Master Thesis in Medical Physics
Department of Physics and Technology
University of Bergen

Performance Evaluation of a Small-Animal PET/CT System

Tordis Johnsen Dahle

Supervisor: Assoc. Prof. Eli Renate Grüner

Co-supervisor: Phd Njål Brekke

Bergen, June 2014

Abstract

This master project is the first vendor-independent performance evaluation of the new nanoScan PET/CT system at the University of Bergen. A comprehensive performance evaluation of a novel scanner is very important, particularly when quantitative assessments of images are required.

The nanoScan PET/CT system is a fully integrated small-animal PET/CT system. An abbreviated performance evaluation of the CT subsystem was done, which included a Hounsfield quality check, a comparison of reconstruction filters and an evaluation of the different scanning methods. The PET subsystem was performance evaluated according to the NEMA NU 4-2008 standard. This standard includes tests of spatial resolution, counting rate capabilities, sensitivity and image quality.

The CT evaluation proved adequate for its intended use. There were only minor differences in the noise measurement of the different reconstruction filters. The scanning method "helical, 1 pitch" would for most applications be recommended, as this scanning method had lowest dose, good images, and just few minutes longer scan time than the scanning method with lowest scan time. The measurements from the PET evaluation were in good agreement with values reported by vendor and in literature. The evaluation of the scanner shows that it has one of the best spatial resolutions available, approximately 1 mm at center of field of view (FOV). The sensitivity at center of FOV was 8.8%, just a bit lower than the highest reported absolute sensitivity at center of FOV, i.e. 10%. The counting rate capabilities proved adequate for all applications undertaken to date, and the NEMA image quality phantom studies demonstrated good values of uniformity and recovery coefficients.

The procedures and methods in this thesis will make it easier to monitor the scanner performance with periodic testing to check if the scanner is robust, reliable and reproducible.

Acknowledgements

I would like to thank all the people who have helped and encouraged me during my work on this thesis. I really appreciate all the help I've received. I would especially like to thank:

My supervisor, Assoc. Prof. Renate Grüner, for all your good ideas and support. Thank you for being available and encouraging, and for taking time to read through the thesis thoroughly, even though you just had a new baby.

My co-supervisor, Phd Njål Brekke, especially for all the help on the practical parts of the project, and for helping me with the development of data analyzing scripts in Python. Thank you also for always answering questions and for reading through the thesis now at the end.

Cecilie Brekke Rygh, for showing me how to use the scanner, and for keeping me updated on when the scanner was available. Thank you also for all the information you have given me on the main use of the scanner.

Kristine Fasmer, for your help at the beginning of the thesis. You really helped me getting started on this work.

The remaining people at the PET center at Haukeland University Hospital, especially Jostein Sæterstøl and the people working in the FDG-production.

Samuel Kuttner at the University of Tromsø, for our discussions on the NEMA NU 4-2008 standard.

My parents and Mike Celia for your help, especially for commenting and proofreading the thesis.

And finally, Agnethe, Renate, Kine, Daniel, Tjalve, Tonje, Christian, Thomas and Thomas, and all my other friends at the Physics Department, for all the discussions and great moments we've had together over the past couple of years. Thank you also, Egil, Ingrid, Karoline and Rebekka, for your support and encouragement.

Contents

Abstract i

Acknowledgements iii

List of Abbreviations viii

List of Figures ix

List of Tables xi

1 Introduction 1

2 Basic Principles of PET/CT scanning 5
- 2.1 Radioactivity and Ionizing Radiation . . . 5
- 2.2 Interactions of Photons with Matter . . . 6
- 2.3 Scintillator Crystals and Photodetectors . . . 9
- 2.4 Radiation Dose . . . 10
- 2.5 Computed Tomography . . . 12
  - 2.5.1 Basics of CT . . . 12
  - 2.5.2 X-Ray Beam Geometry . . . 14
  - 2.5.3 Image Reconstruction . . . 16
  - 2.5.4 Radiation Dose from CT . . . 17
- 2.6 Positron Emission Tomography . . . 19
  - 2.6.1 Basics of PET . . . 19
  - 2.6.2 Data Acquisition . . . 21
  - 2.6.3 Factors Affecting Acquired PET Data . . . 26
  - 2.6.4 Image Reconstruction . . . 27
  - 2.6.5 Radiation Dose from PET . . . 28
- 2.7 Image Quality . . . 28
  - 2.7.1 Spatial Resolution . . . 28
  - 2.7.2 Sensitivity . . . 29

2.7.3 Signal-to-Noise Ratio . . . 30
2.7.4 Uniformity and Partial Volume Effect . . . 31
2.7.5 Artefacts . . . 32
2.8 The NEMA NU 4-2008 Standard . . . 33
2.8.1 Spatial Resolution . . . 34
2.8.2 Scatter Fraction, Count Losses, and Random Coincidence Measurements . . . 36
2.8.3 Sensitivity . . . 37
2.8.4 NEMA Image Quality Phantom Study . . . 38
2.9 Motivation . . . 39

3 Materials and Methods **41**
3.1 Scanner Description . . . 42
3.2 Image Data . . . 42
3.3 Phantoms and Point Sources . . . 44
3.4 Evaluation of the CT Subsystem . . . 49
3.4.1 Hounsfield Quality Check . . . 49
3.4.2 Noise in Reconstruction Filters . . . 49
3.4.3 Different Scanning Methods . . . 52
3.5 Evaluation of the PET Subsystem . . . 54
3.5.1 Spatial Resolution . . . 54
3.5.2 Scatter Fraction, Count Losses, and Random Coincidence Measurements . . . 57
3.5.3 Sensitivity . . . 62
3.5.4 NEMA Image Quality Phantom Study . . . 64

4 Results **67**
4.1 CT Subsystem . . . 67
4.1.1 Hounsfield Quality Check . . . 67
4.1.2 Noise in Reconstruction Filters . . . 70
4.1.3 Different Scanning Methods . . . 72
4.2 PET Subsystem . . . 76
4.2.1 Spatial Resolution . . . 76
4.2.2 Scatter Fraction, Count Losses, and Random Coincidence Measurements . . . 79
4.2.3 Sensitivity . . . 80
4.2.4 NEMA Image Quality Phantom Study . . . 82

5 Discussion **85**
5.1 CT Subsystem . . . 85
5.2 PET Subsystem . . . 87
5.3 Practical Limitations of the PET/CT Evaluation . . . 91
5.4 Implications for In Vivo Imaging . . . 91

6 Conclusion and Future Work **95**

Bibliography **100**

Appendices **101**

A NEMA NU 4-2008 Performance Data for a Collection of Commercial Animal PET Systems **103**
A.1 Spatial Resolution 104
A.2 Scatter Fraction, Count Losses and Random Coincidence Measurements 106
A.3 Sensitivity 107
A.4 NEMA Image Quality Phantom Study 108

B Python Scripts **111**

C Data Sheets of Radioactive Sources **125**

List of Abbreviations

%STD	Percentage Standard Deviation
CBCT	Cone-Beam CT
CT	Computed Tomography
CTDI	Computed Tomography Dose Index
DICOM	Digital Imaging and Communications in Medicine
DLP	Dose Length Product
FBP	Filtered Back-Projection
FDG	Fluorodeoxyglucose
FDK	Fieldkamp-Davis-Kress Algorithm
FOV	Field of View
FWHM	Full Width at Half Maximum
FWTM	Full Width at Tenth Maximum
GPU	Graphical Processing Unit
LOR	Line of Response
LYSO	Lutetium Yttrium Orthosilicate
NECR	Noise Equivalent Count Rate
NEMA	National Electrical Manufacturers Association
PET	Positron Emission Tomography
PMT	Photomultiplier Tube
RC	Recovery Coefficient
ROI	Region of Interest
SNR	Signal-to-Noise Ratio
SOR	Spill-over Ratio
SSRB	Single Slice Rebinning
Std. Dev.	Standard Deviation
VOI	Volume of Interest

List of Figures

1.1 The nanoScan PET/CT system 1
1.2 PET/CT image of a mouse injected with FDG 2

2.1 The intensity of photons as a function of distance 7
2.2 The most common attenuation processes for photons 8
2.3 Schematic overview of a photomultiplier tube 10
2.4 Schematic diagram of an x-ray tube 13
2.5 Fan-beam CT versus cone-beam CT 14
2.6 CT generations 15
2.7 Characteristics of reconstruction filters, FDK algorithm 18
2.8 Reconstruction filters, FDK algorithm 18
2.9 Positron range 20
2.10 Line of Response 21
2.11 2D and 3D data acquisition in PET 22
2.12 Coincidence mode 23
2.13 List Mode 24
2.14 Sinogram, principle 25
2.15 Sinogram, example 25
2.16 Attenuation correction in PET 27
2.17 Comparison of spatial resolution of various scanners 35
2.18 Comparison of NECR of various scanners 36
2.19 Recovery coefficients, microPET P4 system 38

3.1 The nanoScan PET/CT system with description 41
3.2 The CT image quality phantom 44
3.3 The nanoScan Jaszczak phantom 45
3.4 The standard NEMA point source 46
3.5 The mouse-like phantom 46
3.6 The NEMA image quality phantom 47
3.7 Schematic drawing of the NEMA image quality phantom . . . 48
3.8 Placement of ROIs, Hounsfield quality check 51

3.9 Placement of ROI, noise in reconstruction filters test 51
3.10 Placement of ROIs, evaluation of artefacts and SNR 53
3.11 Source arrangement, spatial resolution measurements 54
3.12 Image of a point source, FBP and Tera-Tomo 56
3.13 A typical response function of a point source 56
3.14 Positioning of phantom, counting rate capabilities test 57
3.15 Sinograms and sum projection, counting rate capabilities test . 59
3.16 Sum projection, quantitative evaluation 59
3.17 Sinogram, sensitivity measurements 64
3.18 Scan of NEMA image quality phantom 65

4.1 Images reconstructed with FDK algorithm using various filters 71
4.2 CT images acquired with various scanning methods 74
4.3 Spatial resolution values, FBP 77
4.4 Spatial resolution values, Tera-Tomo 78
4.5 Counting rate curves 79
4.6 Axial absolute sensitivity profile 81
4.7 Recovery coefficients as a function of rod diameter 83

5.1 Mouse scan reconstructed with FBP and Tera-Tomo 92

A.1 Spatial resolution, NanoPET 104
A.2 Axial absolute sensitivity profile, nanoScan PET/MRI 107

List of Tables

2.1 Effective atomic numbers for various materials 6
2.2 Tissue-specific weighting factors 11
2.3 Properties of common positron sources used in PET 20

3.1 Design description of the CT subsystem 43
3.2 Design description of the PET subsystem 43
3.3 Dimensions, CT image quality phantom 44
3.4 Dimensions, nanoScan Jaszczak phantom 45
3.5 Dimensions, mouse-like phantom 46
3.6 Dimensions, NEMA image quality phantom 47
3.7 Acquisition parameters, non-automatic Hounsfield quality check 50
3.8 Acquisition parameters, automatic Hounsfield quality check . . 50
3.9 Acquisition parameters, noise in reconstruction filters test . . . 50
3.10 Acquisition parameters, dose and scan time measurement . . . 53
3.11 Acquisition parameters, evaluation of artefacts and SNR 53
3.12 Acquisition parameters, spatial resolution measurements . . . 55
3.13 Reconstruction parameters, spatial resolution, FBP 55
3.14 Reconstruction parameters, spatial resolution, Tera-Tomo . . . 55
3.15 Acquisition parameters, counting rate capabilities 58
3.16 Reconstruction parameters, counting rate capabilities 58
3.17 Acquisition parameters, sensitivity measurements 63
3.18 Reconstruction parameters, sensitivity measurements 63
3.19 Acquisition parameters, image quality phantom study 66
3.20 Reconstruction parameters, image quality phantom study . . . 66

4.1 CT image noise measurement, non-automatic test 68
4.2 CT image noise measurement, automatic test 68
4.3 Image homogeneity measurement in air, non-automatic test . . 69
4.4 Image homogeneity measurement in water, non-automatic test 69
4.5 Image homogeneity measurement in air, automatic test 69
4.6 Image homogeneity measurement in water, automatic test . . . 69

4.7 Mean HU and Std. Dev., CT reconstruction filters 70
4.8 Scan time and dose index, various scanning methods 73
4.9 Mean HU and Std. Dev. in artefact ROIs 74
4.10 Data, SNR measurements 75
4.11 SNRs in images acquired with different scanning methods . . . 75
4.12 Spatial resolution values, FBP 76
4.13 Spatial resolution values, Tera-Tomo 76
4.14 Peaks of count rate plot 80
4.15 Sensitivity and absolute sensitivity values 80
4.16 Absolute sensitivity at different axial positions 81
4.17 Uniformity test results 83
4.18 Recovery coefficients of different rods 83
4.19 Spill-over ratio for water- and air-filled cylinders 83

5.1 Reconstruction parameters, mouse image 93

A.1 Overview of PET systems 103
A.2 Spatial resolution values, various scanners 105
A.3 Counting rate capabilities, various scanners 106
A.4 Absolute sensitivity, various scanners 107
A.5 Summery of image quality test, various scanners 109

Chapter 1

Introduction

Computed tomography, CT, is an imaging system which generates cross sectional slice images of an object, based on the attenuation of x-rays through the object. The CT images have high tissue contrast with good anatomic information, and thus provide valuable diagnostic information. Also, CT images are used as the basis for performing photon-attenuation and scatter corrections in positron emission tomography, PET [1].

PET is an imaging system which provides biochemical and metabolic information. The PET images are based on the measurement of radiation emitted due to a radiotracer which has been injected into the body. The PET images will normally not provide much anatomic information, so PET scanners are commonly integrated with a CT scanner to improve the diagnostic interpretation [2]. These integrated scanners are referred to as PET/CT scanners.

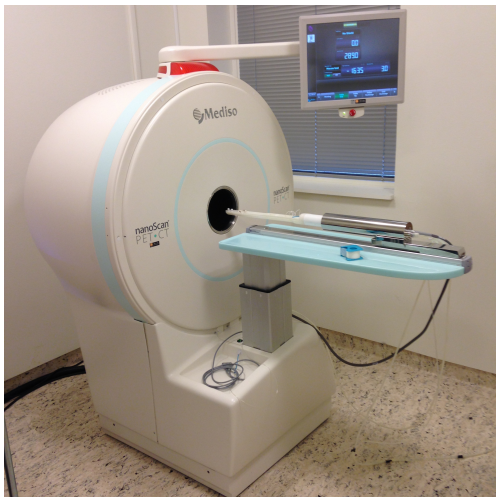

Figure 1.1: The nanoScan PET/CT system.

The University of Bergen has recently purchased a small-animal PET/CT system, the nanoScan PET/CT system from Mediso, Figure 1.1, and it is the first of its kind in Norway. The system installation was officially opened in April 2013, and it is located at the PET center, Haukeland University Hospital, in Bergen. Use of the system is organized through the Molecular Imaging Center (MIC), University of Bergen.

A small-animal PET/CT scanner is a preclinical scanner used to produce images of small animals such as mice and rats, like the image shown in Figure 1.2. Because these animals are much smaller than humans, preclinical scanners must have higher spatial resolution and smaller gantry opening than the clinical scanner [3].

Preclinical systems are mandatory to expand the research activities in PET, particularly within preclinical applications, pharmaceutical drug development and basic radiochemistry research. As the experiments are not only for visualizing results qualitatively, it is important to have a sensitive and robust scanner which allows quantitative assessments. To make sure that the results are robust, reproducible and reliable, a comprehensive performance evaluation of the scanner is needed.

At present, small-animal PET/CT scanners are still in substantial technical development. Preclinical imaging systems are also more experimental and less standardized with respect to protocols and quality control than their clinical counterparts. Preclinical systems provide many options when imaging, and choice of acquisition parameters result in different image quality, scan time and radiation dose to the animals. This makes it important to explore the functionality of the new equipment, and to establish routine procedures for future users of the PET/CT system.

The preclinical PET/CT scanner in Bergen is still at an early stage, but there are already several experiments going on. The main use of the PET/CT system is non-invasive and longitudinal characterization of various tumors and monitoring of treatment effect. Ongoing experiments include detection

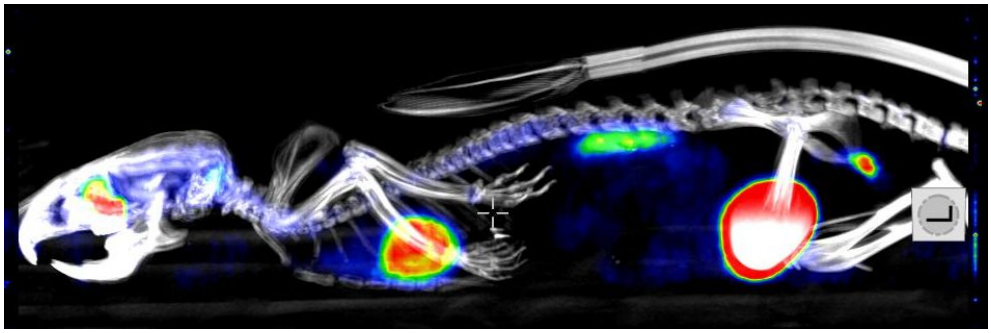

Figure 1.2: PET/CT image of a mouse injected with FDG and CT contrast agent.

of metastatic tumors, evaluating treatment response (by scanning the animal before and after treatment, using the same radiotracer), measuring glomerular filtration rate (which describes the flow rate of filtered fluid through the kidneys), and evaluating the degradation of the dental crest (by feeding the animals red wine).

The overall goal of this master project was to evaluate the performance of the PET subsystem, and give an abbreviated evaluation of the CT subsystem. The evaluation of the CT subsystem included a pixel value check, as well as a short comparison of the different reconstruction filters. Different scanning methods were also evaluated, by comparing scan time, radiation dose, artefacts and signal-to-noise ratio.

The performance evaluation of the PET scanner was based on the NEMA NU 4-2008 standard, which is a standard published by the National Electrical Manufactures Association (NEMA) [4]. This standard is supposed to form a baseline of system performance in typical imaging conditions, and thereby making comparisons between systems from different vendors easier. The NEMA NU 4-2008 standard includes tests of spatial resolution, scatter fraction, counting rate capabilities, sensitivity and image quality. The rest of the thesis is outlined as follows:

Chapter 2 presents the basic physics relevant for this thesis. Before further explaining PET and CT imaging, an introduction to radioactivity and ionizing photons is given. Factors describing image quality are discussed at the end of the chapter. These factors will be used in the performance evaluation of the PET/CT scanner. A section comparing NEMA NU 4-2008 parameters of various preclinical PET scanners is also included, to have something to compare the results with. **Chapter 3** is the materials and methods chapter. This chapter starts by describing the equipment used; the nanoScan PET/CT system, the phantoms and the standard NEMA point source. Then, the methods used to evaluate the CT and PET subsystems are described. In **Chapter 4** the results from the performance evaluation are given. In **Chapter 5** the findings of the current thesis are discussed, in light of existing literature. The chapter also presents the shortcomings of the methodology alongside future recommendations. Finally, the conclusion is given in **Chapter 6**, and future work are presented.

Chapter 2

Basic Principles of PET/CT scanning

In this chapter the basic principles of PET/CT scanning and factors influencing the image quality will be presented. An insight to the NEMA NU 4-2008 performance evaluation of other preclinical scanners is given. Both PET and CT scanning are based on the detection of photons, either emitted as bremsstrahlung and characteristic radiation from an x-ray tube, or emitted by positron-electron annihilation, where the positron comes from the decay of a radioisotope. The chapter will therefore start with an introduction to radiation physics.

2.1 Radioactivity and Ionizing Radiation

A nucleus is radioactive if it can spontaneously change its quantum mechanical properties by decaying/disintegrating. Radioactive decay is a statistic process. For N unstable nuclei, with a probability λ to disintegrate within a unit time, dt, dN nuclei are expected to disintegrate. Starting out with N_0 unstable nuclei at time $t = 0$, there will be N unstable nuclei at a given time t:

$$N(t) = N_0 e^{-\lambda t}. \tag{2.1}$$

The half-life, $t_{1/2}$, is the time it takes for half of the original N_0 unstable nuclei to decay.

As the number of unstable nuclei at a given time is unknown, the activity in a sample is measured instead. The activity, A, is the number of unstable nuclei that decay per second, and has unit bequerel, 1 Bq = 1 s^{-1}:

$$A = \left|\frac{dN}{dt}\right| = \lambda N_0 e^{-\lambda t} = A_0 e^{-\lambda t}, \tag{2.2}$$

	Fat	Air	Water, muscle	Bone
Effective atomic number	6.4	7.6	7.4	13.3

Table 2.1: Effective atomic numbers of various materials in the body [6].

where A_0 is the initial activity.

A nucleus decay by electron capture or by emitting radiation, i.e. by emitting particles or photons. Types of radiation are alpha (α), beta (β) and gamma (γ) radiation. In α-decay the nucleus emits an alpha particle, i.e. a helium nucleus. In $\beta^{\mp}$-decay an electron or a positron is emitted, and in γ-decay an exited nucleus emits one or more photons [5]. A photon is a quantum gauge particle carrying electromagnetic energy, and it is considered a neutral, massless particle.

In β^+-decay, the atomic nucleus is converted into a nucleus with one lower atomic number by emitting a positron (e^+) and an electron neutrino (ν_e);

$$ {}^{\mathrm{A}}_{\mathrm{Z}}\mathrm{X} \rightarrow {}_{\mathrm{Z}-1}{}^{\mathrm{A}}\mathrm{Y} + e^+ + \nu_e, \tag{2.3} $$

where A and Z are the mass number and atomic number of the decaying nucleus. The positron is the electron's antiparticle. Positrons emitted in the decay will almost immediately annihilate with a nearby electron, and emit photons.

2.2 Interactions of Photons with Matter

Both positron emission tomography (PET) and computed tomography (CT) create images based on the detection of photons. In CT, the photons have energy in the range 20 - 120 keV, and in PET the photon energy is 511 keV.

Photons can be scattered and absorbed when passing through tissue, leading to a decrease in the radiation intensity. The most common ways for electromagnetic radiation to interact with matter when the photon energy is in the keV-range are the photoelectric effect and Compton scattering [5]. For higher photon energies pair production becomes important, see Figure 2.2.

The interaction of photons with matter is also dependent on the effective atomic number of the matter which the photon interacts with. Some examples of effective atomic numbers are given in Table 2.1. The effective atomic number is used for compounds and mixtures of different materials, and is equivalent to the atomic number.

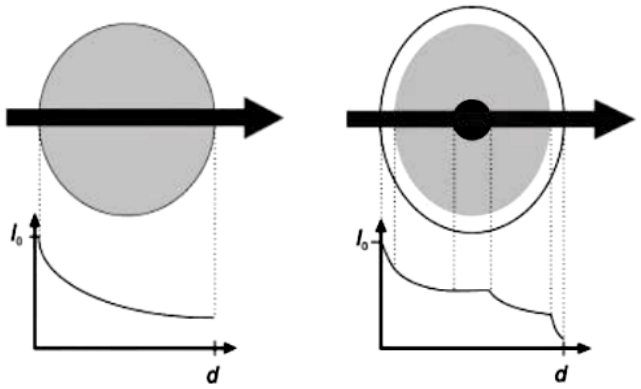

(a) (b)

Figure 2.1: The intensity I of monochromatic radiation as a function of distance for (a) a homogeneous object, and (b) an inhomogeneous object [1].

Linear Attenuation Coefficient

The linear attenuation coefficient, μ, is the fraction of radiation intensity, I, which is lost per unit length, x:

$$\frac{dI}{dx} = -\mu I. \tag{2.4}$$

By solving this equation the following is obtained:

$$I = I_0 e^{-\mu x}, \tag{2.5}$$

where I_0 is the initial intensity at position $x = 0$. The linear attenuation coefficient decreases with the photon energy and increases with the atomic number and density of the absorber. Equation (2.5) gives the intensity of monochromatic radiation as a function of distance for a homogeneous absorber, which is also illustrated in Figure 2.1a. In this case, it is easy to calculate the linear attenuation coefficient. However, the irradiated objects are typically complex objects with composite layers of materials. Irradiation of an inhomogeneous object is illustrated in Figure 2.1b. The radiation intensity, through line $s(x, y)$ between the radiation source and the detector, will in this case be given by:

$$I = I_0 \cdot \exp\left[-\int_0^d \mu(x, y)ds\right], \tag{2.6}$$

where d is the distance between radiation source and detector.

It is even harder to find the linear attenuation coefficient if the object is irradiated by polychromatic radiation. When the photon beam is polychromatic, i.e. when the photon beam has an energy spectrum, there will be a

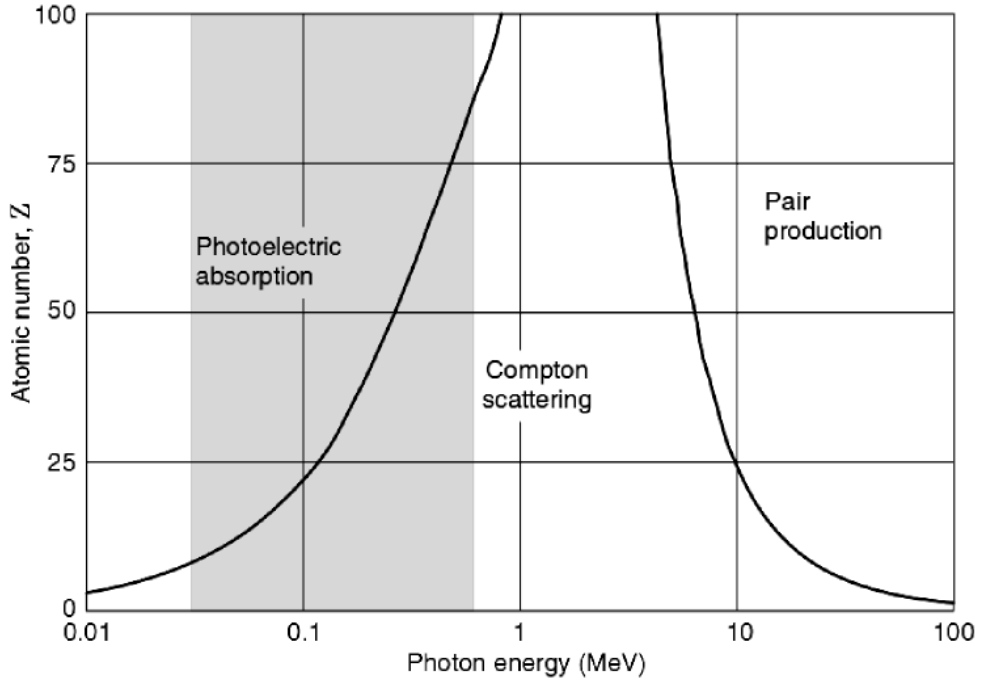

Figure 2.2: The three most common interaction processes for photons in matter [5]. Gray part is the energy range in PET/CT, so the most common interactions in medical imaging are Compton scattering and photoelectric effect.

"beam hardening" effect as a function of depth in the absorber; the low energy photons will be attenuated more rapidly than the high energy photons. In this case the energy intervals, $E(x, y)$, must also be integrated over:

$$I = \int_0^{E_{max}} I_0(E) \cdot \exp\left[-\int_0^d \mu(x, y, E)ds\right] dE. \tag{2.7}$$

The attenuation of keV-photons is essentially due to the photoelectric effect and Compton scattering. These two processes can, in this case, therefore be considered the only contributions to the linear attenuation coefficient:

$$\mu = \mu_\tau + \mu_\sigma, \tag{2.8}$$

where μ is the linear attenuation coefficient, and μ_τ and μ_σ are the contributions from the photoelectric effect and from Compton scattering, respectively [1].

Photoelectric Effect

In the photoelectric effect, the photon collides with a bound electron. The photon is absorbed, and the electron, called a photoelectron, is released from

the atom. The binding energy of the photoelectron will be released as Auger-electrons or as characteristic x-rays. The majority of the photon energy will be absorbed locally in the photoelectric effect, but not necessarily all of it since the characteristic x-rays might escape [5].

The photoelectric effect predominates at low energy photons and high-Z material, as seen in Figure 2.2. The probability of the photoelectric effect has a Z-dependence of $Z^4 - Z^5$ [5]. In diagnostic x-ray images this effect is utilized, showing a sharp contrast between materials with different densities, such as bone and tissue.

Compton Scattering

Compton scattering is a collision between a photon and a "free" electron, i.e. an electron that is so loosely bound to the atom that it can be considered free. The photon will be scattered from its initial path, and some of its energy will be absorbed locally [5]. Compton scattering is the largest source of blurring in medical imaging, e.g. in PET, where scattered photons make false lines of response, see Section 2.6.1.

The probability of Compton scattering has a Z-dependence of Z [5]. Since the Z-dependence is not as strong here as it is for the photoelectric effect, imaging with photons in the Compton energy range will not produce as sharp images as when using photons in the photoelectric range. The photon energies used in diagnostic x-ray imaging, which includes CT imaging, are therefore in the photoelectric energy range.

2.3 Scintillator Crystals and Photodetectors

To produce images in PET and CT, the photons have to be detected. This is done by a detector which stops the photon ray and produces an electrical signal. The detector should have high enough stopping power to totally absorb the photons within the detector. For optimal image quality, the detector should have a high spatial resolution to increase image resolution. The PET detector also requires a very good energy resolution and a high timing resolution [8].

The detectors utilized in PET, and often in CT, are scintillator detectors. These detectors consist of a scintillator crystal coupled to a photodetector. A photomultiplier tube (PMT) is often the photodetector of choice in PET.

Figure 2.3 shows a scintillator crystal coupled to a PMT. The PMT is a vacuum tube, which consists of a photocathode, a focusing electrode, dynodes and an anode. The scintillator crystal converts ionizing radiation into visible light, which hits the photocathode in the PMT. Electrons in the photocathode are excited by the light, and photoelectrons are emitted into vacuum.

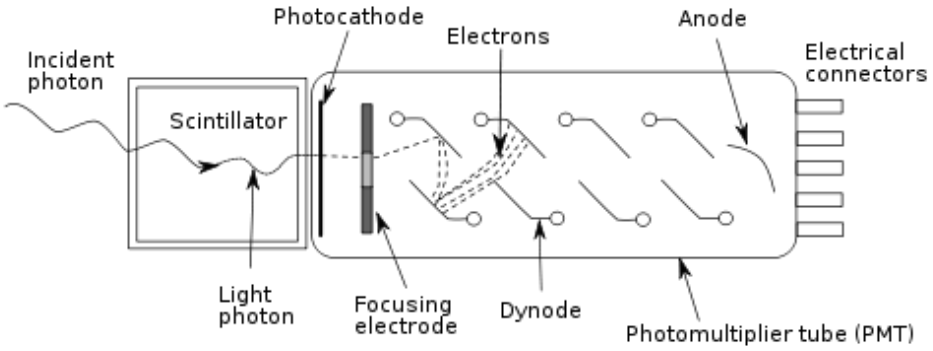

Figure 2.3: A schematic overview of a photomultiplier tube (PMT) [7]. The scintillation photons hit the photocathode to produce photoelectrons, which are accelerated by the electric field, and multiplied at each dynode throughout the PMT.

The photoelectrons are then accelerated and focused by the focusing electrode onto the first dynode where they are multiplied by means of secondary electron emission. This secondary emission is repeated at each of the successive dynodes. Finally, the multiplied secondary electrons are collected by the anode, which transfers the electron current to an external circuit [9].

2.4 Radiation Dose

Ionizing radiation can damage living tissue, and potentially cause cancer. The damage will depend on the energy absorbed in the tissue, the type of radiation, and the tissue type itself. The energy absorbed in matter when exposed to radiation is called the radiation dose, and it is described in three ways: absorbed dose, equivalent dose, and effective dose.

Absorbed Dose

Absorbed dose, D, is a measure of the mean energy $\bar{\varepsilon}$ deposited by ionizing radiation to matter of mass m:

$$D = \frac{d\bar{\varepsilon}}{dm}. \tag{2.9}$$

Absorbed dose has unit gray, where 1 Gy = 1 J/kg. Absorbed dose does not tell how damaging the radiation is, since damage depends on other factors as well, e.g. radiation type [10, 11].

Tissue	Tissue weighting factor
Bone-marrow (red), Colon, Lung, Stomach, Breast	0.12
Gonads	0.08
Bladder, Esophagus, Liver, Thyroid	0.04
Bone surface, Brain, Salivary glands, Skin	0.01

Table 2.2: Tissue-specific weighting factors, w_T, given by ICRP (International Commission on Radiation Protection) [12].

Equivalent Dose

Some radiation types are more damaging than others, even when the absorbed dose is the same. To get a better measure of the damage, the equivalent dose is defined. Equivalent dose is defined with a weighting factor, w_R, which depends on the radiation type, and is introduced to give a better measure of the damage. For photons, w_R = 1.

The equivalent dose, H_T, for a tissue or an organ T is given by:

$$H_T = \sum_R w_R D_{T,R}, \tag{2.10}$$

where $D_{T,R}$ is the mean absorbed dose from radiation R in a tissue or organ T [12]. The equivalent dose has unit sievert, 1 Sv = 1 J/kg.

Effective Dose

Different tissues have different risk of radiation induced cancer. The effective dose, H_E, is the tissue-weighted sum of the equivalent doses in all the specified tissues and organs of the body, given by:

$$H_E = \sum_T w_T \sum_R w_R D_{T,R} = \sum_T w_T H_T, \tag{2.11}$$

where H_T is the equivalent dose in a tissue or organ, T, and w_T is the tissue weighting factor [12]. The tissue weighting factor represents the relative contribution of that tissue or organ to the total health detriment resulting from uniform irradiation of the body, and is defined such that

$$\sum_T w_T = 1.$$

Table 2.2 summarize w_T for organs.

Effective dose has the same unit as equivalent dose, i.e. sievert.

Radiation Exposure and Dose Limits

The average annual radiation dose per person in Norway is approximately 3-4 mSv. The largest contribution to natural radiation in Norway is radon. For people working with radiation, a maximum limit of 20 mSv per year is set by the Norwegian Radiation Protection Authority (Statens Strålevern). In addition the regulations state that the radiation should be managed to be *As Low As Reasonably Achievable* [11].

2.5 Computed Tomography

2.5.1 Basics of CT

Computed tomography, CT, is an imaging modality were x-ray photons are sent through the body to produce cross sectional images. The images are made of voxels (volume elements), and each voxel is represented by a CT-number, which depends on the linear attenuation coefficient, μ, of the tissue in that voxel. The x-rays are sent from the x-ray source towards a detector. The detector measures the x-ray's intensity, which depends on the initial intensity and the attenuation of the intensity along the line between the x-ray source and the detector. X-rays are sent along a large number of lines through the cross section to obtain enough data to produce an image. The images are then reconstructed from the projections [1, 13].

CT images provide a sharp contrast between bone and tissue, which makes CT a good choice when anatomic information is needed. However, there are some limitations when using CT images as the basis for tumor delineation. The density of tumor tissue may be almost identical to that of nearby healthy tissue, and therefore hard to identify based on CT images alone.

X-Ray Tube

The x-rays used in CT are produced in an x-ray tube. In the x-ray tube, electrons, called projectile electrons, are accelerated from the cathode by high voltage before hitting a target in the anode, see Figure 2.4. There are two types of x-rays produced, bremsstrahlung and characteristic x-rays [14].

Bremsstrahlung is produced when the projectile electrons are decelerated by the Coulomb field of the nuclei in the target. These x-rays can have a range of energies, where the maximum energy is equal to the energy of the projectile electrons. This maximum energy is determined by the tube voltage, i.e. the accelerator voltage of the x-ray tube.

Characteristic x-rays are produced when the projectile electrons collide with the electrons in the target atoms. These collisions ionize the target atoms, and characteristic x-rays are emitted when the vacancies in the ionized atoms

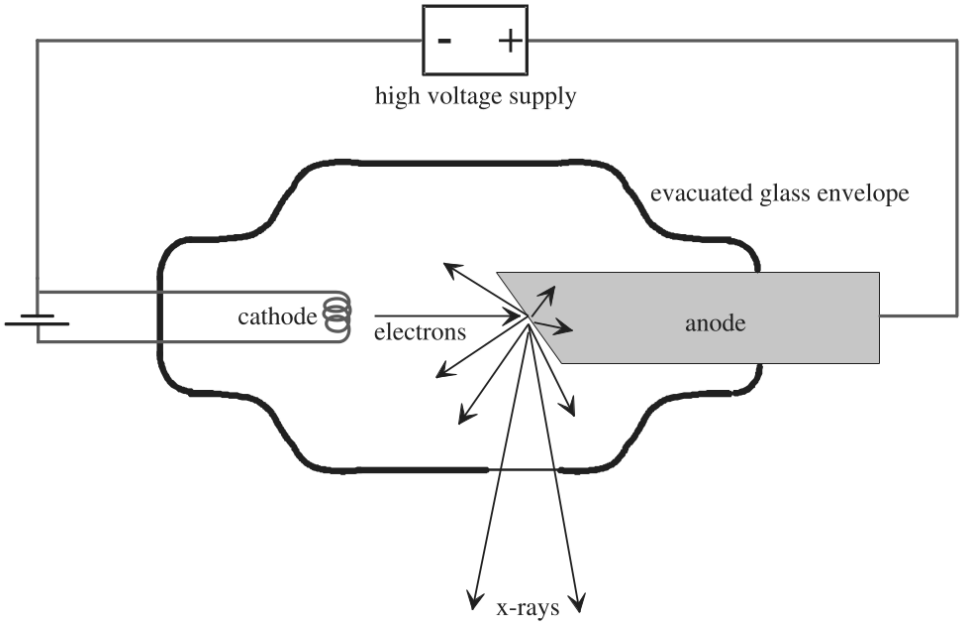

Figure 2.4: Schematic diagram of an x-ray tube [14].

are filled. The energy of these x-rays depends on the binding energies of the electrons in the electron shell, which in turn depend on the type of atoms in the anode.

CT Image

Each voxel in the CT image is represented by a CT-number. These numbers are represented by different gray levels in the image. The CT-number is proportional to the linear attenuation coefficient of the tissue in the voxel, relative to the linear attenuation coefficient of water;

$$\text{CT-number} = \frac{\mu_T - \mu_{water}}{\mu_{water}} \times 1000 \text{ HU}, \tag{2.12}$$

where μ_T and μ_{water} are the linear attenuation coefficient in tissue and water respectively, and HU is the Hounsfield unit. The CT image does not directly show the distribution of the linear attenuation coefficient, since this would make it impossible to compare images from different scanners, as the linear attenuation coefficient is highly dependent on the energy of the x-ray photons [1].

In medical imaging the CT-numbers typically range from -1024 HU to +3071 HU. A human observer cannot discern this many gray levels, so a range of CT-numbers are chosen when examining a CT image. These CT-numbers are displayed using different gray levels, and CT-numbers outside this region

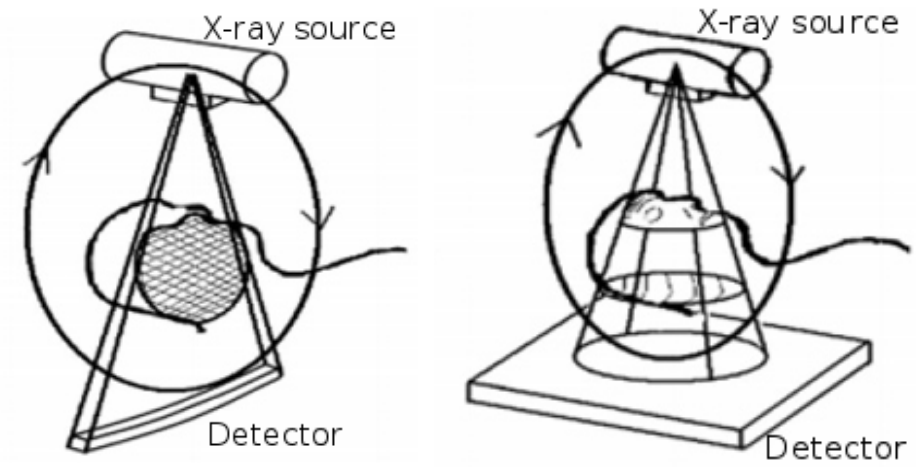

(a) (b)

Figure 2.5: CT beam geometry; a) fan beam CT and b) cone beam CT [15].

are either displayed as white or black. The lowest CT-numbers are usually displayed as white, and the highest CT-numbers as black.

2.5.2 X-Ray Beam Geometry

Modern CT scanners are either fan-beam CT or cone-beam CT, Figure 2.5, which refers to the x-ray beam geometry.

Fan-Beam CT

Figure 2.6 shows four classical designs that have been used for data collection in CT. The first CT generation used a pencil beam and one detector. This method was slow, so to speed things up more detectors were added. With more detectors, the x-ray beam became a small fan-beam instead of a pencil beam; and this is the second CT generation. These two first generations of CT scanners were only used for head examinations. In 1976 the first whole body scanners came on the marked, i.e. the third CT generation. The third generation of CT scanners is fan-beam scanners, where both the x-ray tube and the detectors rotate around the patient. Fan-beam CT with a stationary detector ring is used in most clinical CT scanners today. This is the fourth generation of CT scanners [1].

Cone-Beam CT

Cone-beam CT (CBCT) directs a cone-shaped source of ionizing radiation through the object onto a 2D x-ray detector on the opposite side, see Figure

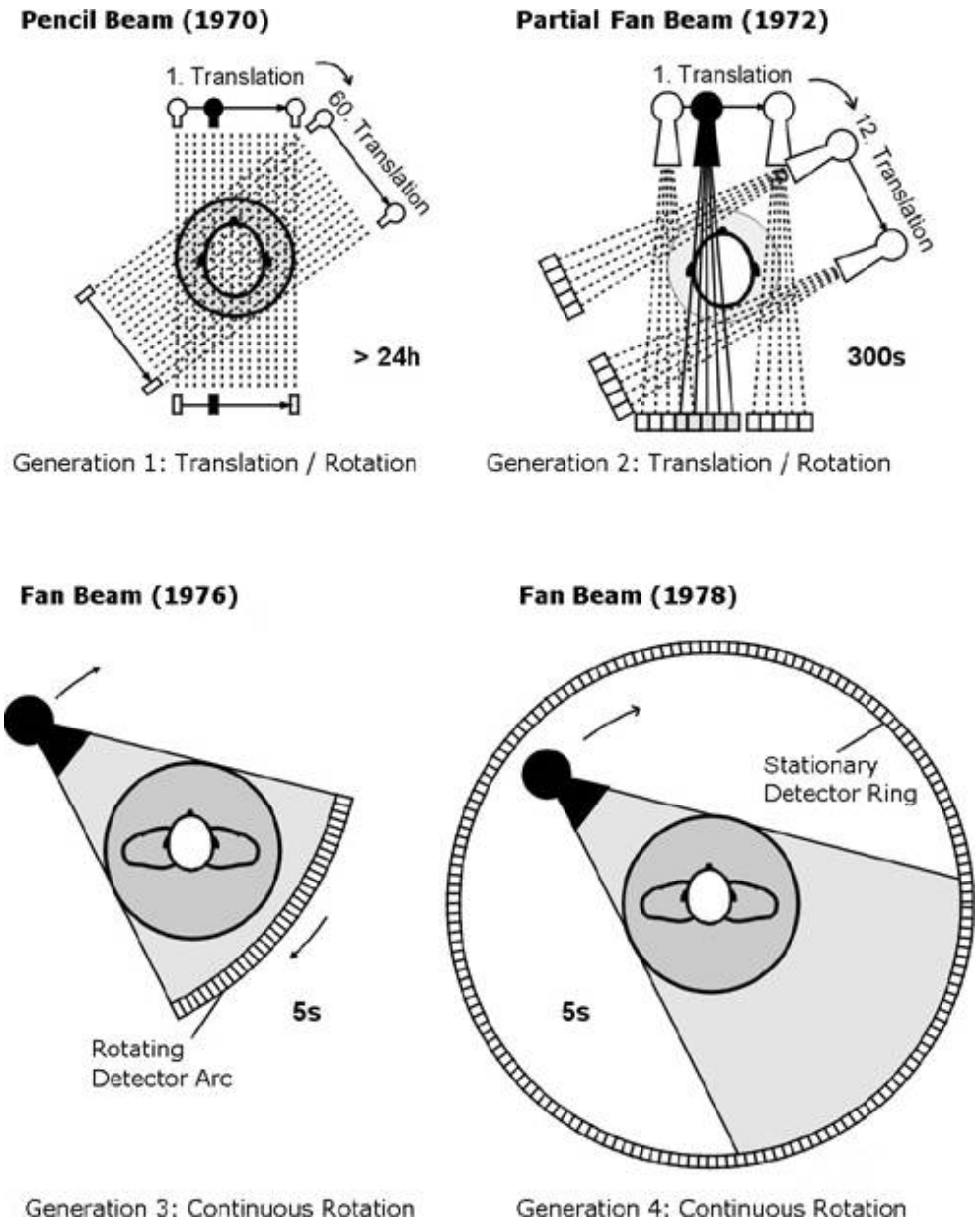

Figure 2.6: Different CT configurations (generations) [1].

2.5.The x-ray source and the detector rotate around the object in CBCT image acquisition [16]. There are various scanning methods in CBCT.

In the circular acquisition method, multiple sequential planar projection images of the field of view (FOV) are acquired in a complete, or partial, arc during the rotation [16]. A further development of this method is called semi-circular. In the semicircular scanning method, the scan object bed will move slightly back and forth while acquiring the images. This hardly noticeable movement is done to reduce ring artefacts (see Section 2.7.5) in the images. Because of this movement, the images will not be acquired in a completely circular path, but in a semicircular path. In this thesis, images acquired in a complete arc will be referred to as "semicircular, full scan", while a partial arc (180°) will be referred to as "semicircular, half scan".

In the semicircular acquisition method, an image can only be acquired for one bed position. Sometimes a larger axial FOV is needed, and to achieve this, the image has to be acquired for several bed positions. In the helical acquisition method, the bed will have a horizontal motion as the x-ray source and the detector rotate around the table. This means that the helical acquisition method can have longer axial FOV than the semicircular acquisition method [17]. The movement of the table is given by the pitch number:

$$\text{Pitch number} = \frac{\text{table travel by single rotation}}{\text{axial field of view}}. \tag{2.13}$$

1 pitch means that during one single 360° rotation the table moves 1 FOV length.

Fan-Beam CT versus Cone-Beam CT

CBCT can incorporate the entire FOV with only one rotational sequence of the gantry, so CBCT uses less scan time compared to fan-beam CT. Because of shortened scan time, CBCT has advantages such as reduction of image blurring caused by the translation of the patient, and less susceptibility to movement artefacts [16].

However, when incorporating the entire FOV with only one rotational sequence, it is an advantage with as small transaxial FOV as possible. With larger transaxial FOV there is a limitation in image quality related to noise and contrast resolution, because of the detection of large amounts of scattered radiation [16]. This makes CBCT most useful for preclinical scanners and for small clinical scanners, e.g. the CT scanners used in dentistry.

2.5.3 Image Reconstruction

CT images are computed from sinograms, which contain information on the linear attenuation distribution, $\mu(x, y)$, given as a set of projection values. The

projection values are the logarithm of the ratio of the primary intensity and the attenuated intensities. Each line between x-ray source and detector has a point in the sinogram, located in the sinogram depending on the line's angle and distance from center of FOV. Thus, each projection value in the sinogram corresponds to a line between the x-ray source and detector. A common way of reconstructing a CT image from this information is filtered back-projection (FBP) [1].

A simple back-projection is a back-profile of ray sums. A ray sum is the sum of the attenuation coefficients along the path of a single ray. To back-profile the ray sums means to share the ray sums out equally among the voxels through which the ray passes. This gives a poor image, with a star-burst pattern which blurs the edges of the object. To remove the star-burst pattern, a convolution between the attenuation profile and a filter function is done prior to back-projection. This is the filtered back-projection method [14].

In conventional fan-beam CT, individual axial slices of the object are reconstructed using FBP. In CBCT, a 3D volume must be reconstructed from 3D projection data, referred to as "cone-beam reconstruction". The most approximate cone-beam reconstruction is the FDK method (Fieldkamp-Davis-Kress algorithm). This algorithm uses a convolution back-projection method, i.e. it applies a filter in the frequency domain before back-projecting the projection frames, like in normal FBP [16, 18].

The RamLak or RAMP filter is a filter which suppresses the low frequency components and raises the high frequency parts of the signal. The RamLak filter can be combined with several window functions for filtering the high frequency components. This results in new filters, which are named after the window function, and they are simply the product of the window function and the original RamLak filter. These filters, characteristics shown in Figure 2.7, can be categorized into three groups [18].

The first group contains high-resolution filters. Filters in this group are RamLak, Butterworth and the Shepp-Logan. The second group has less noise than the high resolution filters in the first group, but the reconstruction is reduced as a consequence. Filters in this group are Cosine, Hamming and Hann. The third group are low-resolution filters. A filter here is the BlackMan filter. With the BlackMan filter the noise is about 60% and the resolution approximately 75%, of an equivalent RamLak filtered image. The noise, contrast resolution and spatial resolution of the filters compared to each other are given in Figure 2.8.

2.5.4 Radiation Dose from CT

To give an estimate of radiation dose delivered to the patient during a CT scan, two dose indices, the CT dose index ($CTDI_{vol}$) and the dose length product

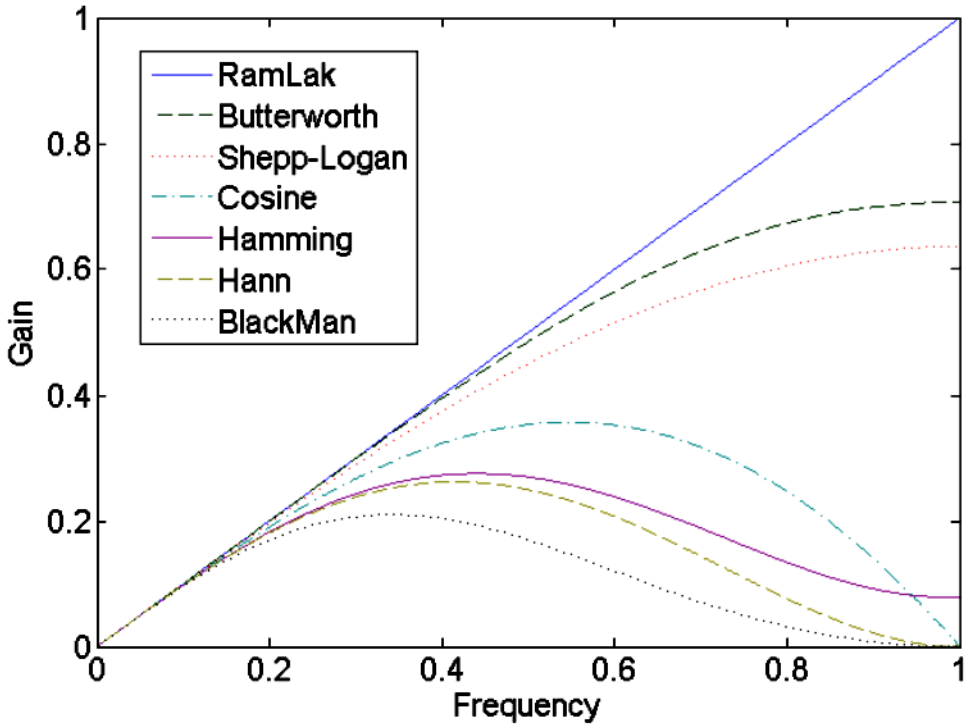

Figure 2.7: Characteristics of the different filters. Horizontal axis represents the frequencies from 0 (base frequency) to 1 (highest frequency). Vertical axis represents the gain (multiplier) for the current frequency [18].

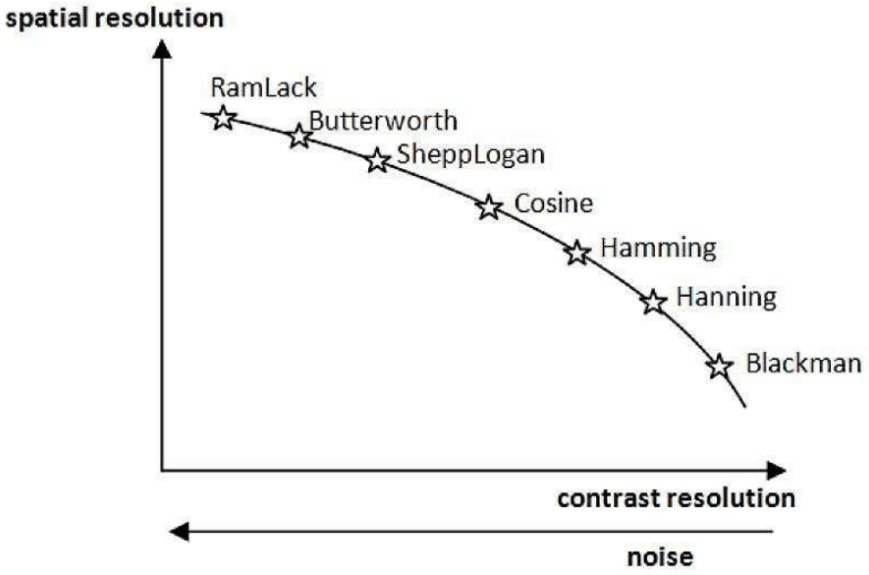

Figure 2.8: Reconstruction filters, spatial or contrast resolution [17]. Hanning is the Hann filter.

(DLP), are introduced.

$CTDI_{vol}$ has unit gray, and represents the radiation dose delivered to a standard plastic CDTI phantom, which is a cylindrical plastic phantom [19]. $CTDI_{vol}$ provides a standardized method for estimating and comparing the radiation output from different CT scanners, but does not give an indication of patient dose. The displayed $CTDI_{vol}$ on the CT scanner is independent on the changes in patient size, as it assumes that the patient is the cylindrical plastic phantom. The actual $CTDI_{vol}$ is very dependent on patient size. This therefore underestimates dose to smaller patients and overestimates dose to larger patients.

The total amount of radiation delivered to a patient during a given examination is dependent on the relative intensity of the radiation that is incident on the patient, and on the CT scan length. The relative intensity of the radiation is given by the $CTDI_{vol}$, and this index multiplied by the scan length gives the DLP, which can be used to determine the total amount of radiation given to the patient.

2.6 Positron Emission Tomography

2.6.1 Basics of PET

A PET scanner is a diagnostic imaging modality which creates images based on the measurement of radiation emitted due to a radiotracer which has been injected into the body. The radiotracer emits positrons, which will almost immediately interact with electrons in the body. An electron and a positron will briefly orbit before uniting, annihilating, and producing two (or sometimes three) photons which the PET scanner can detect [20]. These photons will have the same energy, and conservation of energy requires, for the case with two photons, that each photon has energy $E = m_e c^2 = 0.511$ MeV. Conservation of momentum requires that the photons travel in opposite directions (or almost opposite direction if the initial momentum was not completely zero).

Positron Range

In PET imaging the location of interest is where the positron is emitted from the radiotracer. This location is not necessarily equivalent to what is actually detected, i.e. the point of annihilation of the positron and the electron, Figure 2.9. This is a limitation in spatial resolution, and comes from the fact that the positron will be emitted with a kinetic energy, which comes from excess beta decay energy. The positron can take on a range of kinetic energy values, because the excess beta decay energy can be distributed between the positron and neutrino in different ways. For typical PET isotopes the positron will have

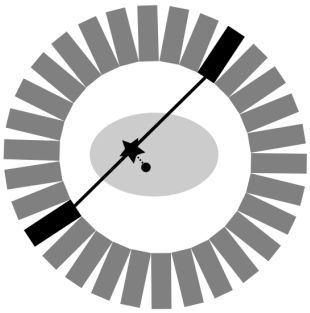

Figure 2.9: Positron range, point of decay versus annihilation.
(• = Photon emitted, ★ = annihilation event, — = assigned LOR).

Nuclide	$t_{1/2}$ (mins)	$Range_{max}$ (mm)	$Range_{mean}$ (mm)
^{11}C	20.4	4.1	1.1
^{13}N	9.96	5.1	1.5
^{15}O	2.03	7.3	2.5
^{18}F	109.74	2.4	0.6
^{68}Ga	68.3	8.2	2.9
^{82}Rb	1.25	14.1	5.9
^{124}I	6048	6.3	2.3

Table 2.3: Decay time and range in water for the most common positron sources used in PET [23, 24]. $t_{1/2}$ is the half-life, and $Range_{max}$ and $Range_{mean}$ are maximum and mean range in water, respectively.

a range up to a few millimeters [21]. The mean and maximum range in water for various positron sources are given in Table 2.3.

Radiotracers

A radiotracer is a quantity of biologically important material which has been labelled with radioisotopes, i.e. one or more of the material's atoms are replaced with a radioisotope. Fluorine-18, or ^{18}F, is the most commonly used isotope in PET scans [22], but there are also other isotopes which can be used. See Table 2.3 for the most common radioisotopes used in PET.

The images produced by a PET scanner depend on the biodistribution of the radiotracer in the biological system. Different radiotracers will therefore produce different images. The most used radiotracer in clinical PET scans is FDG, or fluorodeoxyglucose (^{18}F combined with deoxy-glucose) [22]. This radiotracer is used in oncology for staging, restaging and evaluation of tumor response to treatment.

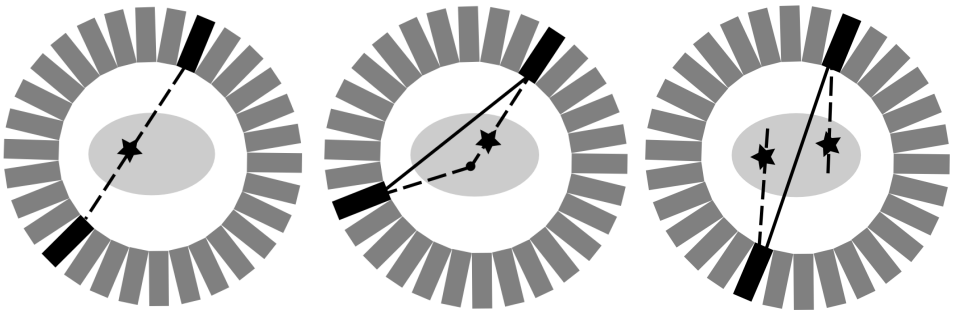

(a) True coincidence (b) Scattered coincidence (c) Random coincidence

Figure 2.10: Coincidence detection. In (a) there is a true line of response, and in (b) and (c) a false line of response. The black detector is where the photons are detected.
(★ = Annihilation event, ● = scatter, - - - = gamma ray, — = assigned LOR).

Line of Response

The PET image shows the distribution of the radiotracer in the body. What is actually detected are the two photons from the positron-electron annihilation. Since these photons have the same energy and are sent in opposite directions, they will hit a detector almost at the same time. The line between the two detectors is called line of response (LOR), and for a true LOR the annihilation happened somewhere along this line. If one of the photons is scattered, or if photons which are not from the same annihilation make a coincidence hit, a false LOR is formed, Figure 2.10.

The PET detectors will only accept a photon hit if it is a coincidence event, i.e. when photons are detected by two detectors within a specified time window and energy window. All coincidence events are collectively called prompts, which include true, random and scattered events.

The scanners ability to detect positron-electron annihilation gamma rays can be expressed as the rate (counts per second) that coincidence events are detected for a given source strength and branching ratio. This is called the scanners sensitivity, see Section 2.7.2.

2.6.2 Data Acquisition

2D and 3D Data Acquisition

PET data can be acquired in either 2-dimensional (2D) or 3-dimensional (3D) mode. In 2D mode, a thin septa of tungsten or lead are inserted between the detector rings, Figure 2.11a. The septa are used as collimators, making sure that only direct coincidence events between two paired detectors in a ring, or in two neighbor rings, are recorded. This is done in an attempt to eliminate

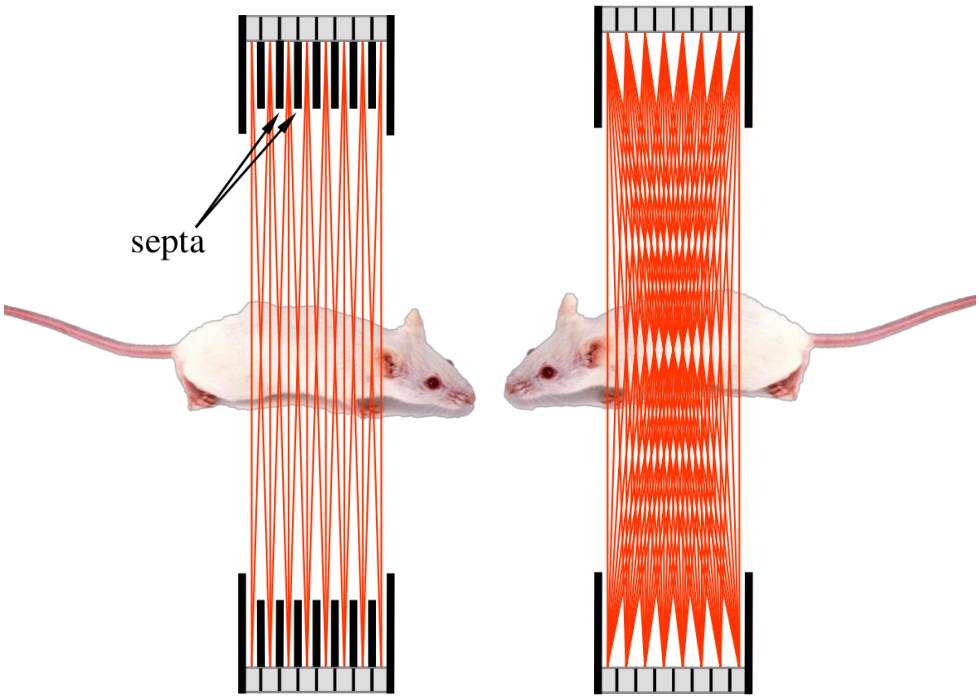

Figure 2.11: 2D mode (a) and 3D mode (b) in PET [25].

random and scattered photons. Detector pairs connected in coincidence in the same ring give a direct plane event, and coincidence events from a detector pair in two neighboring rings gives cross plane events. For an n-ring system, n direct planes and $n-1$ cross planes can be obtained, giving a total of $2n-1$ sinograms, each of which produces a transaxial image slice [26].

The sensitivity of a 2D PET scanner is good compared to other nuclear imaging, but PET sensitivity can increase even more by going from 2D acquisition to 3D acquisition. There are no septa present in a 3D mode, Figure 2.11b. This mode includes all coincidence events from all detector pairs, thus increasing the sensitivity by a factor of almost 4-8 over 2D mode acquisitions. But this also makes the mode more sensitive to effects of scatter and random coincidences [26].

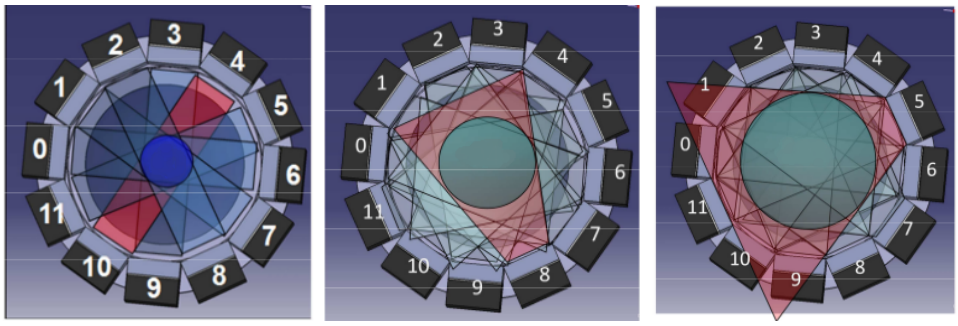

(a) (b) (c)

Figure 2.12: Coincidence mode: (a) 1-1, (b) 1-3 and (c) 1-5. The transaxial field of view (FOV) is shown by a circle; larger coincidence mode gives larger FOV [17].

Coincidence Mode

The coincidence mode decides the number of detectors on the opposite side that coincidence registration will be performed on. This is illustrated in Figure 2.12. Which number is preferred during a scan depends on the size of the scan object, as larger coincidence mode gives larger transaxial field of view (FOV). 1-3 coincidence can be a good choice for mice, while 1-5 coincidence might be better for rats. The highest coincidence mode is normally recommended at acquisition, as it is possible to modify this parameter during reconstruction. But larger coincidence mode result in longer reconstruction time, so it is not always recommended.

List Mode

List mode is a way of storing the raw data from the PET subsystem. The position of the registered photons interacting with the detectors are given in digitized X- and Y-signals, which in list mode are coded with “timestamps”. This is because they are received in sequence and stored as individual events as they occur. The parameters for each event in a module are saved in a file continuously [26].

There are different list mode types which can be used, e.g. *Fine Timestamp*, where every single event has a time stamp, and *Packet Timestamp*, where every packet of 1000 events has a timestamp, Figure 2.13 [17].

Sinogram

The sinogram is a method of storing and viewing processed PET data. In the sinogram, coincidence events in the PET scanner are categorized by plotting each line of response (LOR) as a function of its angular orientation versus

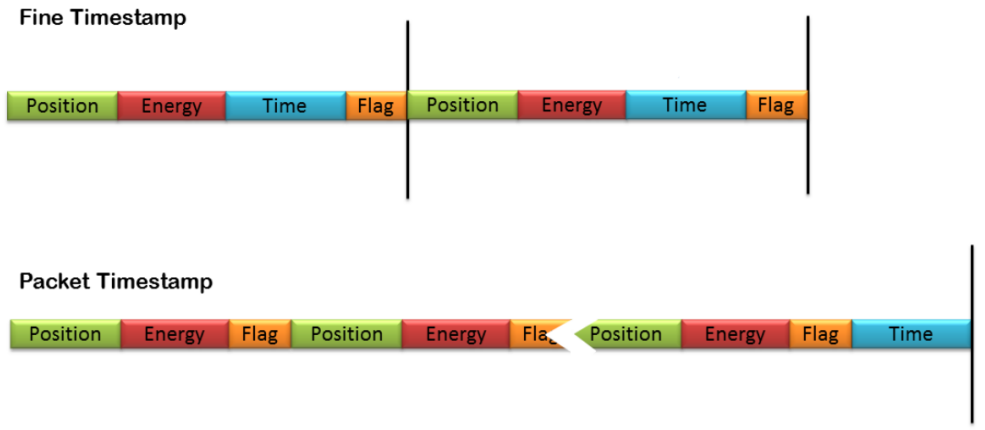

Figure 2.13: Data structure of fine timestamp (above) and packed timestamp (below) in list mode. Fine timestamp is timestamp in every event, packet timestamp is timestamp in every 1000 events [17].

its displacement from center of gantry [27], see Figure 2.14. Each LOR will therefore correspond to a point in the sinogram, and each sinogram will consist of all LORs in a given slice. Each sinogram will have enough information to reconstruct a slice image.

As each pixel in the sinogram is associated with a LOR, and therefore coincidence detection, the sum of all the pixel values in a sinogram is the equivalent to the total coincidence events detected corresponding to that slice. Figure 2.15 shows a sinogram of a point source placed in center of gantry. The black lines are due to the detector gaps, where the sensitivity of the detector ring is zero.

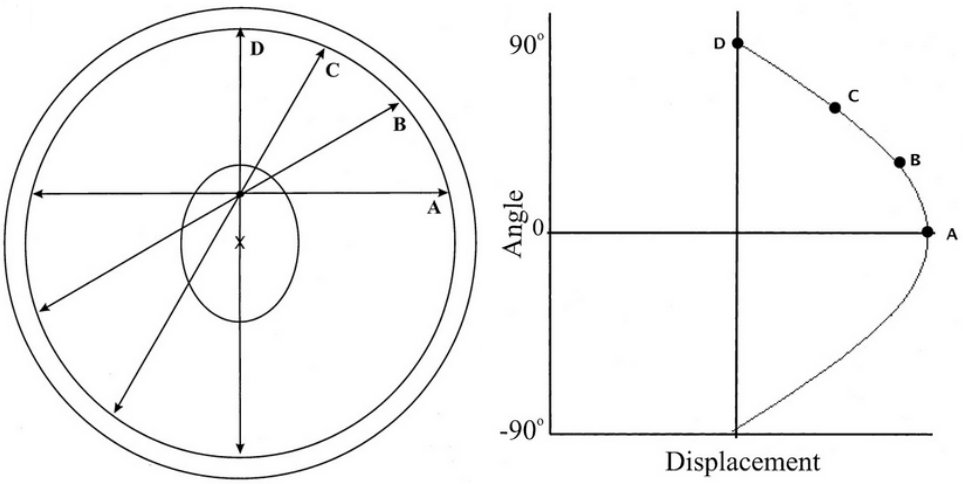

(a) (b)

Figure 2.14: In (a) four LORs are labeled A, B, C and D. These four LORs are plotted on a sinogram in (b), where the y-axis represents the angular orientation and the x-axis the displacement from center of gantry [27].

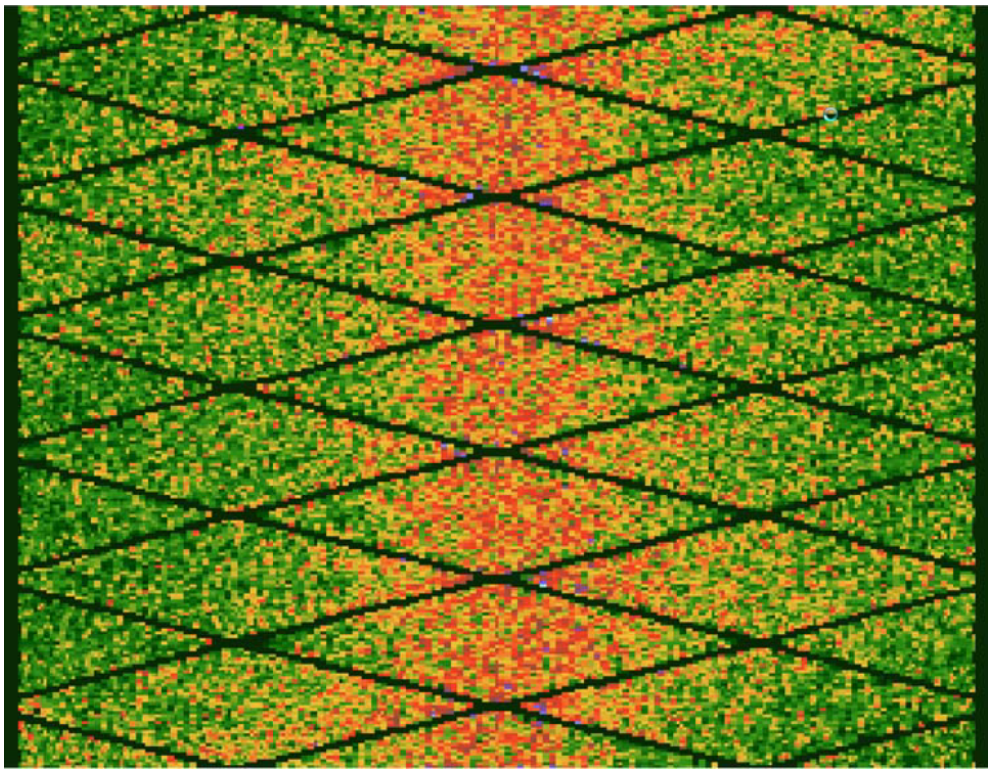

Figure 2.15: Example of a sinogram data file.

2.6.3 Factors Affecting Acquired PET Data

Normalization

Non-uniformity of the raw data due to the fact that the detection efficiency of a detector pair varies from pair to pair, can be corrected for in PET scanners. This correction method is called the normalization. The variation in detector efficiency comes from variations in the gain of photomultiplier tubes, detector locations, and the physical variation of the detector.

The normalization correction is done by giving each detector pair a normalization factor. The normalization factor is found by scanning a 511 keV photon source, and for each detector pair divide the average detector pair count by the individual detector pair count. This factor will then later be multiplied by the actual count, and the corrected count will be used to reconstruct the images [26].

Photon Attenuation

The annihilation photons can be attenuated before they reach the detectors. This causes non-uniformities in the images, because the longer the photons have to travel through tissue before reaching the detectors, the higher the probability is for the photons to be attenuated. As seen in Figure 2.16a, if a cylindrical phantom with homogeneous activity is scanned and then reconstructed without photon attenuation correction, it seems like there are more activity toward the edges than in the center of the phantom. Figure 2.16b shows the same image, but with attenuation correction. Here it is obvious that the phantom has homogeneous activity. The attenuation correction shown here is done by using the CT subsystem to get an attenuation map of the phantom. This attenuation map is scaled to reflect the attenuation of the PET photons, and then applied to the PET data to obtain the attenuation corrected image.

Random and Scatter Coincidences Events

Random coincidences and scatter coincidences give false lines of response, which give rise to noise in the images.

The amount of random coincidence events depend on many factors, e.g. the administered activity, time window of coincidence event detection, the energy window limits, and the scanning mode (2D vs. 3D) [21]. To estimate the number of random coincidence events, there are two standard strategies; a statistical calculation based on measured single events, and a direct measurement with the help of a delayed coincidence window [21].

Scatter coincidence events are a result of scattered photons. With PET energies, the photons have a high likelihood of undergoing Compton scattering. The photons lose energy when scattering, which makes it possible to reduce

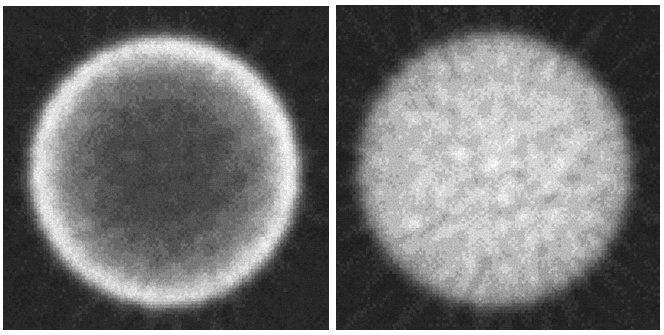

(a) (b)

Figure 2.16: Illustration of reconstruction artefacts resulting from lack of attenuation correction for uniform distribution of activity in a cylindrical phantom. Image of the phantom reconstructed (a) without attenuation correction and (b) with attenuation correction [28].

the scattered coincidence events by narrowing the energy window of the photon detection process.

2.6.4 Image Reconstruction

Image reconstruction in PET is the process of converting measurements of counts on a set of lines of response into a plot of the spatial location of the radiotracer. Image reconstruction is done by either analytic methods (e.g. filtered back-projection) or iterative methods. In iterative reconstruction, an initial estimate of an image is made, and the projections are computed from the image and compared with the measured projections. If there is a difference between the estimated and measured projections, corrections are made to improve the estimated image, and a new iteration is performed to assess the convergence between the estimated and measured projections [26].

Preclinical imaging systems typically provide both 2D and 3D reconstruction modes. 2D and 3D mode then refer to the reconstruction process and not to the type of image acquisition or final data format.

Reconstruction Algorithms in 2D

In 2D reconstruction only coincidences between detectors within the same ring or closely adjacent rings are permitted. Because of less data, the reconstruction process is faster in this mode than in 3D mode, but at the same time the sensitivity is poorer.

Available 2D algorithms are, in general, both analytic reconstruction algorithms like FBP, and iterative statistical reconstruction algorithm based on Expectation Maximization. 2D reconstruction is not the standard choice when

reconstructing. In this thesis FBP is the only 2D reconstruction algorithm used.

Preclinical scanners normally acquire 3D data, so the data have to be rebinned into a set of 2D equivalent projections before using 2D reconstruction. Single slice rebinning (SSRB) is a method where rebinning is achieved by assigning axially tilted LORs to transaxial planes intersecting at their axial midpoints. This is equivalent to collecting data in a multi-ring scanner in 2D mode.

Reconstruction Algorithms in 3D

3D reconstruction algorithms are generally iterative, like the Tera-Tomo reconstruction method. Tera-Tomo reconstruction [29] is a 3D iterative reconstruction method which uses EM and OSEM (Expectation Maximization and Ordered Subset Expectation Maximization) for reconstruction of PET images.

2.6.5 Radiation Dose from PET

The effective dose from a PET scan depends on the activity of the injected radiotracer, and on the radiotracer itself. The radiation dose from FDG to an adult is approximately 2×10^{-2} mSv/MBq [30]. At Haukeland University Hospital, the patients are routinely injected with approximately 370 MBq, regardless of patient size. Thus, the dose to patients at Haukeland University Hospital is normally 7-8 mSv per PET scan.

The injected activity in patients is not necessarily the same at other hospitals, as this depends on the procedure at the hospital. At Haukeland University Hospital, a new procedure is being planned, based on the EARL FDG-PET/CT accreditation program. The plan is to decide how much activity to inject based on the patient's weight, e.g. one activity for patients less than 60 kg, one for patients in the range 60-90 kg, and one activity for patients above 90 kg. The mice scanned at the preclinical scanner at Haukeland University Hospital are generally injected with 5-10 MBq activity.

2.7 Image Quality

2.7.1 Spatial Resolution

Spatial resolution is a measure of how closely two points can be to be distinguished after reconstruction. In the NEMA NU 4-2008 standard, spatial resolution is defined as the measured size of the reconstructed image of a point source, and is specified as the full width at half maximum (FWHM) or the full width at tenth maximum (FWTM).

The following factors affect the spatial resolution of a PET scanner [26]:

- **Detector size**
  The spatial resolution is greatly affected by the intrinsic resolution of the scintillation detectors used in the scanner. The intrinsic resolution, R_i, is, for a multidetector PET scanner, affected by the detector size d; $R_i = d/2$ at on the scanner axis at the midposition between the two detectors, and $R_i = d$ at the face of either detector. This makes the intrinsic resolution best at the center of the field of view (FOV).
- **Positron range**
  There will always be a degradation of spatial resolution due to positron range, as the point of interest is the positron emission, while the detection is related to the annihilation location.
- **Noncolinearity**
  If the positron still has some residual momentum when annihilating with an electron, it will result in two 511 keV photons which are emitted at not exactly 180°, but at $180° \pm 0.25°$. Thus, the observed LOR between the two detectors will not intersect directly at the point of annihilation. The degeneration of spatial resolution due to noncolinearity worsens with larger detector ring diameter, so this has a bigger effect on clinical scanners than on preclinical scanners.
- **Reconstruction method used**
  Noise introduced due to the reconstruction method will degrade the spatial resolution. As an example, filtered back-projection will introduce more noise than an iterative reconstruction method like the Tera-Tomo. Tera-Tomo will therefore have better spatial resolution than filtered back-projection.

2.7.2 Sensitivity

The sensitivity is a measure of the scanner's ability to detect photons from position-electron annihilations. It is defined as the number of counts per unit time detected by the device for each unit of activity present in the source, cps/kBq.

The sensitivity is calculated as follows:

$$S = \frac{R_{TOT}}{A}, \tag{2.14}$$

where R_{TOT} is the prompt (total) count rate and A is the activity at scan start. Count rates are given in counts per second.

Factors which affect the sensitivity of a PET scanner are [26]:

- **Geometric efficiency**
  Geometric efficiency is defined by the solid angle projected by the

source of activity at the detector. When increasing the solid angle, the sensitivity increases. The solid angle depends on the distance between the source and the detector, the diameter of the ring, and the number of rings; increasing the distance between source and detector reduces the solid angle.
Also, because of geometric efficiency, the sensitivity of the scanner will be highest at the center of the axial FOV and gradually decrease towards the periphery.

- **Detection efficiency**
  The detector efficiency depends on scintillation decay time and stopping power of the detector. The sensitivity of the PET scanner increases as the square of the detector efficiency (due to the need to detect both photons from an annihilation event).
- **Energy window settings**
  To set an energy window, a pulse height analyzer is used. The pulse height analyzer sorts out photons of different energies, and is essential for the scanner to count mainly unscattered photons. The narrower the window of the pulse height analyzer, the more accurate is the energy discrimination of photons from the sample, but the detection efficiency is reduced.
- **Dead time of the system**
  The dead time of a system is the time it takes for two 511 keV photons to each interact with a detector until the coincidence event is recorded. During this time the system is unable to process a second event, which will therefore be lost. With longer dead time, fewer events will be recorded, and therefore the sensitivity will be lower. Dead time is only a problem at very high activity.

2.7.3 Signal-to-Noise Ratio

For PET and CT images, the signal-to-noise ratio (SNR) is given as the ratio between the average signal value and the average standard deviation of the noise outside the object:

$$\text{SNR} = \frac{\text{Signal value}}{\text{Standard deviation of noise}}. \tag{2.15}$$

In PET the signal value is given in standardized uptake values, and in CT it is given in Hounsfield units (HU).

For CT scanners, the SNR value is proportional to the following:

$$\text{SNR} \propto \sqrt{\frac{\epsilon \cdot \text{mAs} \cdot S}{I_0/I}}, \tag{2.16}$$

where ϵ is the efficiency of the system, mAs is the product of tube current and exposure time, S is the slice thickness, and I_0/I is the x-ray's initial intensity divided by the detected intensity [1].

It is an advantage to have as high SNR as possible, but at the same time this would need a higher mAs, and therefore more dose and/or longer scan time, which can be a disadvantage.

Noise Equivalent Count Rate

Image noise is the random variation in pixel counts across the image and is inverse proportional to the square root of the counts in a pixel. Image noise can therefore be reduced by increasing the total counts in the image, but it is not always possible to increase the counts, since this requires either longer scan time, injecting more activity into the patient, or improving the detector efficiency of the scanner [26].

The noise equivalent count rate (NECR) is a parameter which characterizes the image noise, and it is given by

$$\text{NECR} = \frac{R_t^2}{R_{TOT}}, \tag{2.17}$$

where R_t is the true coincidence count rate and R_{TOT} is the prompt coincidence count rate.

The NECR is proportional to the signal-to-noise ratio in the final reconstructed images. This makes it a good parameter to compare the performance of different PET scanners which does not have a wide variation in design. Image noise can be minimized by maximizing NECR [26].

Scatter Fraction

Scatter is expressed by scatter fraction, SF, which is a measure of the relative system sensitivity to scatter radiation. Scatter fraction is given by

$$\text{SF} = \frac{R_s}{R_{TOT}}, \tag{2.18}$$

where R_s and R_{TOT} are the scattered and prompt count rates, respectively. The performance of the scanner and the quality of the images are better the lower the SF value [26].

2.7.4 Uniformity and Partial Volume Effect

The image uniformity in PET is a measure of the attenuation and scatter correction performance. Also, the noise in a uniform region of a phantom is indicative of the signal-to-noise ratio performance of the imaging system [4].

The reconstructed PET images should display the radiotracer distribution uniformly and accurately throughout the FOV. However, hot (radioactive) structures smaller than twice the scanner resolution, in a cold (non-radioactive) background show partial loss of intensity. This is because of limitations in spatial resolution. The total counts however, are preserved by making the object appear to be larger, with a lower activity concentration than it actually has. Similarly, a cold spot relative to a hot background would appear smaller with a high activity concentration [26].

Such underestimation and overestimation of activities around smaller structures in reconstructed images are called the partial volume effect, and this reduces the contrast between high and low uptake regions. This effect also contains the spill-over effect due to contamination of activity from the neighboring tissues to these hot or cold areas [26]. Measurements of the partial volume effect are given in recovery coefficients and spill-over ratios.

The recovery coefficient is the ratio of the reconstructed count density to the true count density of a region of interest smaller than twice the spatial resolution of the system. The spill-over ratio is the mean activity concentration measured in a cold (non-radioactive) region divided by the mean activity concentration in a hot (radioactive) uniform region. The activity measured in the cold regions is indicative of the scatter correction performance [4].

2.7.5 Artefacts

Artefacts are false structures in the images which do not have counterparts in the physical object being imaged. Artefacts degrade image quality. Two types of artefacts often encountered in CT/PET are ring artefacts and attenuation correction artefacts.

Ring artefacts are often present in high resolution small-animal CT scanners. Ring artefacts are concentric rings in the images around the center of rotation of the CT setup, which are caused by imperfect detector elements [18]. Ring artefacts can be reduced by different approaches. One approach is to move the detector array during the acquisition, as done in the semicircular acquisition method. This averages all the detector elements, which usually leads to significantly reduced ring artefacts [31].

Attenuation correction artefacts can arise in PET images, due to the fact that the images have been attenuation corrected using a CT scan. These artefacts arise when there are materials presents, like a contrast agent or metallic implants, which do not behave like air, water or bone. In these materials, photons with CT energies and photons with PET energies will behave differently, and thus give rise to artefacts when using CT to correct PET images.

2.8 The NEMA NU 4-2008 Standard

The National Electrical Manufactures Association (NEMA) was founded in 1926, and is the association of electrical equipment and medical imaging manufacturers [32]. NEMA is the leader in standardization of electrical equipment, and the NEMA NU 2 standard[1] has since the early 1990s been the standard performance evaluation method of clinical PET scanners.

More recently a NEMA standard for preclinical PET systems was developed, as the demand has grown for a standardized performance evaluation of preclinical scanners. This standard is called the NEMA NU 4-2008 standard. Before the NEMA NU 4-2008 standard, performance evaluation of preclinical scanners were done by modifying the NEMA NU 2 standard, making comparisons between systems difficult.

The NEMA NU 4-2008 standard includes evaluation of spatial resolution, counting rate capabilities, sensitivity and image quality. The methods in this standard are further described in Chapter 3.

The main part of this thesis was to complete a performance evaluation of the PET subsystem of a small-animal PET/CT scanner, mainly according to the NEMA NU 4-2008 standard. Many preclinical scanners have already been performance evaluated according to this standard. There are three completed performance evaluations which are of special interest to this thesis:

- A vendor dependent performance evaluation of a random nanoScan PET/CT system, included in the small-animal PET/CT system's purchase contract.
- Szanda et al. (2011): *National Electrical Manufacturers Association NU-4 Performance Evaluation of the PET Component of the NanoPET/CT Preclinical PET/CT Scanner*
- Nagy et al. (2013): *Performance Evaluation of the Small-Animal nanoScan PET/MRI System*

These three performance evaluations can be expected to give similar results to the performance evaluation in this thesis, since the scanners are from the same vendor and they are quite similar. The nanoScan PET/MRI system and the nanoScan PET/CT system have almost identical PET scanners, except for the reinforced magnetic shielding and a radiofrequency shield inside the PET ring in the nanoScan PET/MRI system [33]. The nanoPET/CT is an older version of the nanoScan PET/CT system.

However, a comparison of PET systems from the same vendor is not enough, as this does not say how good the scanner is in general. The following articles are of interest when comparing preclinical PET scanners:

[1]The most updated NEMA NU 2 version is the NEMA NU 2-2012. Older versions are NEMA NU 2-1994, NEMA NU 2-2001 and NEMA NU 2-2007.

- Yao et al. (2012): *Small-Animal PET: What Is It, and Why Do We Need It?*
- Goertzen et al. (2012): *NEMA NU 4-2008 Comparison of Preclinical PET Imaging Systems*

A summary of these articles and the vendor evaluation of a nanoScan PET/CT system is given in the next four subsections, each subsection going through one part of the NEMA NU 4-2008 standard. The performance data are also listed in Appendix A.

2.8.1 Spatial Resolution

The best spatial resolutions reported for small-animal PET systems have been about 1 mm in full width at half maximum. The state-of-the-art human PET systems achieve a spatial resolution of 6 mm. When comparing a typical mouse and a typical rat to an average-sized adult, the mouse is scaled down by a factor of approximately 15 in size, and the rat is scaled down by a factor of approximately 6 in size. Compare this to the 6 mm resolution of a clinical PET scanner; the small-animal PET would need to have a spatial resolution of 0.4 mm for mouse imaging and of 1 mm for rat imaging to distinguish the same level of structural detail in images. The resolution capability of small-animal PET is close to what is needed for rat imaging but not yet fully optimal for mouse imaging [3].

- **The nanoScan PET/CT System (performance evaluated by vendor)**
  The vendor has not done this part of the performance evaluation completely as described in the NEMA NU 4-2008 standard, as the standard states that the reconstruction should be done with filtered back-projection, and both the FWHM and FWTM (full width at half or tenth maximum) at positions 5 mm, 10 mm, 15 mm and 25 mm from transaxial field of view (FOV) should be reported. Instead the reconstruction method used was OSEM (ordered subset expectation maximization), and only FWHM values were reported, at 1 mm, 10 mm and 25 mm.
  At 1 mm radial distance from center of FOV, the spatial resolution was approximately 1 mm for radial and tangential FWHM resolution, and 1.3-1.4 mm for axial FWHM resolution. All FWHM resolutions measured were less than 2 mm [17].
- **The NanoPET/CT System**
  The performance evaluation by Szanda et al. (2011) did not include a table with the spatial resolution results; instead the results were given in a figure, Figure A.1. The reconstruction algorithm was filtered back-projection.

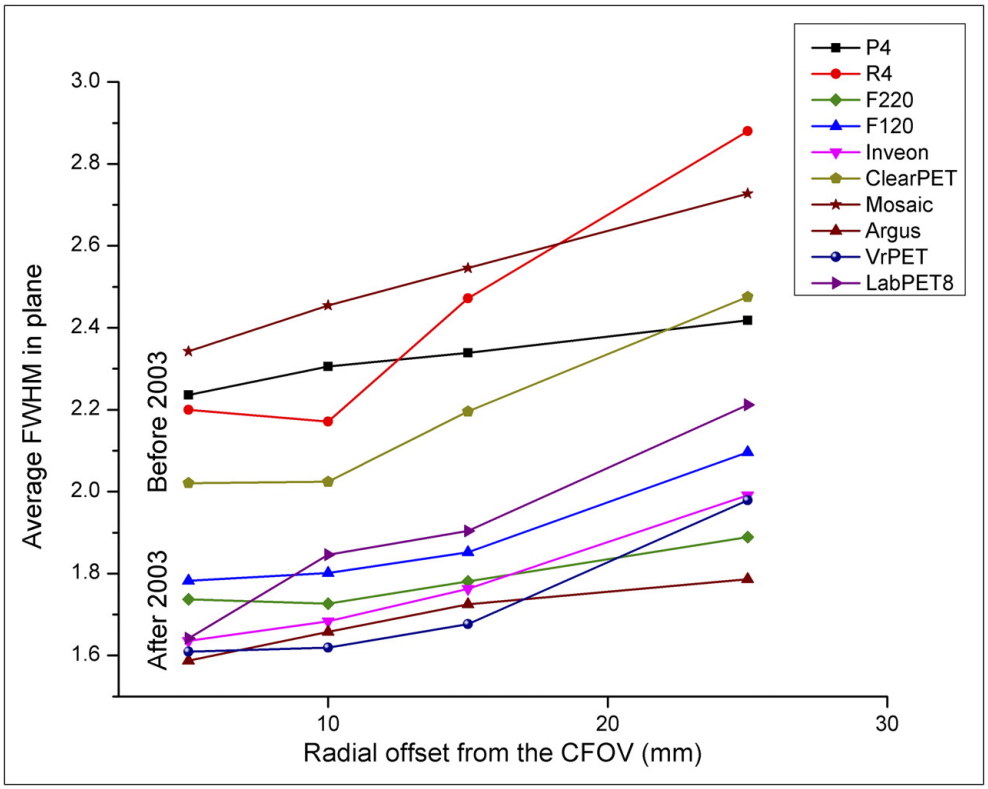

Figure 2.17: Comparison of spatial resolution of first-generation PET systems, i.e. systems manufactured before 2003, with later-generations [35].

In the center of transaxial FOV, the scanner resolution (FWHM) approached 1 mm. Over the central 10 cm transaxial region, the scanner resolution remained under 2.0 mm [34].

- **The nanoScan PET/MRI System**
  The reconstruction algorithm was filtered back-projection, and the FWHM resolution remained under 2.0 mm within the central 15 mm transaxial region [33].

Goertzen et al. (2012) found that spatial resolution was generally better at the 1/4-axial-offset position than at the center, particularly for axial resolution, because of the more oblique lines of response used by the central position than by the 1/4-axial-offset position [35].

A comparison of spatial resolution is given in Figure 2.17, which shows an improvement in spatial resolution for newer scanners.

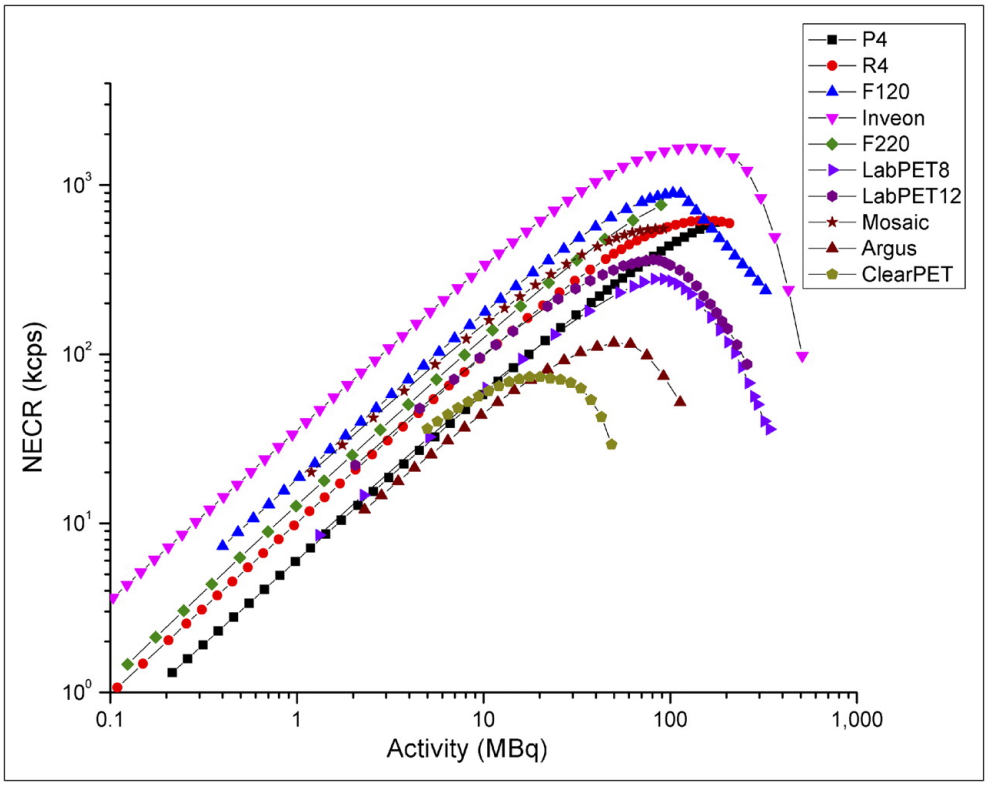

Figure 2.18: Plot of noise equivalent count rate (NECR) vs. activity for mouse-sized phantom, various scanners [35].

2.8.2 Scatter Fraction, Count Losses, and Random Coincidence Measurements

The animals scanned in the small-animal scanner are much smaller than humans. The amount of scattered events and the magnitude of attenuation are therefore much less in small-animal PET scanners than in human PET scanners.

- **The nanoScan PET/CT System (performance evaluated by vendor)**
  This part of the NEMA NU 4-2008 standard was not evaluated by the vendor.
- **The NanoPET/CT System**
  The peak of the noise equivalent count rate (NECR) curve was 430 kcps at 36 MBq for the mouse phantom. The scatter fraction was 15% [34].
- **The nanoScan PET/MRI System**
  The peak true counting rate was 692 kcps at 1.090 MBq/ml and the peak NECR was 406 kcps at 0.847 MBq/ml for the mouse-like phantom. The scatter fraction was 17.3% [33].

Goertzen et al. (2012) found that the scatter fraction was generally lowest for large-ring systems and for narrow energy windows. The system with lowest observed scatter fraction here was the microPET P4 with a scatter fraction of 5.2%, and the highest was the ClearPET with a scatter fraction of 31% [35].

Preclinical systems from different vendors have a much wider variation in design compared to clinical PET scanners. Because of this wide variation, it is difficult to directly use NECR for comparing systems. Figure 2.18 shows the NECR curves for the systems evaluated in Goertzen et al. (2012), and it is clear that although they are similar in shape the NECR curves are still quite different from each other. Below the peak NECR value, all systems have a linear range of the NECR-versus-activity level [35], when plotted logarithmic.

2.8.3 Sensitivity

Most small-animal PET systems have the same cylindrical geometry as human PET systems, but with a smaller detector ring. Since the detector ring has smaller diameter, the small-animal PET system can have more detectors in the axial direction and still have a similar number of detector channels as used for human PET. The highest reported absolute sensitivity at the center of FOV for state-of-the-art small-animal PET systems is approximately 10%, which is about 3 times that of a conventional human PET scanner [3].

- **The nanoScan PET/CT System (performance evaluated by vendor)**
  The absolute sensitivity at center of FOV was 9%, and it was 5% at 25 mm from center of FOV [17].
- **The NanoPET/CT System**
  The absolute sensitivity at the center of FOV was 7.7%. The average absolute sensitivity for mouse-sized region was 5.15% [34].
- **The nanoScan PET/MRI System**
  The absolute sensitivity at the center of FOV was $\sim$ 8.5%. The absolute sensitivity for mouse-sized region was 5.83% [33].

Goertzen et al. (2012) found that the largest factor affecting detection efficiency is the solid-angle coverage of the detector ring, with higher values for long-axial-FOV and small-ring systems. The peak detection efficiency is the same as the absolute sensitivity at center of FOV, and for the scanners evaluated by Goertzen et al. (2012), the absolute sensitivity at center of axial FOV was in the range 1.19% - 6.72% [35].

In Goertzen et al. (2012), the scanners from before 2003 had absolute sensitivity at center of axial FOV in the range 1.19% - 3.03%, and the scanners from after 2003 in the range 2.22% - 6.72% [35].

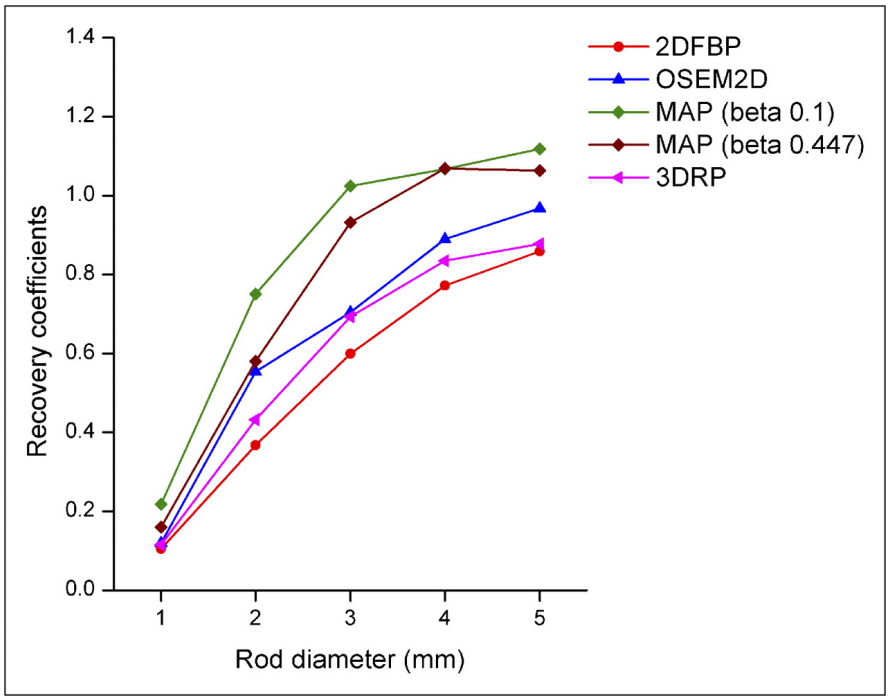

Figure 2.19: Recovery coefficients for microPET P4 system for 5 reconstruction algorithms. MAP = maximum a posteriori; OSEM2D = 2-dimensional ordered-subsets expectation maximization; 3DRP = 3-dimensional reprojection; 2DFBP = 2-dimensional filtered back-projection [35].

2.8.4 NEMA Image Quality Phantom Study

This test is to measure how good the scanner is at attenuation and scatter correction performance. Small-animal PET scanners usually use the same attenuation and scatter correction techniques as human PET scanners.

- **The nanoScan PET/CT System (performance evaluated by vendor)**
  The Tera-Tomo reconstruction had a lower percentage standard deviation (%STD) than OSEM reconstruction; a %STD of 9.5% for OSEM and 2.74% for Tera-Tomo. The recovery coefficients were only given for Tera-Tomo reconstruction. The 1 mm diameter rod had a recovery coefficient less than 0.3, while the other rods had recovery coefficients close to 1. The spill-over ratios were also lower for Tera-Tomo reconstruction (0.06 and 0.05 for water and air, respectively) than for OSEM (0.07 and 0.06 for water and air, respectively) [17].
- **The NanoPET/CT System**
  The %STD of the uniformity region was 8%. The recovery coefficient was less than 0.2 for the rod with 1 mm diameter, less than 0.6 for the rod with 2 mm diameter and close to 1 for the other rods. Spill-

over ratio was 0.08 and 0.20 for water and air, respectively. The reconstruction was done with MLEM (maximum-likelihood expectation maximization) [34].

- **The nanoScan PET/MRI System**
  The %STD of the uniformity region was 3.52%. The recovery coefficient for the 1 mm diameter rod was less than 0.3. The recovery coefficients started approaching 1 already at the rod with 2 mm diameter. The reconstruction was done with Tera-Tomo reconstruction [33].

The results in this test are highly dependent on the reconstruction algorithm and corrections applied. Goertzen et al. (2012) illustrated this by plotting the recovery coefficients of the micro PET P4 system for five reconstruction algorithms, Figure 2.19.

This variability in results in a system using different reconstruction algorithms makes it difficult to compare the results from this test across systems from different vendors.

2.9 Motivation

The aim of this thesis was to evaluate the performance of a small-animal PET/CT system. Such a vendor-independent evaluation is needed when initiating research on a novel installation, particularly when quantitative measurements rather than qualitative assessments are sought. The work in this thesis is therefore timely and of high importance to all imaging experiments being performed on the system. The performance evaluation is done in multiple steps:

CT subsystem;

- Evaluation of the system's ability to accurately reproduce known signal intensities (Hounsfield units).
- Evaluate variations in noise distribution across FOV and compare with vendor provided maintenance procedures.
- Evaluate the effect of reconstruction filters on noise variation.
- Evaluate various scan methods by comparing scan time, dose, artefacts and signal-to-noise ratio.

PET subsystem;

- Measuring spatial resolution using a point source.
- Evaluation of the system's counting rate abilities, by scanning a line source while the activity in the phantom decay over several half-lifes.
- Measure the sensitivity across the axial FOV using a point source.
- Evaluate image uniformity (%STD) and partial volume effects (recovery coefficients and spill-over ratio).

Chapter 3

Materials and Methods

This chapter begins with a description of the nanoScan PET/CT system and a presentation of the phantoms used in this evaluation. A description of the methods used for evaluating the PET/CT system is included.

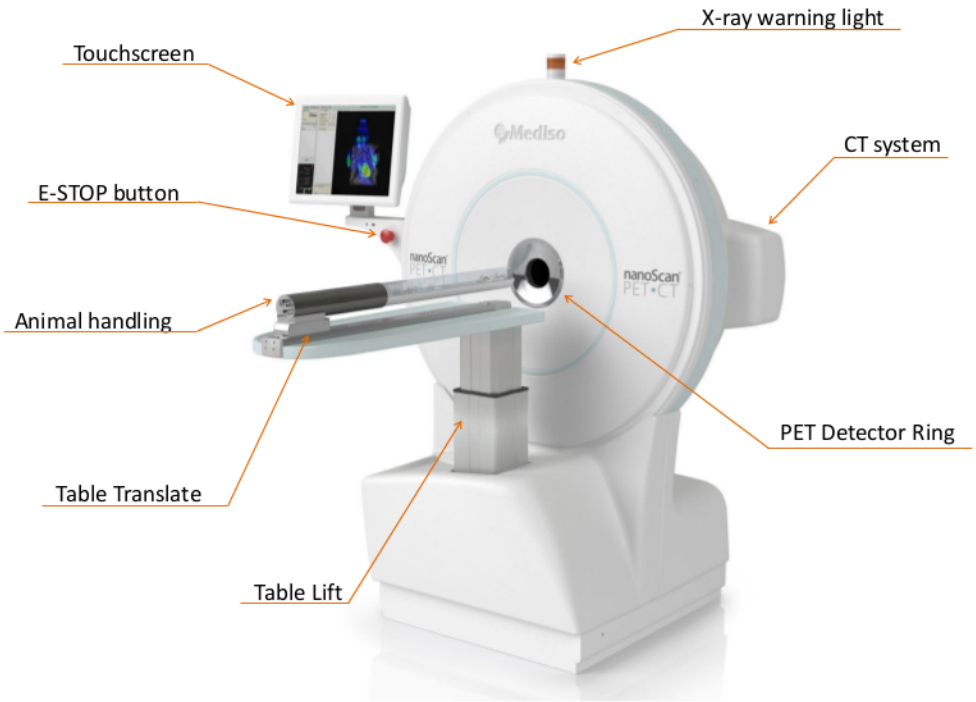

Figure 3.1: The nanoScan PET/CT system with description [17].

3.1 Scanner Description

In this thesis, all data acquisition were performed using the nanoScan PET/CT system (Mediso, Budapest, Hungary), Figure 3.1. This is a high sensitivity, high resolution and fully integrated small-animal PET/CT system.

CT Subsystem

The nanoScan CT is a cone-beam in vivo CT scanner. For design description of the CT subsystem, see Table 3.1.

The scanner uses multiple GPUs (Graphical Processing Unit) for reconstruction. Reconstruction is done according to the FDK method, which is a filtered back-projection method, with following available filters: RamLack, Hamming, Hann, Shepp-Logan, Butterworth, Cosine and BlackMan.

PET Subsystem

The PET system has 12 detector blocks of 81×39 Lutetium Yttrium Orthosilicate (LYSO) crystals (1.12 mm$\times$1.12 mm$\times$13 mm), tightly packed (pitch 1.17 mm, packing fraction 92%) coupled to two 256-channel position sensitive photomultiplier tubes. The detector blocks are mounted in rings of diameter 184 mm, and there are 81 rings in total, see Table 3.2.

PET data are acquired in list mode, and list mode data can be sorted into 3-dimensional (3D) sinograms or into 2-dimensional (2D) sinograms by single-slice rebinning (SSRB).

3.2 Image Data

The acquired data in this thesis were either given as DICOM files or as sinogram files. The image data were either analyzed in InterView FUSION, which is a visualization and evaluation software developed by Mediso, or in-house developed Python scripts. All Python scripts were developed as a part of this thesis. Abbreviated versions of the scripts are included in Appendix B.

DICOM

The reconstructed images are stored as DICOM files. DICOM is short for Digital Imaging and Communications in Medicine. This is a standard for handling information in medical imaging, and it includes a file format definition and a network communications protocol [36].

Detector	
Type	Flat panel CMOS technology
Detector material	Gd_2O_2S
Detector size	15×12 cm^2
Detector pixel number	3M Pixel
X-ray tube	
Maximum tube current	0.18 mA
Tube voltage range, standard	30-80 kV_p
Tube power	50/80 W

Table 3.1: Design description of the CT subsystem.

Detector	
Crystal material	LYSO
Crystal size (mm^3)	$1.12 \times 1.12 \times 13$
Crystal pitch (mm)	1.17
Packing fraction	92%
Crystal array	81×39
System	
No. of detector blocks/module	12
No. of crystals	37908
No. of rings	81
No. of crystals per ring	468
Ring diameter (cm)	18.4
Gantry aperture (cm)	16
Axial FOV per bed position (cm)	9.4 (up to 280 mm)
Transaxial FOV (cm)	12.3
Solid angle/4π	0.219
Dataset	
No. of sinograms	161 (SSRB)
Sinogram size	410×240
Sampling distance (mm)	0.3

Table 3.2: Design description of the PET subsystem.

Sinogram

The sinograms from the nanoScan PET/CT system are in MINC format, which is basically NetCDF. Due to "historical reasons", the nanoScan PET/CT system's MINC handling software is not fully standard compliant. A script which converts sinograms into pixel arrays in Python is included in Appendix B.

3.3 Phantoms and Point Sources

Phantoms are objects used to evaluate the image quality of a scanner. This section describes the phantoms used in this thesis.

CT Image Quality Phantom (Mouse Size)

The CT image quality phantom, Figure 3.2 and Table 3.3, is a 60 mm long cylindrical phantom. The CT image quality phantom consists of two cylindrical compartments, as seen in the drawing of the phantom in Figure 3.2b. One of the compartments is filled with water, and the other with air.

Total length	60 mm
Outer diameter	30 mm
Inner diameter	26 mm
Length water/air compartments	20 mm

Table 3.3: Dimensions, CT image quality phantom.

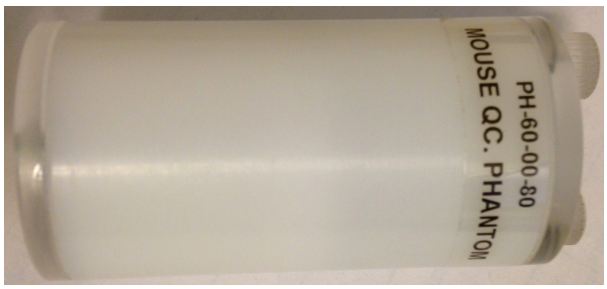

(a)

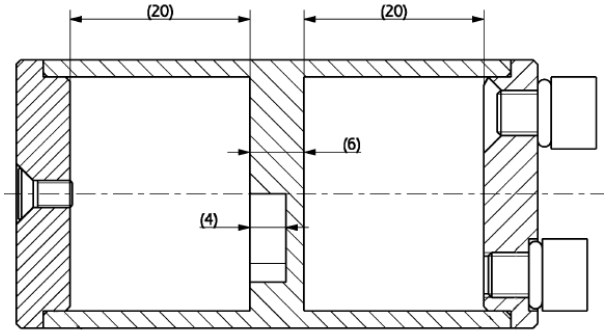

(b)

Figure 3.2: The CT image quality phantom (mouse size); (a) picture of the phantom and (b) schematic drawing of the phantom with dimensions given in mm.

The nanoScan Jaszczak Phantom

The nanoScan Jaszczak phantom, Figure 3.3a and Table 3.4, is a rod phantom with fillable rods of six different sizes. The rods are arranged as shown in Figure 3.3b and Figure 3.3c.

Total length	24 mm
Diameter	25 mm
Diameter, rods	0.7 - 1.2 mm
Length, rods	12 mm

Table 3.4: Dimensions, nanoScan Jaszczak phantom.

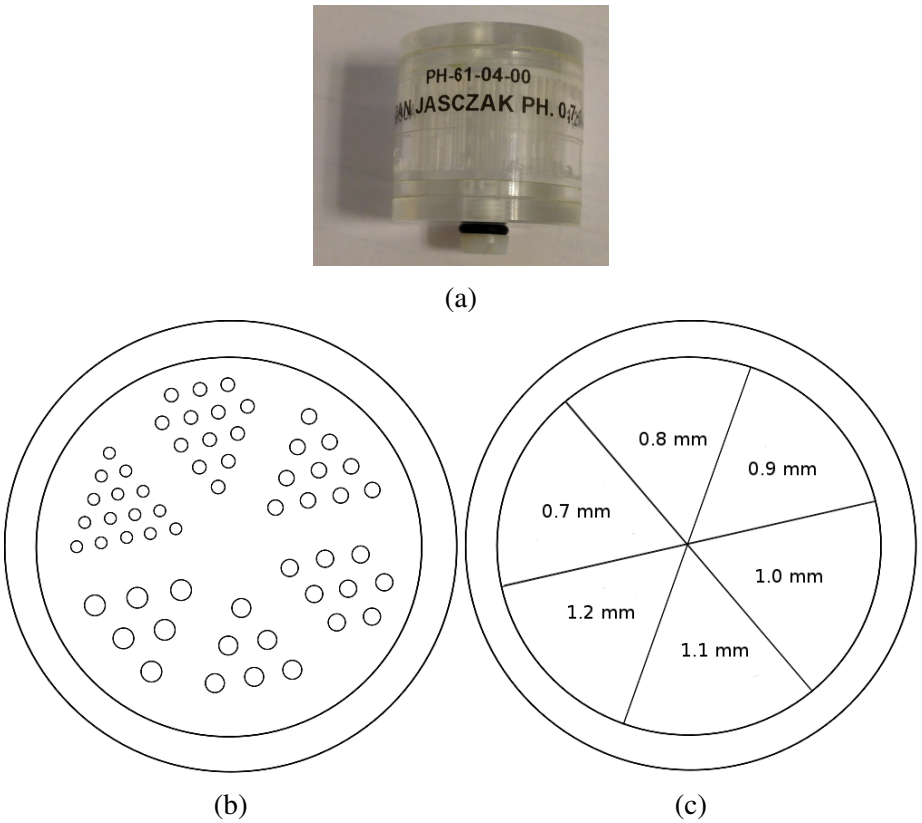

(a)

(b) (c)

Figure 3.3: The nanoScan Jaszczak phantom (a), with arrangements of rods (b), and the rod diameters (c). The rods have a diameter of 0.7 mm, 0.8 mm, 0.9 mm, 1.0 mm, 1.1 mm and 1.2 mm.

The Standard NEMA Point Source

The standard NEMA point source, Figure 3.4, is a small quantity of ^{22}Na confined to no more than 0.3 mm in all directions, embedded in an acrylic cube with 10.0 mm side lengths.

^{22}Na has a half-life of 2.6 years. The activity of the ^{22}Na point source used in this thesis was 370 kBq on April 1, 2013, and all the tests were done within a year after this. Alessio et al. (2005), [37], showed that ^{22}Na and ^{18}F have very similar positron ranges, which justifies the use of ^{22}Na for system response function measurements.

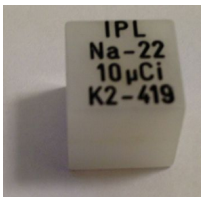

Figure 3.4: The standard NEMA ^{22}Na point source.

Mouse-Like Phantom

The mouse-like phantom, Figure 3.5 and Table 3.5, is a solid cylinder composed of high density polyethylene (density 0.96 $\pm$ 0.1 g/cm^3). A cylindrical hole of 3.2 mm is drilled into the cylinder, parallel to the central axis at the radial distance of 10 mm. A line source, i.e. a clear flexible tubing with a fillable section, can be inserted into this hole.

Length	70 mm
Diameter	25 mm
Diameter, cylindrical hole	3.2 mm
Distance between central axis and hole	10 mm

Table 3.5: Dimensions, mouse-like phantom.

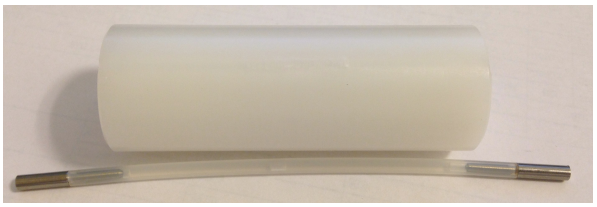

Figure 3.5: The mouse-like phantom. The clear flexible tubing can be inserted into a cylindrical hole, 10 mm from the central axis of the phantom.

NEMA Image Quality Phantom

The NEMA image quality phantom, Figure 3.6 and Table 3.6, is supposed to mimic a typical imaging condition. The phantom is made of polymethylmethacrylate, and consists of three parts; a fillable 5-rod region, a fillable uniform region and a 2-chamber region (air/water chambers), as seen in Figure 3.7.

The 5-rod region is a 20 mm long solid region with 5 fillable rods drilled through (at 7 mm from the center). The five rods have diameters 1 mm, 2 mm, 3 mm, 4 mm and 5 mm, respectively. The remaining 30 mm of the phantom is a fillable cylindrical chamber which consists of a uniform region and two chambers. The two chambers are to be filled with non-radioactive water and air. The water is to simulate attenuation only.

Internal length	50 mm
Internal diameter	30 mm
Length, 5-rod region	20 mm
Diameter, rods	1 - 5 mm
Length, fillable cylindrical chamber	30 mm
Length, cold region chambers	15 mm
Internal diameter, cold region chambers	8 mm

Table 3.6: Dimensions, NEMA image quality phantom.

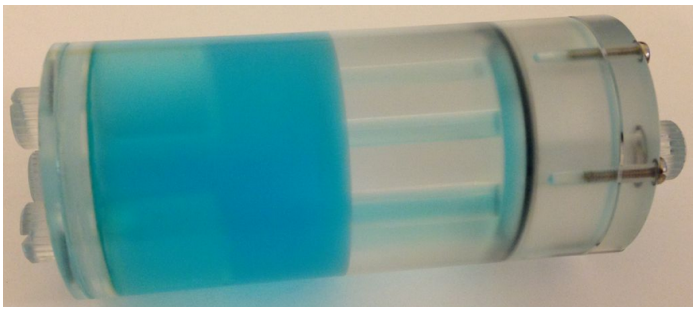

Figure 3.6: The NEMA image quality phantom.

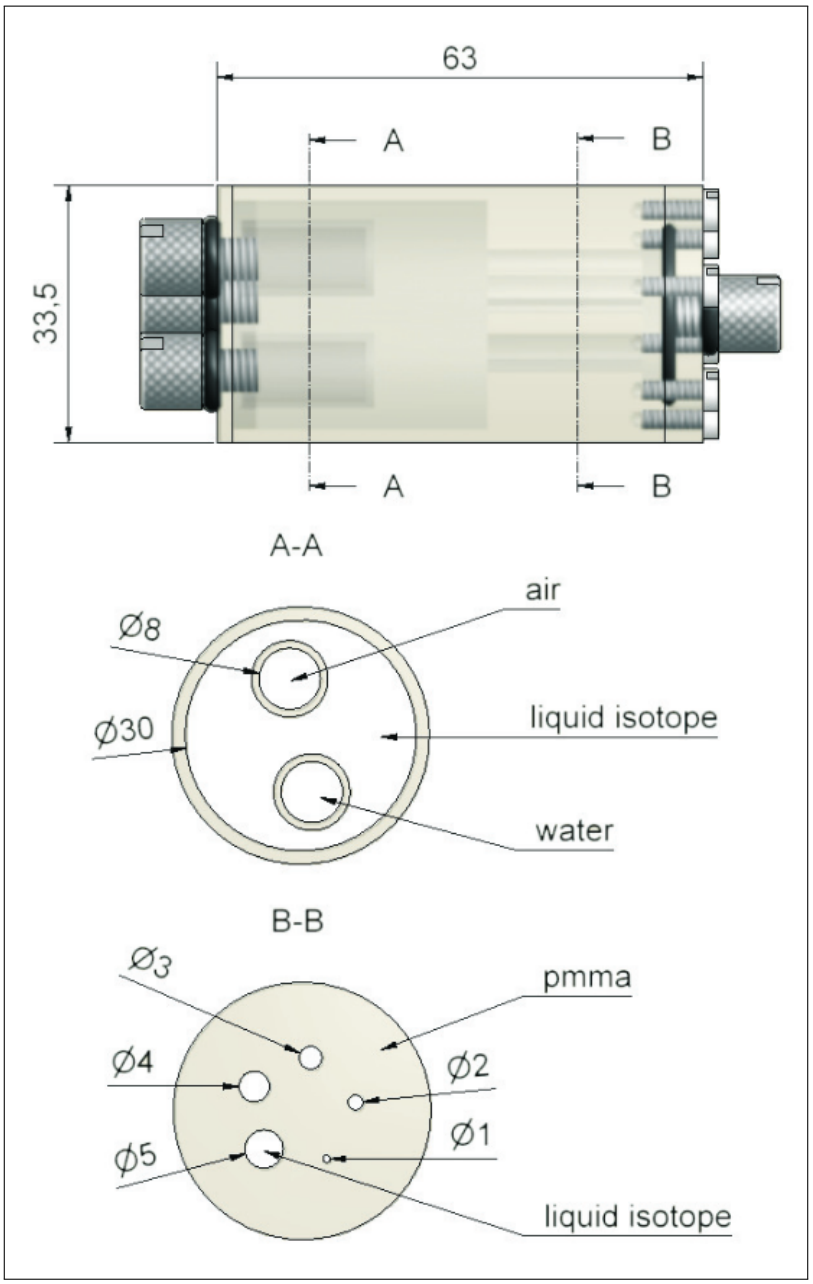

Figure 3.7: Schematic drawing of the NEMA image quality phantom, with dimensions in mm [38].

3.4 Evaluation of the CT Subsystem

The CT evaluation was not as standardized and comprehensive as the evaluation of the PET subsystem. This evaluation started by reproducing the automatic Hounsfield quality check, which is a vendor provided CT quality control software which is supposed to be performed on a weekly basis.

Then, the different reconstruction filters were compared, to see if different filters produced a significant difference in the reconstructed images. The CT evaluation ended with a comparison of different scanning methods, to get an insight in the positive and negative aspects of each method.

3.4.1 Hounsfield Quality Check

The CT image quality phantom (mouse size) consists of water and air, and can therefore be used to check how the CT-numbers (Hounsfield units) of water and air in images differs from the defined CT-numbers of water and air. The phantom was scanned using the "semicircular, half scan" method, and with all available tube voltages and exposure times. The acquisition parameters are given in Table 3.7, and the images were reconstructed using the FDK algorithm with the RamLak filter.

Two measurements were done on the reconstructed images; image noise measurement and image homogeneity measurement. In the image noise measurement, a large region of interest (ROI) with a diameter of 24 mm was placed on the central slice of the water compartment and on the central slice of the air compartment, as illustrated in Figure 3.8a. In the image homogeneity measurement five small ROIs with diameters of 6 mm were placed in the center and at 3h, 6h, 9h and 12h, on the central slice of the water compartment and on the central slice of the air compartment, see Figure 3.8b.

The phantom was also scanned with the automatic Hounsfield quality check. The acquisition settings for this protocol, as described by the vendor, are provided in Table 3.8. The reconstruction was done using FDK algorithm with the RamLak filter. The ROIs in the automatic test are, like the non-automatic test, as described in Figure 3.8.

3.4.2 Noise in Reconstruction Filters

The CT image quality phantom (mouse size) was scanned with acquisition parameters given in Table 3.9. Reconstructions were done using the FDK algorithm with all the available reconstruction filters.

To evaluate the noise in the different reconstruction filters, a ROI with a 12 mm diameter was placed on the central slice of the water compartment

Acquisition mode	Semicircular, half scan
Number of projections	720
Tube Voltage	All kV_p
Tube current	All μA
Exposure time	All ms
Magnification	Maximum Zoom

Table 3.7: CT acquisition parameters, non-automatic Hounsfield quality check. The number of projections means the angular sampling per single 360° rotation.

Acquisition mode	Semicircular (not specified as half or full scan)
Number of projections	360
Tube Voltage	All kV_p
Tube current	All μA
Exposure time	All ms
Magnification	Maximum FOV

Table 3.8: CT acquisition parameters, automatic Hounsfield quality check.

Acquisition mode	Semicircular, half scan
Number of projections	720
Tube Voltage	70 kV_p
Tube current	310 μA
Exposure time	300 ms
Magnification	Maximum Zoom

Table 3.9: CT acquisition parameters, noise in reconstruction filters.

and on central slice of the air compartment, see Figure 3.9. For each filter, the mean CT number and the standard deviation of noise were measured.

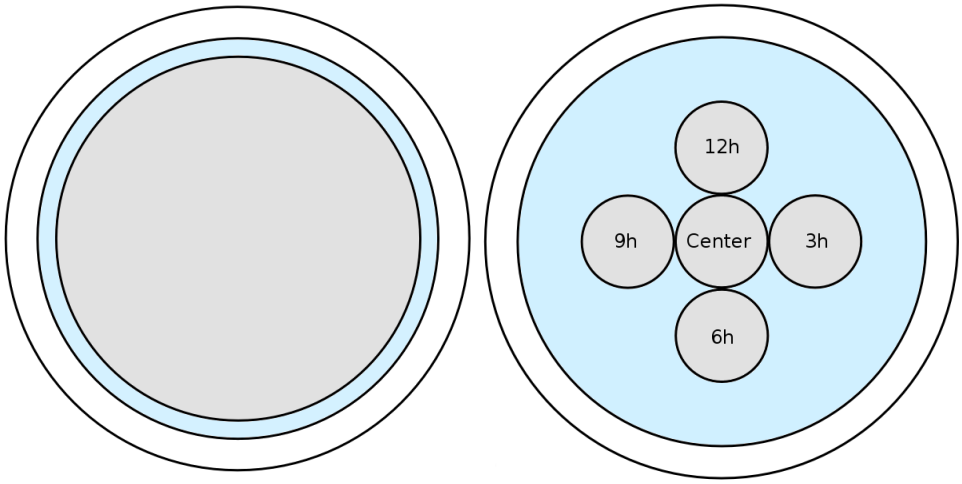

(a) (b)

Figure 3.8: Placement of ROIs, Hounsfield quality check. The ROIs (gray) are placed the in water and in the air compartment (blue). The ROI in (a) has a diameter of 24 mm and is used for image noise measurements, and the ROIs in (b) have diameters of 6 mm and are used for image homogeneity measurements.

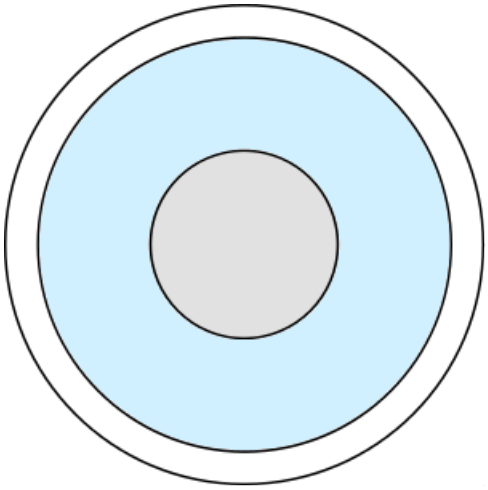

Figure 3.9: Placement of ROIs, noise in reconstruction filters test. The ROIs (gray) is placed in the water and in the air compartment (blue). The ROI has a diameter of 12 mm.

3.4.3 Different Scanning Methods

The system is delivered with four scanning options on the CT subsystem, “semicircular, full scan”, “semicircular, half scan”, “helical, 0.5 pitch” and “helical, 1 pitch”. It is important to understand the advantages and disadvantages of these methods in order to determine in which experimental condition the various methods should be applied.

The parameters checked for each of these four scanning methods were dose, scan time, artefacts and signal-to-noise ratio.

Dose and Scan Time

In addition to image quality, factors like dose and total scan time are of importance when determine which scanning method should be applied. To give an indication of dose to a mouse from a CT scan, the CT image quality phantom (mouse size) was scanned. See Table 3.10 for acquisition parameters.

Scan time, exposure (mAs), the CT dose index ($CTDI_{vol}$) and the dose length product (DLP) were recorded. Neither of the results, except for scan time, were measured directly, they were all just recorded of the system screen.

Artefacts and Signal-to-Noise Ratio

The nanoScan Jaszczak phantom filled with CT contrast liquid was scanned to evaluate artefacts and signal-to-noise-ratio (SNR) in images acquired with different acquisition methods. The acquisition parameters are given in Table 3.11. The images were all reconstructed with the FDK algorithm using the RamLak filter. Iomeron (Bracco Imaging SpA, Milan, Italy) was used as contrast agent, with 350 mg I/ml. The contrast agent was diluted in water, with the ratio of Iomeron to water being approximately 1:64.

To compare the degree of artefacts present in the four images, the variation of noise was measured in a ROI placed as shown in Figure 3.10a. The ROI was placed in a seemingly homogeneous region with the assumption that the variability in signal intensity would increase in the presence of artefacts.

SNR was measured by dividing the mean signal intensity in a ROI by the standard deviation of the noise outside the ROI. For each of the four images, the SNR was measured six times. The ROIs used for measuring mean signal intensity were placed around six rods of different sizes, ROI 1-6 in Figure 3.10b, and the standard deviation of the noise outside these ROIs was measured from a ROI in the middle of the image, ROI 7 in Figure 3.10b.

Acquisition mode	All scanning methods
Number of projections	720
Tube Voltage	All kV_p
Tube current	All μA
Exposure time	300 ms
Magnification	Maximum Zoom

Table 3.10: CT acquisition parameters, dose and scan time measurement.

Acquisition mode	All scanning methods
Number of projections	720
Tube Voltage	70 kV_p
Tube current	310 μA
Exposure time	300 ms
Magnification	Maximum FOV

Table 3.11: CT acquisition parameters, evaluation of artefacts and signal-to-noise ratio.

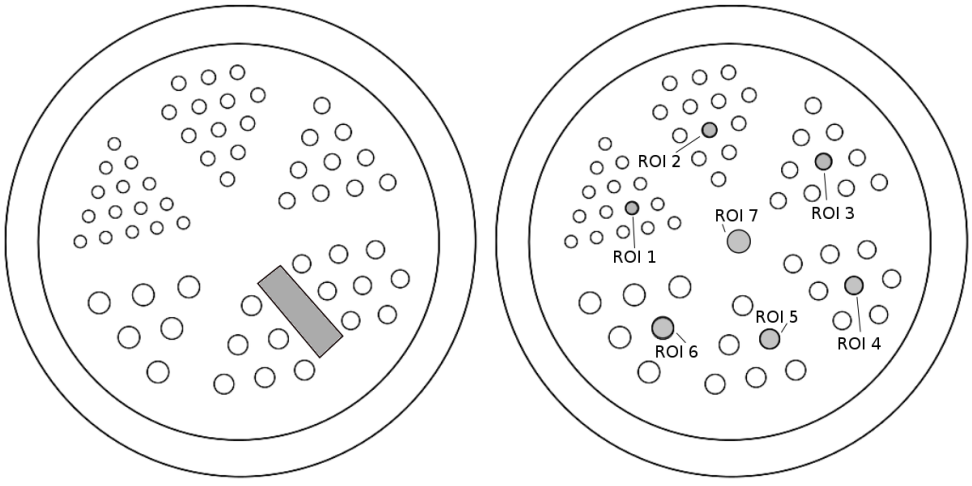

(a) (b)

Figure 3.10: Location of ROIs (gray), (a) for evaluation of artefacts and (b) for SNR measurements.

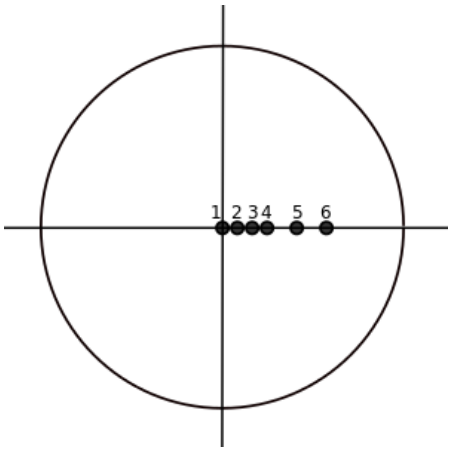

Figure 3.11: Positioning of the point source in the transaxial plane for measurements of spatial resolution. The points has the following radial distances from center: (1) 0 mm, (2) 5 mm, (3) 10 mm, (4) 15 mm, (5) 25 mm, and (6) 35 mm. Axial position in scanner: center of axial field of view (FOV) and 1/4 of axial FOV from center.

3.5 Evaluation of the PET Subsystem

3.5.1 Spatial Resolution

The spatial resolution of the system was measured as proposed in the NEMA NU 4-2008 standard. The measurements were performed by imaging the standard NEMA point source at 12 different positions in the scanner.

The point source was first scanned placed at the center of axial field of view (FOV), and then at one-fourth of the axial FOV from the center, at following radial distances from the center of transaxial FOV: 0 mm, 5 mm, 10 mm, 15 mm, 25 mm and 35 mm, as seen in Figure 3.11. The acquisition settings for the system are given in Table 3.12.

The acquired data were reconstructed, as proposed in the NEMA standard, with 2D filtered back-projection (FBP), resulting in a reconstructed image with 0.585 mm axial plane thickness and 0.100 mm pixel size. The reconstruction parameters are given in Table 3.13. FBP is not normally the reconstruction method of choice, due to suboptimal performance. Thus to get spatial resolution values also for the default reconstruction algorithm of the nanoScan PET system, the acquired data were also reconstructed with TeraTomo 3D reconstruction, see Table 3.14.

After reconstruction, the DICOM images were converted into a 3D array in Python. The tangential/radial slice and the tangential/axial slice with largest value, i.e. which had largest value when the pixels in the slices were summed together, were found. The tangential/radial slice was used to find tangential

Coincidence mode:	1-5
Count rate mode:	Normal mode
Coincidence Time Window:	5 ns
Acquisition Time:	10 minutes
List mode type:	Fine Timestamp

Table 3.12: PET acquisition parameters, spatial resolution measurements.

Reconstruction Mode:	2D
Energy window:	250-750 keV
Coincidence mode:	1-3 for 0 mm, 5 mm, 10 mm and 15 mm 1-5 for 25 mm and 35 mm
Reconstruction:	FBP
Rebinning method:	SSRB SINO
Ring difference:	8
Random Corrections:	Delayed Window
Normalization:	ON
Dead time Correction:	ON
Reconstruction resolution:	Voxel size: 0.1 mm $\times$ 0.1 mm $\times$ 0.585 mm

Table 3.13: PET reconstruction parameters, spatial resolution, filtered back-projection (FBP).

Reconstruction Mode:	3D
Energy window:	400-600 keV
Coincidence mode:	1-3
Reconstruction:	Tera-Tomo
Random Corrections:	Delayed Window
Normalization:	ON
Dead time Correction:	ON
Reconstruction resolution:	Voxel size: 0.1 mm $\times$ 0.1 mm $\times$ 0.1 mm

Table 3.14: PET reconstruction parameters, spatial resolution, Tera-Tomo.

and radial response functions and the tangential/axial slice were used to find axial response function. See Figure 3.12 for two of these slices. When these slices were found, the response functions were made by summing the one-dimensional profiles that were parallel to the direction of measurement. Figure 3.13 shows a typical response function.

The maximum value of the response function was found by parabolic fit of the peak point and its two nearest neighboring points. The full width at

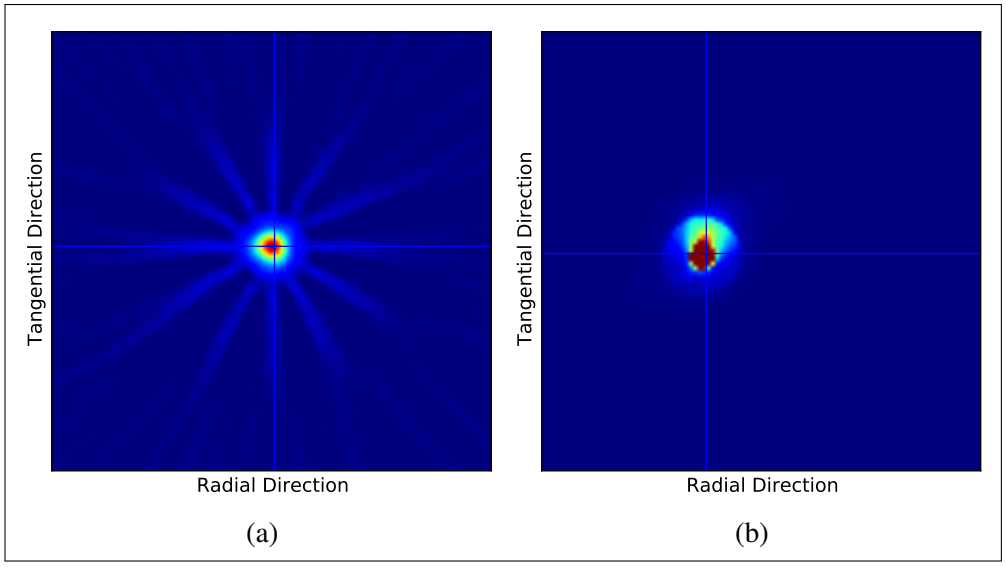

Figure 3.12: Image of ^{22}Na, reconstructed with (a) filtered back-projection (FBP) and (b) Tera-Tomo.

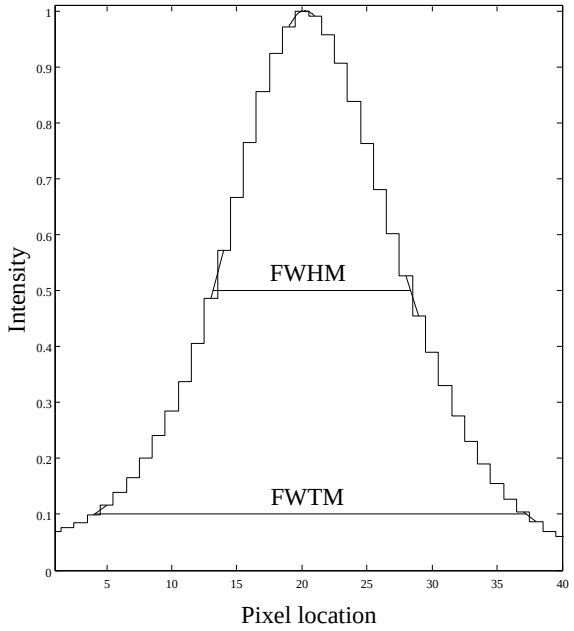

Figure 3.13: A typical response function with FWHM and FWTH determined by interpolation.

half maximum (FWHM) and full width at tenth maximum (FWTM) were determined by linear interpolation between adjacent pixels at half and one-tenth of the maximum value, see Figure 3.13.

The spatial resolution is, in all three orthogonal directions, here defined as

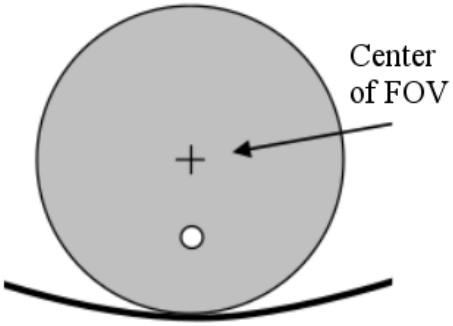

Figure 3.14: Positioning of the mouse-like phantom, counting rate capabilities. The white circle is where the line source is placed [4].

the FWHM and FWTM of the one-dimensional response functions through the peak of the image in the three directions.

3.5.2 Scatter Fraction, Count Losses, and Random Coincidence Measurements

This test evaluates the counting rate capabilities of the scanner, as proposed in the NEMA NU 4-2008 standard. This test was done using the mouse-like phantom described in Section 3.3, with a line source filled with FDG. The phantom was placed in the scanner, so that the line source inserted in the phantom was positioned nearest to the animal bed, see Figure 3.14.

At startup, the source had relatively high activity (65 MBq). Regular measurements were taken while the activity in the phantom decayed over several half-lifes (to 0.27 MBq). A background scan was also performed, where the mouse-like phantom was scanned, but without any radioactivity in it. Acquisition settings for the system are given in Table 3.15.

When reconstructing the data, no corrections for variation in detector sensitivity or detector motions, such as random and scattered events, dead-time, or attenuation, were applied to the measurements. The data were rebinned into a set of 2D sinograms during reconstruction, since the sinograms were needed for data analysis, not the final DICOM images. See Table 3.16 for reconstruction parameters. Single slice rebinning (SSRB) was used so that each slice were represented by one sinogram.

All pixels in each sinogram i of acquisition j located farther than 8 mm from the edges of the phantom were set to zero, as illustrated in Figure 3.15. In other words, only the data within a band 1.6 cm wider than the phantom and centered on the projection space were kept for the following analysis. This mask was also implemented on the background scan.

Coincidence mode:	1-5
Count rate mode:	Normal mode
Coincidence Time Window:	5 ns
Acquisition Time:	2 min (Scan 1-16), 5 min (Scan 17-24), 10 min (Scan 25 -30), 20 min (background)
List mode type:	Fine Timestamp

Table 3.15: PET acquisition parameters, counting rate capabilities.

Reconstruction Mode:	2D
Energy window:	250-750 keV
Coincidence mode:	1-5
Reconstruction:	FBP
Rebinning Method:	SSRB SINO
Ring Difference:	81
Random Corrections:	None
Normalization:	Off
Decay Correction:	Off
Dead time Correction:	Off

Table 3.16: PET reconstruction parameters, counting rate capabilities.

For each projection angle within the sinogram, i.e. for each sinogram row, the location of the center of the line source response was determined by finding the pixel with the greatest value. Then each projection were shifted, so that the pixel with the maximum value in each row became aligned with the central pixel of the sinogram, as illustrated in Figure 3.15.

After alignment, a sum projection was produced. Each pixel in the sum projection is the sum of the pixels in each angular projection having the same radial offset as the pixel in the sum projection. Figure 3.15 shows a sum projection as a function of pixel location.

The random and scattered event's counts, $C_{r+s,i,j}$, and the total event count, $C_{TOT,i,j}$, were found from the sum projection plot. This was done by first obtaining the counts (pixel intensities) $C_{L,i,j}$ and $C_{L,i,j}$ at the edges of a 14 mm wide strip at the center of the sinogram, see Figure 3.16. The pixel intensities were found by linear interpolation.

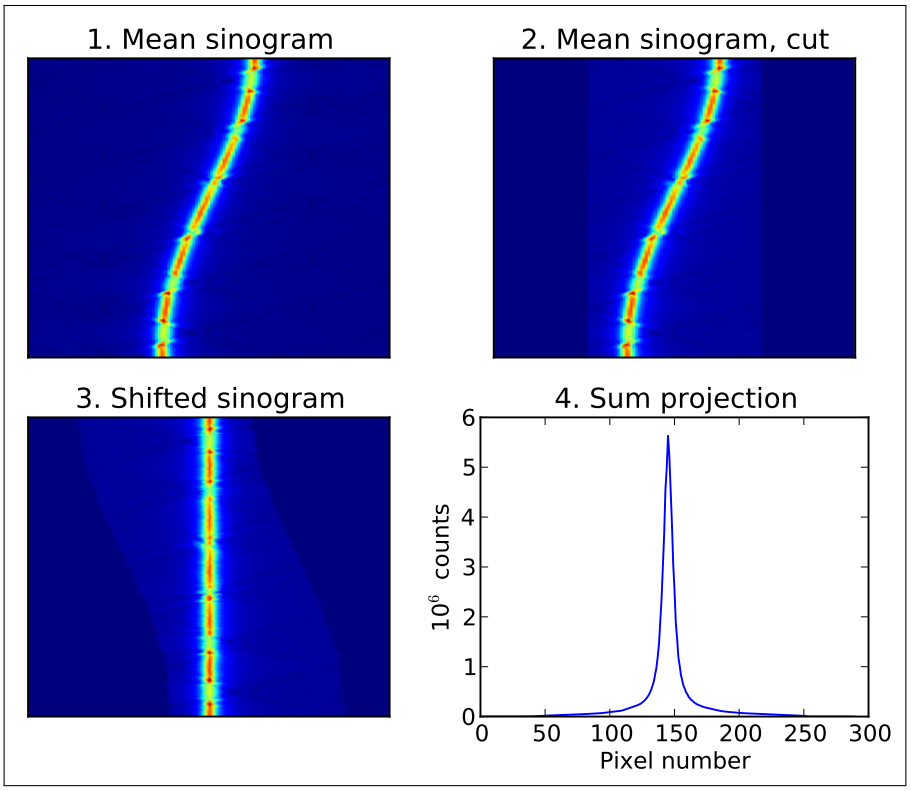

Figure 3.15: In 1), the mean sinogram of a line source is shown. In 2), a mask is applied to this sinogram. 3) is formed by aligning the pixels, and 4) is the sum projection as a function of pixel location.

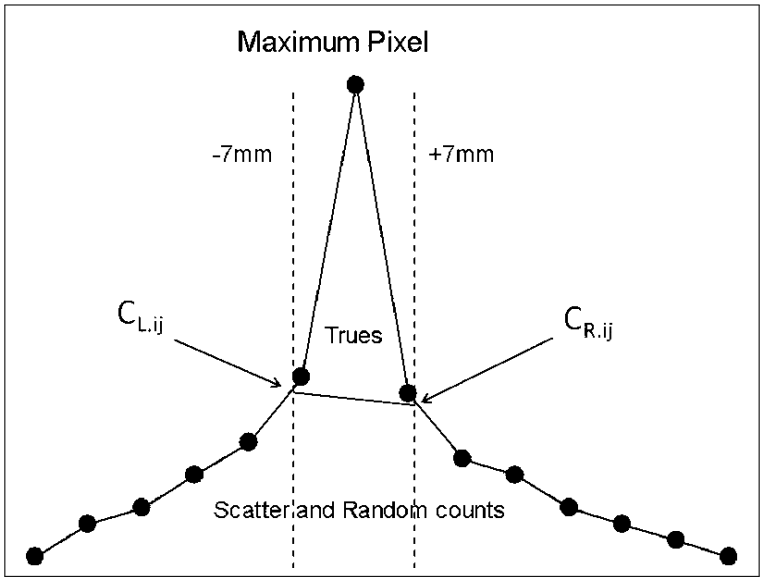

Figure 3.16: Sum projection, quantitative evaluation [4].

The number of random plus scattered event's counts, $C_{r+s,i,j}$, were then found for slice i of acquisition j, by first multiplying the average of $C_{L,i,j}$ and $C_{L,i,j}$ with the number of pixels, including fractional values, between the edges of the 14 mm strip, and then adding this to the counts in the pixels outside the strip. The total event count, $C_{TOT,i,j}$, is just the sum of all the pixels in the sum projection for slice i of acquisition j.

The average activity $A_{ave,j}$, of each acquisition j, was calculated as follows:

$$A_{ave,j} = \frac{A_{0,j}}{\ln 2}\left(\frac{t_{1/2}}{T_{acq,j}}\right)\left[1 - \exp\left(\frac{-T_{acq,j}}{t_{1/2}}\ln 2\right)\right], \tag{3.1}$$

where $A_{0,j}$ is the activity at the start of acquisition j, $T_{acq,j}$ is the acquistion time of acquisition j, and $t_{1/2}$ is the radiotracer's half-life, i.e. 109.74 minutes for ^{18}F.

$C_{r+s,i,j}$, $C_{TOT,i,j}$, $A_{ave,j}$ and $T_{acq,j}$ were all used to calculate the scatter fraction, total event rate, true event rate, random event rate, scattered event rate and noise equivalent count rate for each acquisition j.

Scatter Fraction

The scatter fraction was calculated at activities between 1 and 1.5 MBq, where the random event rate is expected to be negligible compared to the scatter event rate. The scatter fraction, SF_i, for each slice i was calculated as follows:

$$SF_i = \frac{\sum_{j'} C_{r+s,i,j'}}{\sum_{j'} C_{TOT,i,j'}}, \tag{3.2}$$

where j' is the acquisitions where the average activity was between 1 and 1.5 MBq.

The system scatter fraction, SF, was computed as the weighted average of SF_i as follows:

$$SF = \frac{\sum_{i}\sum_{j'} C_{r+s,i,j'}}{\sum_{i}\sum_{j'} C_{TOT,i,j'}}. \tag{3.3}$$

Total Event Rate Measurement

The total event rate, $R_{TOT,i,j}$, for each slice i of acquisition j was computed as:

$$R_{TOT,i,j} = \frac{C_{TOT,i,j}}{T_{acq,j}}. \tag{3.4}$$

The system total event rate, $R_{TOT,j}$, was computed as the sum of $R_{TOT,i,j}$ over all slices i.

True Event Rate Measurement

For each acquisition j, the true event rate, $R_{t,i,j}$, for each slice i was computed as:

$$R_{t,i,j} = \frac{C_{TOT,i,j} - C_{r+s,i,j}}{T_{acq,j}}. \tag{3.5}$$

The system true event rate, $R_{t,j}$, was computed as the sum of $R_{t,i,j}$ over all slices i.

Random Event rate Measurement

The random event rate, $R_{r,i,j}$, for each slice i of acquisition j was computed as:

$$R_{r,i,j} = R_{TOT,i,j} - \left(\frac{R_{t,i,j}}{1 - SF_i} \right). \tag{3.6}$$

The system random event rate, $R_{r,j}$, was computed as the sum of $R_{r,i,j}$ over all slices i.

Scattered Event Rate Measurement

The scattered event rate, $R_{s,i,j}$, for each slice i of acquisition j was computed as:

$$R_{s,i,j} = R_{TOT,i,j} - R_{t,i,j} - R_{r,i,j} - R_{int,j}, \tag{3.7}$$

where $R_{int,j}$ is intrinsic true count rate. $R_{int,j}$ was calculated by taking the total number of true coincidence events per plane in the background sinogram and dividing this by scan duration in seconds.

The system random event rate, $R_{s,j}$, was computed as the sum of $R_{s,i,j}$ over all slices i.

Noise Equivalent Count Rate Measurement

The noise equivalent count rate, $R_{NEC,i,j}$, for each slice i of acquisition j was computed as:

$$R_{NEC,i,j} = \frac{R_{t,i,j}^2}{R_{TOT,i,j}}. \tag{3.8}$$

The system noise equivalent count rate, $R_{NEC,j}$, was computed as the sum of $R_{NEC,i,j}$ over all slices i.

3.5.3 Sensitivity

This test was done by scanning the standard NEMA point source at 64 different positions in the scanner. The activity of the point source at start of each acquisition was calculated using the decay law given in Equation (2.2). The initial activity value with time of measurement was given.

In the NEMA NU 4-2008 standard the ^{22}Na point source is supposed to be scanned in steps throughout the whole axial FOV, in steps of the size of a reconstructed slice. Since the axial FOV is 9.4 cm long and each slice is 0.585 mm thick, this gives 161 steps. Taking into consideration the high resolution and long axial FOV of the scanner, this test was instead performed with steps of size 0.585 mm only around the center of FOV and near the edges of the FOV. In between this, the step size was increased to 2.340 mm. In practice, steps of sizes respectively 0.6 mm and 2.3 mm were achieved.

The acquisition settings are given in Table 3.17. A background scan was also performed without source, to get a representative background rate which is needed to ensure that a reasonable estimate of the sensitivity is determined. The background scan had the same acquisition settings and reconstruction settings as the point source scans. The data were rebinned into a set of 2D sinograms during reconstruction, making 161 sinograms, each corresponding to one slice. See Table 3.18 for reconstruction parameters.

For each scan, the sinogram with the highest values was chosen, since this sinogram corresponds to the slice where the point source was located. A mask was applied to this sinogram, by taking the highest value in each row in this sinogram and setting all pixels greater than 1 cm from this peak value to zero, as illustrated in Figure 3.17. The total number of pixels in the masked sinogram were then summed to form the total counts in that slice. The same mask was applied to all the sinograms corresponding to that scan, and the total counts in each scan were found by summing the counts in each masked sinogram. This was also done with the background acquisition, as seen Figure 3.17.

For each scan i the counting rate R_i was determined by dividing the total counts in that scan, i.e. in all 161 sinograms, by the acquisition time. The background counting rate, $R_{B,i}$, was determined by dividing the counts in the background sinograms by the background acquisition time.

The sensitivity (counts per second per Bq) for each scan i was then calculated as follows:

$$S_i = \left(\frac{R_i - R_{B,i}}{A_{calc}} \right). \tag{3.9}$$

The branching ratio of ^{22}Na for β^+-decay is 0.9060, so the absolute sensitivity (percentage) is given by:

Coincidence mode:	1-5
Count rate mode:	Normal mode
Coincidence Time Window:	5 ns
Acquisition Time:	1 min
List mode type:	Fine Timestamp

Table 3.17: PET acquisition parameters, sensitivity measurement.

Reconstruction Mode:	2D
Energy window:	250-750 keV
Coincidence mode:	1-5
Reconstruction:	FBP
Rebinning Method:	SSRB SINO
Ring Difference:	81
Random Correction:	Delayed Window
Normalization:	On
Decay Correction:	On
Dead Time Correction:	On

Table 3.18: PET reconstruction parameters, sensitivity measurement.

$$S_{A,i} = \frac{S_i}{0.9060} \times 100. \tag{3.10}$$

The branching ratio of a given decay mode is the fraction of particles which disintegrate with this decay mode, with respect to the total number of particles which decay.

The total system sensitivities were calculated as follows:

$$S_{tot} = \frac{1}{N} \sum_i S_i, \tag{3.11}$$

$$S_{A,tot} = \frac{1}{N} \sum_i S_{A,i}, \tag{3.12}$$

where N is the total number of slices used. The system sensitivities appropriate for mouse applications were computed by taking the average sensitivity of the central 7 cm.

Since the data were not acquired at steps of 0.585 mm, the total sensitivity was calculated by interpolating the sensitivity profile for 0.585 mm steps in the whole FOV.

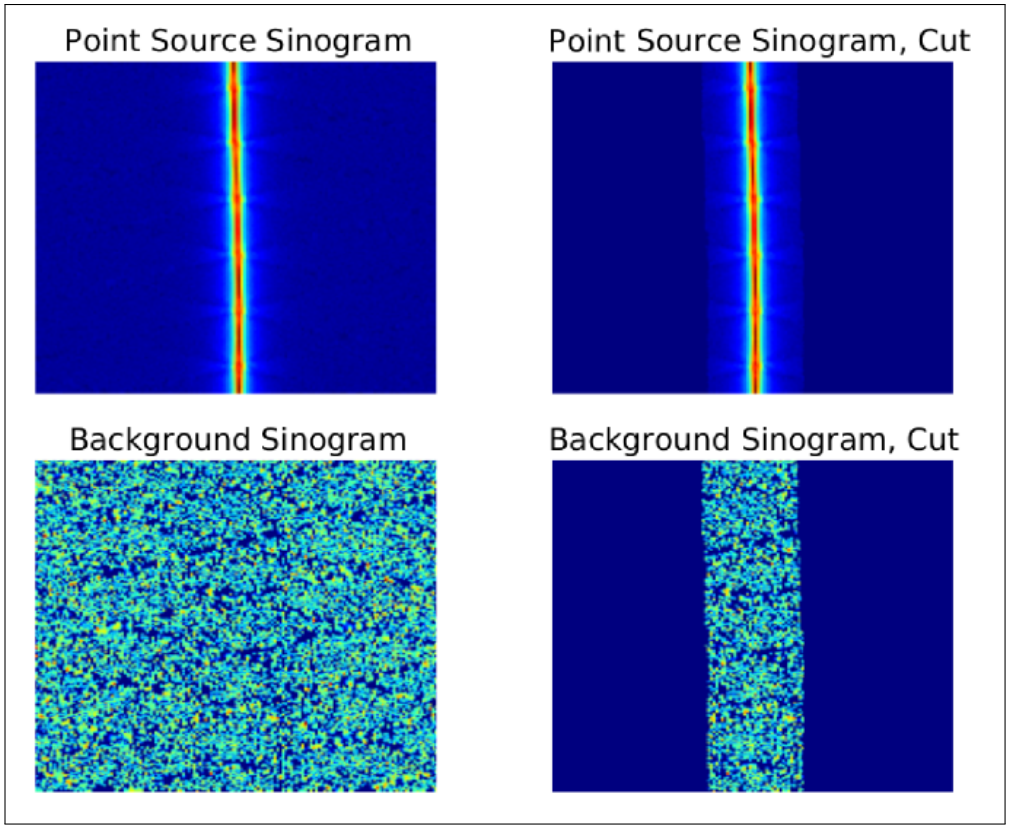

Figure 3.17: Sinogram, sensitivity measurements. Original sinogram and cut sinogram, i.e. original sinogram with mask applied.

3.5.4 NEMA Image Quality Phantom Study

This test uses the NEMA image quality phantom, described in Section 3.3. This phantom can be divided into three parts; a uniform region, a 5-rod region and a 2-chamber region, as seen in Figure 3.18.

The phantom was filled with FDG, and the activity injected into the phantom was 3.7 MBq $\pm$ 5% at scan start. The phantom was placed in the scanner such that the axis of its main cylindrical compartment was aligned with the axis of the tomograph's field of view. The phantom was scanned for 20 minutes, with acquisition settings as given in Table 3.19. The acquired data were reconstructed with Tera-Tomo, to get a reconstructed image with voxel size 0.4 mm $\times$ 0.4 mm $\times$ 0.4 mm. The reconstruction parameters are given in Table 3.20.

Uniformity

Uniformity was measured by drawing a cylindrical volume of interest (VOI) with 22.5 mm diameter and 10 mm length, over the center of the uniform

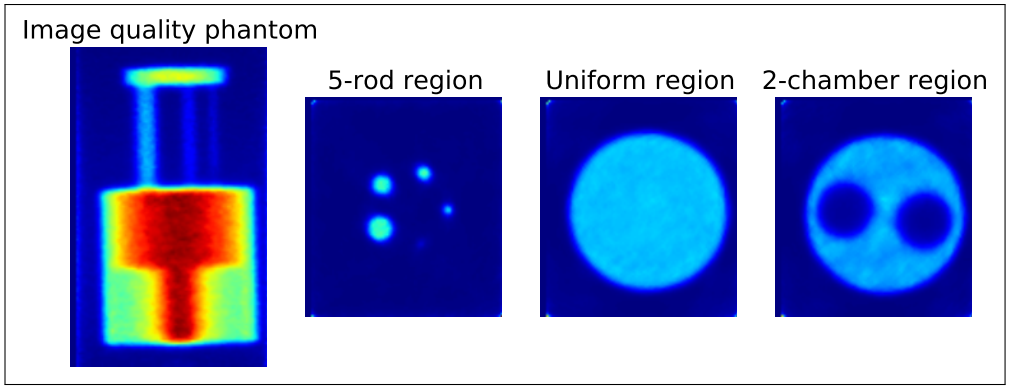

Figure 3.18: Top scan of NEMA image quality phantom, and a slice from each of the three phantom parts.

region of the image quality phantom. The average, minimum and maximum activity concentration and the percentage standard deviation (%STD) in this VOI were measured. The %STD is the standard deviation divided by the mean value and then multiplied by 100.

Recovery Coefficients

The 5-rod region was used to find the recovery coefficients. The image slices covering the central 10 mm length of the rods were averaged to obtain a single image slice of lower noise. Circular regions of interest (ROIs) were drawn around each of the rods, with a diameter twice the physical diameter of the rods. The pixel coordinates of the maximum value in each of the ROIs were measured, and used to create line profiles along the rods in the axial direction. The recovery coefficients were then found by summing the pixel values along each profile and dividing the sum by the mean activity concentration found in the uniformity test. The %STD of the recovery coefficients was calculated as follows:

$$\%\text{STD}_{RC} = 100 \cdot \sqrt{\left(\frac{\text{STD}_{lineprofile}}{\text{Mean}_{lineprofile}}\right)^2 \left(\frac{\text{STD}_{background}}{\text{Mean}_{background}}\right)^2} \tag{3.13}$$

Accuracy of Corrections

The 2-chamber region was used to evaluate the accuracy of scatter corrections, by finding the spill-over ratio (SOR). A cylindrical VOI with diameter of 4 mm and length of 7.5 mm was defined in center of each of the water- and air-filled cylindrical chambers. The SOR is the mean activity concentration in each of these VOIs, divided by the mean activity concentration in the uniform region. The %STD was calculated according to Equation (3.13).

Coincidence mode:	1-5
Count rate mode:	Normal mode
Coincidence Time Window:	5 ns
Acquisition Time:	20 minutes
List mode type:	Fine Timestamp

Table 3.19: PET acquisition parameters, image quality phantom study.

Energy window:	400-600 keV
Coincidence mode:	1-5
Reconstruction:	Tera-Tomo
Random Corrections:	Delayed Window
Normalization:	ON
Dead time Correction:	ON
Attenuation Correction:	ON
Reconstruction resolution:	Voxel size: 0.4 mm $\times$ 0.4 mm $\times$ 0.4 mm

Table 3.20: PET reconstruction parameters, image quality phantom study.

Chapter 4

Results

In this chapter, the results of the performance evaluation of the PET/CT system described in the previous chapter are presented.

4.1 CT Subsystem

4.1.1 Hounsfield Quality Check

Image Noise Measurement

Table 4.1 summarizes the results from the image noise measurement, and Table 4.2 is the output from the automatic image noise measurement, i.e. the vendor provided Hounsfield quality control software.

By definition, the CT-numbers of water and air are 0 HU and -1000 HU, respectively. The vendor has set a tolerance of $\pm$ 30 HU for CT-numbers. In the water regions, the results are mostly in good accordance with the expected value; the mean CT-numbers are all within 0 ± 30 HU. The standard deviation in the water region is quite high, it approaches 400. In the air region, the mean CT-numbers are not within the $\pm$ 30 HU tolerance. Here, the CT-numbers are as high as -875 HU. The standard deviation in air is much lower than in water, it goes only up to 175.

It is important to notice that none of the CT-numbers are lower than -1000 HU. The DICOM images were checked in Python to see if any pixels at all had values lower than -1000 HU, which they did not have. This indicates that the reconstruction algorithm truncates low values to -1000 before exporting to DICOM. This will have an impact on the mean CT-number and on the standard deviation in a region of interest (ROI) in the CT image, especially in an area with low CT-numbers.

Settings	Exposure time	Air				Water			
		Mean HU	Min HU	Max HU	Std. Dev.	Mean HU	Min HU	Max HU	Std. Dev.
35 kV_p, 1000 μA	170 ms	-888.4	-1000	206	151.3	-11.8	-1000	2042	399.9
	300 ms	-927.2	-1000	-328	93.4	-16.9	-1000	1170	259.5
	450 ms	-934.6	-1000	-396	81.5	-18.7	-1000	1126	217.0
50 kV_p, 670 μA	170 ms	-912.2	-1000	-40	118.5	-15.4	-1000	1575	332.1
	300 ms	-920.0	-1000	-215	101.7	-10.7	-981	1000	221.8
70 kV_p, 310 μA	170 ms	-874.6	-1000	354	175.2	-17.1	-1000	1664	383.4
	300 ms	-903.6	-1000	-132	125.9	-14.0	-1000	1115	271.0

Table 4.1: Image noise measurement, non-automatic test; mean CT-numbers (HU) and standard deviation (Std. Dev.).

Settings	Exposure time	Air		Water	
		Mean HU	Std. Dev.	Mean HU	Std. Dev.
35 kV_p, 1000 μA	170 ms	-1004.2	33.3	-5.6	62.4
	300 ms	-1006.6	26.0	-6.6	48.0
	450 ms	-1004.2	21.8	-8.7	42.1
50 kV_p, 670 μA	170 ms	-1004.3	34.3	-1.9	56.4
	300 ms	-1002.1	27.2	6.4	46.0
70 kV_p, 310 μA	170 ms	-1002.4	44.5	-2.6	66.5
	300 ms	-1001.8	34.2	2.8	51.6

Table 4.2: Image noise measurement, automatic test; mean CT-numbers (HU) and standard deviation (Std. Dev.).

In the automatic test, however, the CT-numbers are not cut at -1000 HU, and here the mean CT-numbers are all within the tolerance both for water and air. The mean CT-numbers are within 0 ± 9 HU for water and -1000 ± 7 HU for air. The standard deviation is also much lower in the automatic test than in the non-automatic test.

Image Homogeneity Measurement

The results of the image homogeneity measurement are given in Table 4.3 and Table 4.4. Table 4.5 and Table 4.6 are the output of the automatic image homogeneity measurement test.

When performing a simple statistical analysis (Student t-test, two-tailed paired, $p < 0.001$) it was seen that the center ROI values for water were not significantly different from the values obtained in the adjacent ROIs (12h, 3h, 6h, 9h), both for the non-automatic and automatic test. The simple statistical analysis was not performed on air data, because of the pixel cut at -1000.

The automatic test has CT-numbers which are much closer to the defined CT-numbers of water and air when compared to the non-automatic test. The automatic test has also much lower standard deviations.

Settings	Exposure time	ROI center		ROI 12h		ROI 3h		ROI 6h		ROI 9h	
		HU	Std. Dev.	HU	Std. Dev.	HU	Std. Dev.	HU	Std. Dev.	HU	Std. Dev.
35 kV_p, 1000 μA	170 ms	-891.9	148.6	-900.8	135.3	-887.0	147.9	-901.4	140.3	-875.0	157.2
	300 ms	-911.1	103.6	-940.1	82.3	-912.8	98.4	-939.5	85.3	-926.6	93.1
	450 ms	-919.5	90.1	-951.2	66.4	-916.4	86.4	-946.2	72.7	-936.5	79.5
50 kV_p, 670 μA	170 ms	-902.2	126.7	-921.2	109.4	-889.2	129.7	-919.2	112.9	-924.9	108.6
	300 ms	-902.1	113.7	-937.9	85.5	-904.6	106.1	-932.7	93.5	-920.7	98.1
70 kV_p, 310 μA	170 ms	-849.8	194.9	-900.1	150.7	-881.6	166.9	-884.4	169.1	-866.3	178.3
	300 ms	-883.8	140.4	-920.4	110.5	-887.7	132.2	-916.3	117.8	-902.5	124.7

Table 4.3: Image homogeneity measurement, non-automatic test. Mean CT-numbers (HU) and standard deviation (Std. Dev.) in ROIs in air compartment.

Settings	Exposure time	ROI center		ROI 12h		ROI 3h		ROI 6h		ROI 9h	
		HU	Std. Dev.	HU	Std. Dev.	HU	Std. Dev.	HU	Std. Dev.	HU	Std. Dev.
35 kV_p, 1000 μA	170 ms	-28.5	414.6	-56.0	417.5	-4.2	396.6	-35.3	399.1	-55.2	398.1
	300 ms	-41.9	270.2	-41.1	265.7	-32.5	262.2	-27.2	260.1	-38.0	256.9
	450 ms	-49.0	215.2	-44.7	209.6	-41.0	206.0	-31.6	211.4	-26.7	226.4
50 kV_p, 670 μA	170 ms	-46.6	349.3	-33.8	344.6	-14.2	337.3	-10.6	332.6	-39.8	329.3
	300 ms	-42.7	231.5	-39.6	221.0	-28.7	225.4	-21.3	222.0	-38.0	218.3
70 kV_p, 310 μA	170 ms	-36.3	396.9	-47.9	391.2	-29.7	385.2	-11.8	379.7	-38.5	376.8
	300 ms	-45.2	274.7	-46.2	261.1	-30.1	271.8	-22.8	282.4	-45.4	266.8

Table 4.4: Image homogeneity measurement, non-automatic test. Mean CT-numbers (HU) and standard deviation (Std. Dev.) in ROIs in water compartment.

Settings	Exposure time	ROI center		ROI 12h		ROI 3h		ROI 6h		ROI 9h	
		HU	Std. Dev.	HU	Std. Dev.	HU	Std. Dev.	HU	Std. Dev.	HU	Std. Dev.
35 kV_p, 1000 μA	170 ms	-1000.4	32.3	-1002.4	26.1	-997.1	30.5	-1002.2	43.6	-997.9	30.5
	300 ms	-1001.3	24.3	-1003.2	19.4	-997.3	22.9	-999.6	32.8	-997.8	22.9
	450 ms	-1001.1	20.1	-1002.8	16.3	-996.2	19.4	-996.3	27.9	-997.7	19.1
50 kV_p, 670 μA	170 ms	-1000.6	33.3	-1002.5	26.7	-996.4	31.5	-1000.9	45.1	-999.8	31.0
	300 ms	-1000.3	26.2	-1003.9	20.9	-996.9	24.7	-998.1	35.9	-996.1	24.4
70 kV_p, 310 μA	170 ms	-1004.8	43.8	-1005.1	35.8	-1000.3	40.4	-1002.4	60.3	-997.2	40.9
	300 ms	-999.5	33.2	-1003.1	26.9	-994.6	31.6	-998.4	44.7	-995.8	31.4

Table 4.5: Image Homogeneity measurement, automatic test. Mean CT-numbers (HU) and standard deviation (Std. Dev.) in ROIs in air compartment.

Settings	Exposure time	ROI center		ROI 12h		ROI 3h		ROI 6h		ROI 9h	
		HU	Std. Dev.	HU	Std. Dev.	HU	Std. Dev.	HU	Std. Dev.	HU	Std. Dev.
35 kV_p, 1000 μA	170 ms	-37.4	61.8	2.6	50.5	-3.1	58.7	-26	73.7	3.1	58.3
	300 ms	-34.3	46.6	1.3	38.8	-3.8	44.5	-24.7	55.2	-0.2	44.5
	450 ms	-39.0	36.9	3.0	34.3	-5.7	37.5	-29.7	44.1	-4.7	37.8
50 kV_p, 670 μA	170 ms	-18.6	58.5	1.4	45.3	1.6	53.3	-13.7	70.7	0.0	52.4
	300 ms	-24.5	39.9	15.8	37.8	6.6	40.9	-15.6	48.8	12.0	41.3
70 kV_p, 310 μA	170 ms	-22.8	68.2	0.5	53.9	-1.9	62.2	-13.9	85.2	3.2	62.2
	300 ms	-29.2	46.0	11.9	42.2	4.1	46.9	-19.4	57.2	8.9	47.5

Table 4.6: Image homogeneity measurement, automatic test. Mean CT-numbers (HU) and standard deviation (Std. Dev.) in ROIs in water compartment.

4.1.2 Noise in Reconstruction Filters

The mean CT-number and standard deviation in ROIs in the CT image quality phantom are given in Table 4.7. The filters, sorted from highest to lowest standard deviation according to Table 4.7, are as follows: RamLak, Butterworth, Shepp-Logan, Cosine, Hamming, Hann and BlackMan.

The difference in mean CT-number and standard deviation of the different filters are small; the CT-numbers in the air region are all within $\pm$ 2% of the mean CT-number of the filters, and the CT-numbers in the water are all within $\pm$ 7% of the mean CT-number of the filters. To check if there were any obvious visual differences in images of non-homogeneous objects when reconstructing using different filters, the nanoScan Jaszczak phantom was used. One data set was acquired with "semicircular, half scan", and the images were reconstructed using the FDK algorithm and different filters, Figure 4.1. As seen in Figure 4.1, there are not much difference between the filters.

	Air		**Water**	
	Mean HU	**Std. Dev.**	**Mean HU**	**Std. Dev.**
RamLak	-899.8	128.4	-46.2	268.3
Hamming	-921.2	102.0	-49.7	205.2
Hann	-922.3	100.3	-49.7	201.3
Shepp-Logan	-909.2	119.7	-49.8	248.4
Butterworth	-906.6	123.6	-49.6	257.8
Cosine	-916.0	109.8	-49.6	223.7
BlackMan	-928.1	91.7	-49.7	181.1

Table 4.7: Reconstruction filters; mean CT-number (HU) and standard deviation (Std. Dev.).

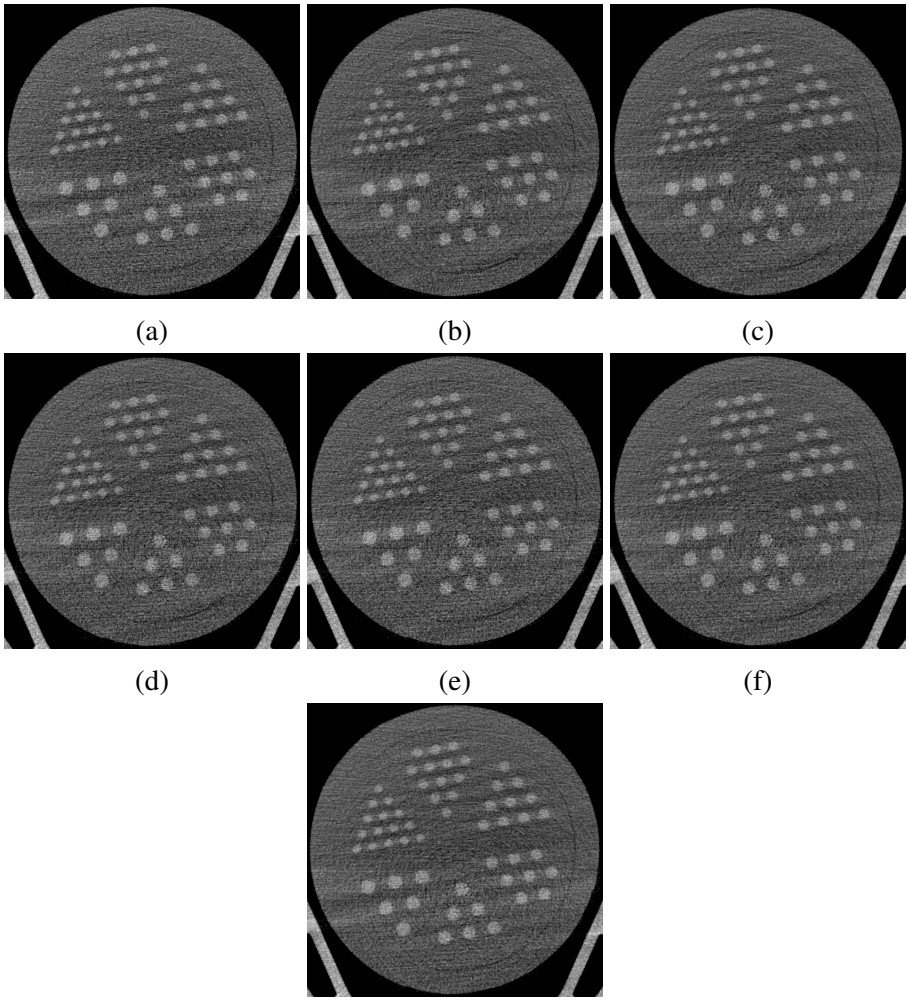

(a) (b) (c)

(d) (e) (f)

(g)

Figure 4.1: Image of phantom with contrast agent, reconstructed with the FDK algorithm using the following filters: (a) RamLak, (b) Hamming, (c) Hann, (d) Shepp-Logan, (e) Butterworth, (f) Cosine and (g) BlackMan.

4.1.3 Different Scanning Methods

Dose and Scan Time

The scan time and the dose length product (DLP) for the different scanning methods when imaging the CT image quality phantom (mouse size) are given in Table 4.8. DLP is not equivalent to dose, but can be used to determine the total amount of radiation given to the scanned object, and can thus be used to compare the dose from different scanning methods.

"Semicircular, half scan" has the shortest scan time, and "helical, 0.5" pitch the longest. "Semicircular, full scan" and "helical, 1 pitch" have more or less the same scan time.

The dose is highest for "helical, 0.5 pitch", and lowest for "helical, 1 pitch". The dose is the same for "semicircular, half scan" and "semicircular, full scan". "Helical, 0.5 pitch" has twice as much dose as "helical, 1 pitch".

For each tube voltage, the current was set automatically. The mAs, i.e. the product of the tube current and exposure time, is lowest for 70 kV_p and highest for 35 kV_p. The dose, however, is lowest for 35 kV_p, a factor 2 lower than for 50 kV_p and 70 kV_p, which have comparable dose.

Semicircular, Full scan					
Set kV_p and μA	**Actual kV_p and μA**	**Scan time (min:sec)**	**Exposure (mAs)**	**CTDIvol (cGy)**	**DLP (cGy × mm)**
35 kV_p, 1000 μA	34.72 kV_p, 992 μA	11:37	214272	20701.4	290250.0
50 kV_p, 670 μA	49.8 kV_p, 664.5 μA	11:30	143532	43135.9	604800.0
70 kV_p, 310 μA	69.98 kV_p, 305.25 μA	11:35	65934	42269.3	592650.0

Semicircular, Half scan					
Set kV_p and μA	**Actual kV_p and μA**	**Scan time (min:sec)**	**Exposure (mAs)**	**CTDIvol (cGy)**	**DLP (cGy × mm)**
35 kV_p, 1000 μA	34.7 kV_p, 991.5 μA	07:08	214164	20701.4	290250.1
50 kV_p, 670 μA	49.72 kV_p, 664.5 μA	07:08	143532	43135.9	604800.0
70 kV_p, 310 μA	69.86 kV_p, 304.5 μA	07:08	65772	42269.3	592650.0

Helical, 0.5 pitch					
Set kV_p and μA	**Actual kV_p and μA**	**Scan time (min:sec)**	**Exposure (mAs)**	**CTDIvol (cGy)**	**DLP (cGy × mm)**
35 kV_p, 1000 μA	34.78 kV_p, 992.5 μA	18:35	214380	6210.4	376351.2
50 kV_p, 670 μA	49.78 kV_p, 665 μA	18:33	143640	12940.8	784210.8
70 kV_p, 310 μA	69.9 kV_p, 304.5 μA	18:33	65772	12680.8	768456.6

Helical, 1 pitch					
Set kV_p and μA	**Actual kV_p and μA**	**Scan time (min:sec)**	**Exposure (mAs)**	**CTDIvol (cGy)**	**DLP (cGy × mm)**
35 kV_p, 1000 μ	34.86 kV_p, 993.5 μA	11:26	214596	3105.2	188175.6
50 kV_p, 670 μA	49.88 kV_p, 664.75 μA	11:20	143586	6470.4	392105.4
70 kV_p, 310 μA	69.92 kV_p, 304.75 μA	11:20	65826	6340.4	384228.3

Table 4.8: Scan time and dose index, various scanning methods and tube voltages.

Artefacts

The mean CT-number and standard deviation in ROIs in the nanoScan Jaszczak phantom are given in Table 4.9. As seen here, “semicircular, half scan” has highest standard deviation, and “helical, 0.5 pitch”, the lowest. Also, it is seen in Figure 4.2 that there are most artefacts present in the images obtained using “semicircular, half scan”, and least in “helical, 0.5 pitch”. “Helical, 1 pitch” and “semicircular, full scan” have comparable noise and level of visible artefacts.

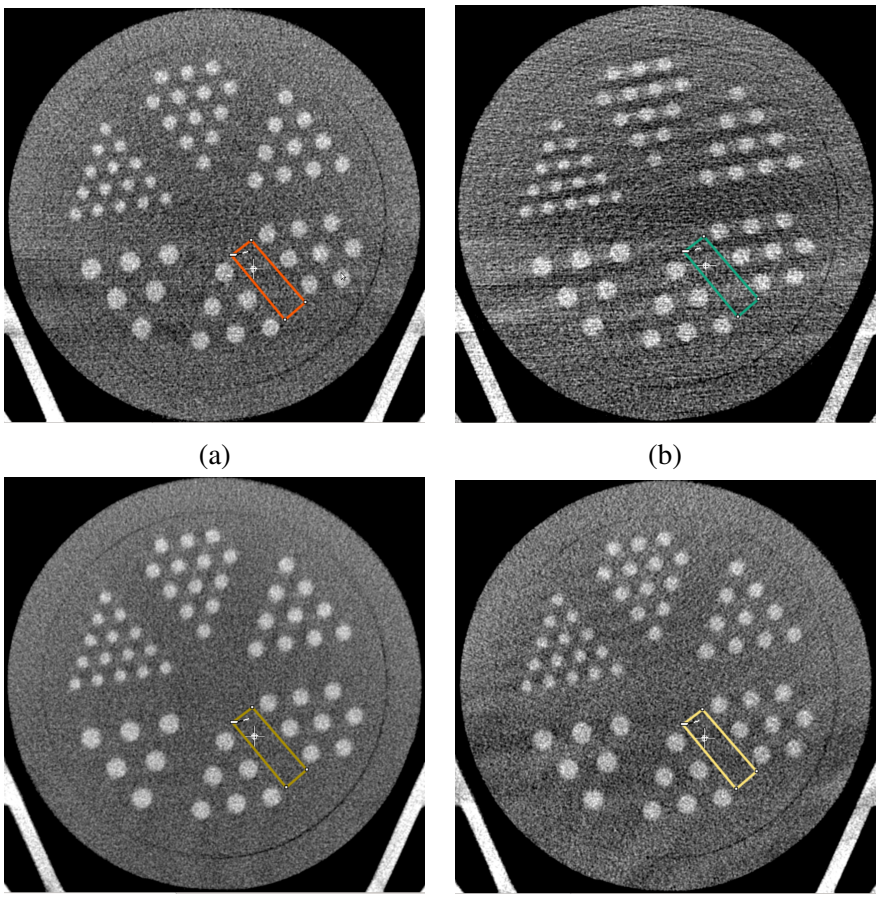

(a) (b)

(c) (d)

Figure 4.2: CT images acquired with tube voltage of 70 kV_p and with following acquisition methods: (a) “semicircular, full scan”, (b) “semicircular, half scan”, (c) “helical, 0.5 pitch” and (d) “helical, 1 pitch”.

	Mean HU	**Std. Dev.**
Semicircular, full scan	-67	194.1
Semicircular, half scan	-43	247.7
Helical, 0.5 pitch	-65	123.1
Helical, 1 pitch	-79	176.9

Table 4.9: Mean CT-number and standard deviation (Std. Dev.) in artefact ROIs.

Signal-to-Noise Ratio

The signal-to-noise ratios (SNRs) are given in Table 4.11, calculated from data in Table 4.10. Higher SNR means larger signal and less noise, so the higher, the better. "Helical, 0.5 pitch" has the highest SNRs, and "semicircular, half scan" the lowest. "Helical, 1 pitch" and "semicircular, full scan" has almost the same SNRs, which are comparable to the SNR values obtained using "semicircular, half scan".

	Helical, 0.5 pitch		
	Mean HU	**Std. Dev.**	**Volume (mm^3)**
ROI 1	170.7	146.4	0.023
ROI 2	204.0	119.3	0.029
ROI 3	224.7	132.8	0.042
ROI 4	211.8	133.4	0.053
ROI 5	201.7	137.7	0.056
ROI 6	194.6	145.0	0.066
ROI 7	-64.7	118.8	0.079

	Semicircular, full scan		
	Mean HU	**Std. Dev.**	**Volume (mm^3)**
ROI 1	216.6	189.4	0.023
ROI 2	250.4	178.3	0.029
ROI 3	243.9	184.8	0.042
ROI 4	226.0	192.8	0.053
ROI 5	215.6	205.2	0.056
ROI 6	192.5	209.0	0.066
ROI 7	-80.9	191.2	0.079

	Helical, 1 pitch		
	Mean HU	**Std. Dev.**	**Volume (mm^3)**
ROI 1	182.4	172.1	0.023
ROI 2	214.5	168.6	0.029
ROI 3	206.4	162.8	0.042
ROI 4	176.4	172.6	0.053
ROI 5	173.9	181.7	0.056
ROI 6	184.4	197.1	0.066
ROI 7	-55.1	176.6	0.079

	Semicircular, half scan		
	Mean HU	**Std. Dev.**	**Volume (mm^3)**
ROI 1	204.1	245.98	0.023
ROI 2	224.1	235.05	0.029
ROI 3	195.6	256.83	0.042
ROI 4	238.6	263.86	0.053
ROI 5	223.6	266.64	0.056
ROI 6	228.7	250.92	0.066
ROI 7	-112.8	235.05	0.079

Table 4.10: Data for SNR measurements; mean CT-number (HU) and standard deviation (Std. Dev.) in each ROI.

Rod diameter (mm)	**Helical, 0.5 pitch SNR**	**Helical, 1 pitch SNR**	**Semicircular, full scan SNR**	**Semicircular, half scan SNR**
0.7 mm	1.4	1.0	1.1	0.9
0.8 mm	1.7	1.2	1.3	1.0
0.9 mm	1.9	1.2	1.3	0.8
1.0 mm	1.8	1.0	1.2	1.0
1.1 mm	1.7	1.0	1.1	1.0
1.2 mm	1.6	1.0	1.0	1.0
Mean	1.7	1.1	1.2	1.0

Table 4.11: Signal-to-noise ratios (SNRs) in images acquired with different scanning methods.

4.2 PET Subsystem

4.2.1 Spatial Resolution

The resolution values found when reconstructing with filtered back-projection are shown in Figure 4.3 with the corresponding data in Table 4.12.

The full width at half maximum (FWHM) values approach 1 mm at the center of field of view (FOV), except in the axial direction at center of axial FOV, where the value is actually less than 1 mm. The FWHM values stay under 2 mm for the central 15 mm of the transaxial FOV.

The full width at tenth maximum (FWTM) values are around 3 mm at the center of FOV, and for the radial and axial direction the values are approximately 4 mm at 35 mm radial distance from the center of FOV. The tangential FWTM values increase more rapidly than the radial and axial values. This might be because of noise in the images; this will be discussed more in Chapter 5.

The resolution values found when reconstructing with Tera-Tomo, are given in Figure 4.4 and in Table 4.13. These resolution values are superior to those achieved when reconstructing with FBP. At center of FOV the FWHM values go down to approximately 0.6 mm, and are all less than 1 mm for the central 15 mm of the transaxial FOV. All resolution values, both FWHM and FWTM, are less than 2 mm for the dataset.

Reconstructed image pixel size (mm): 0.1000
Slice thickness (mm): 0.5850

	0 mm ± 0.5 mm		5 mm ± 0.5 mm		10 mm ± 0.5 mm		15 mm ± 0.5 mm		25 mm ± 0.5 mm		35 mm ± 0.5 mm	
	FWHM (mm)	FWTM (mm)	FWHM (mm)	FWTM (mm)	FWHM (mm)	FWTM (mm)	FWHM (mm)	FWTM (mm)	FWHM (mm)	FWTM (mm)	FWHM (mm)	FWTM (mm)
At axial center												
Radial	1.28	3.16	1.50	3.39	1.53	3.34	1.69	3.40	2.34	3.64	2.36	4.04
Tangential	1.18	3.05	1.46	3.36	1.49	3.58	1.67	4.28	2.02	7.27	2.34	-
Axial	0.93	2.68	1.13	2.78	1.09	2.85	1.20	3.05	1.23	3.29	1.32	3.46
At 1/4 axial FOV from center												
Radial	1.20	3.02	1.46	3.32	1.36	3.16	1.63	3.27	2.39	3.65	2.48	4.30
Tangential	1.14	2.98	1.33	3.19	1.41	3.42	1.67	4.14	1.90	7.21	2.11	7.00
Axial	1.43	2.94	1.43	2.93	1.51	2.99	1.11	3.08	1.19	3.36	1.80	4.13

Table 4.12: Spatial resolution values, FBP reconstruction.

Reconstructed image pixel size (mm): 0.1
Slice thickness (mm): 0.1

	0 mm ± 0.5 mm		5 mm ± 0.5 mm		10 mm ± 0.5 mm		15 mm ± 0.5 mm		25 mm ± 0.5 mm		35 mm ± 0.5 mm	
	FWHM (mm)	FWTM (mm)	FWHM (mm)	FWTM (mm)	FWHM (mm)	FWTM (mm)	FWHM (mm)	FWTM (mm)	FWHM (mm)	FWTM (mm)	FWHM (mm)	FWTM (mm)
At axial center												
Radial	0.60	1.34	0.82	1.46	0.83	1.55	0.91	1.78	1.11	1.98	1.08	1.98
Tangential	0.97	1.47	0.87	1.63	0.85	1.66	0.86	1.76	0.96	1.90	1.00	1.93
Axial	0.55	1.31	0.46	1.41	0.77	1.41	0.72	1.40	0.72	1.40	0.72	1.39
At 1/4 axial FOV from center												
Radial	0.60	1.34	0.89	1.31	0.71	1.50	0.85	1.73	1.06	1.91	1.04	1.86
Tangential	0.81	1.45	0.94	1.41	0.86	1.61	0.89	1.71	0.93	1.82	1.01	1.91
Axial	0.62	1.25	0.72	1.16	0.67	1.26	0.71	1.34	0.68	1.30	0.66	1.30

Table 4.13: Spatial resolution values, Tera-Tomo.

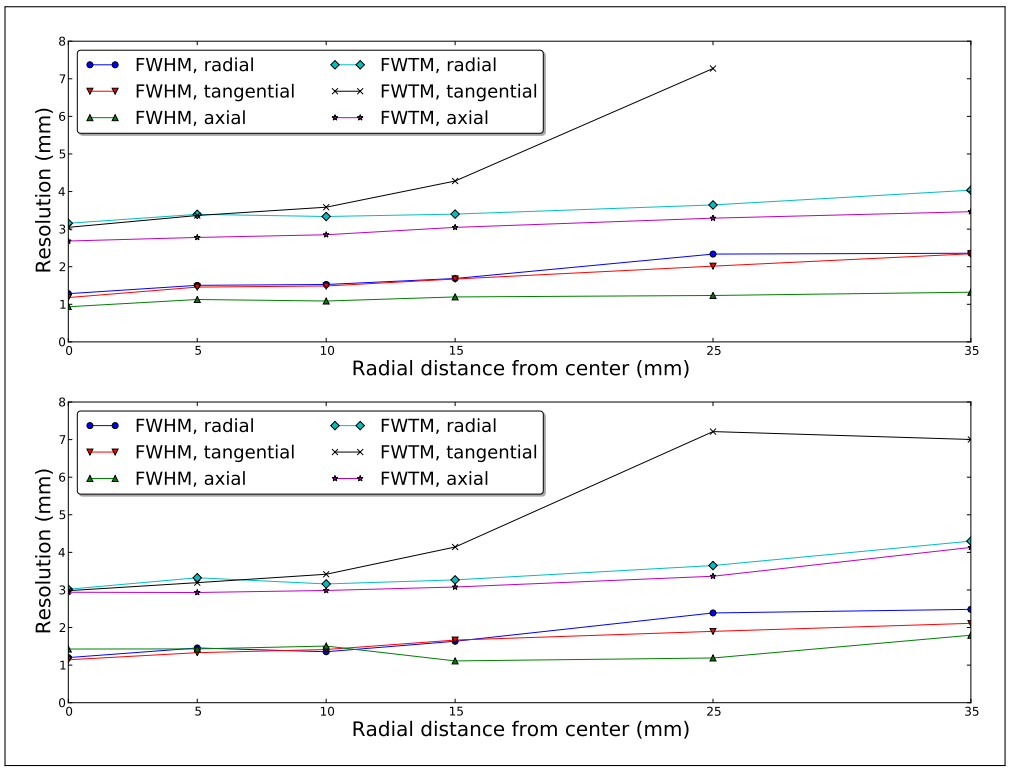

Figure 4.3: Spatial resolution of images reconstructed with filtered back-projection, at center of axial FOV (above) and at one-quarter FOV from center (below). The spatial resolutions are plotted as a function of radial distance from center.

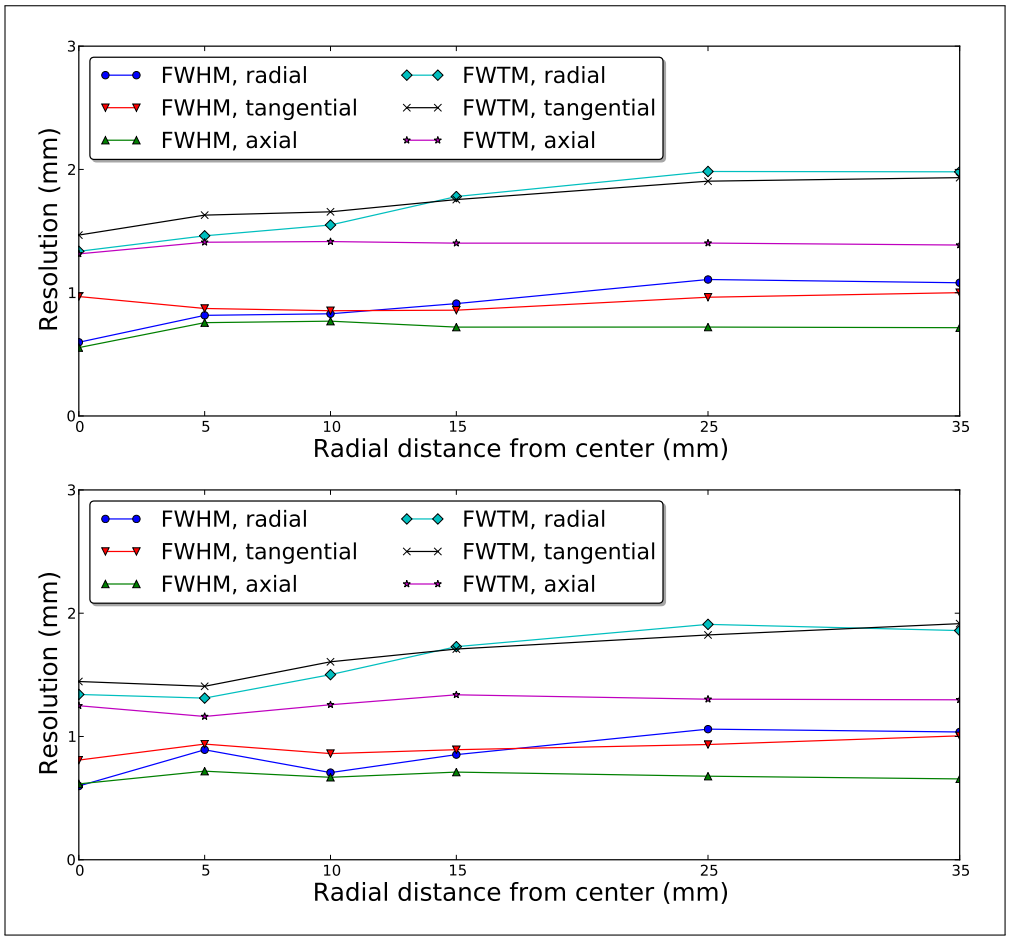

Figure 4.4: Spatial resolution of images reconstructed with Tera-Tomo, at center of axial FOV (above) and at one-quarter FOV from center (below). The spatial resolutions are plotted as a function of radial distance from center.

4.2.2 Scatter Fraction, Count Losses, and Random Coincidence Measurements

The scatter fraction of the mouse phantom is 19.3%.

Figure 4.5 is a plot of the following five quantities as a function of the average activity, $A_{ave,j}$: system true event rate, system random event rate, system scattered event rate, system noise equivalent count rate and system total event rate.

The peak values and activity of these curves are given in Table 4.14. The count rates increase till they reach peak around 40 MBq, and then they all start to decrease again. It is seen that the number of true events is substantially higher than the number of random and scattered events. Thus, the total event rate consists primarily of true events.

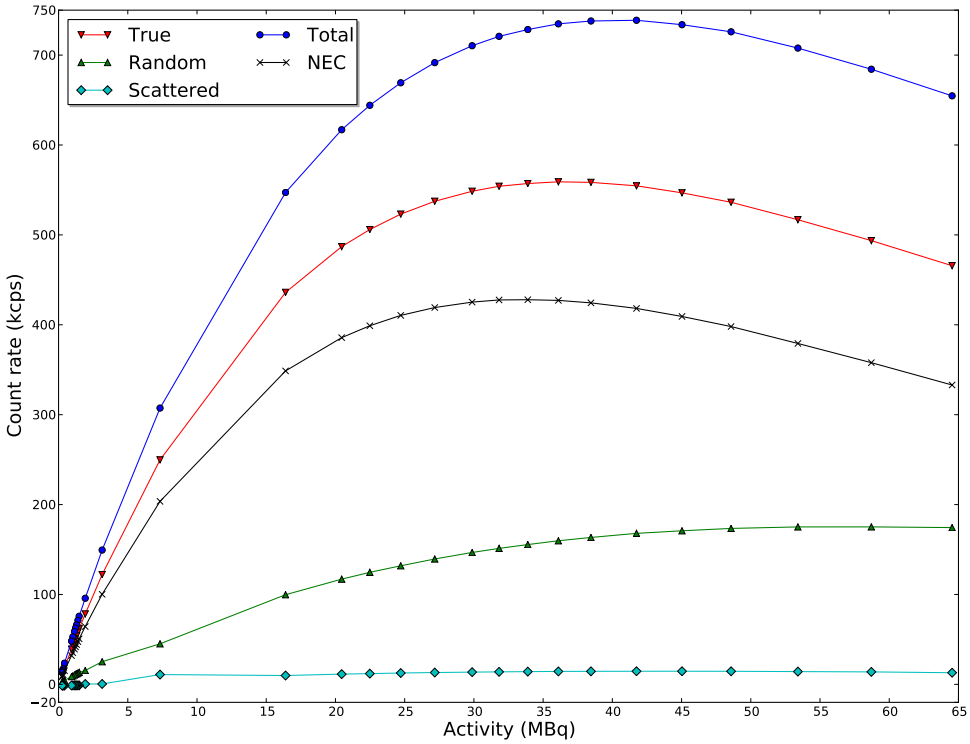

Figure 4.5: System true, random, scattered and total event rate and system noise equivalent count rate as a function of average activity.

	Peak (kcps)	Activity at Peak (MBq)
True event rate	559.0	36
Random event rate	175.2	58
Scattered event rate	14.6	45
Noise equivalent count rate	427.9	33
Total event rate	738.7	41

Table 4.14: Peak values of count rate plot, Figure 4.5.

4.2.3 Sensitivity

The axial sensitivity profile, i.e. the absolute sensitivity of the scanner as a function of axial position of point source, is shown in Figure 4.6, with the corresponding data in Table 4.16.

The peak of the axial profile is approximately in the center of axial FOV. The sensitivity and absolute sensitivity at center of FOV, and the average sensitivity and absolute sensitivity for the mouse-sized region and for the total axial FOV is given in Table 4.15.

The absolute sensitivity at center of FOV is 8.8%, and the average absolute sensitivity of the total axial FOV is 5.1%. In a mouse-sized region the average absolute sensitivity is 6.1%.

	Sensitivity (cps/kBq)	Absolute Sensitivity (%)
At center of FOV	79.9	8.8
Mouse-sized region	55.1	6.1
Total axial FOV	46.5	5.1

Table 4.15: Sensitivity and absolute sensitivity at center of FOV, and average sensitivity and average absolute sensitivity over mouse-sized region and over total axial FOV.

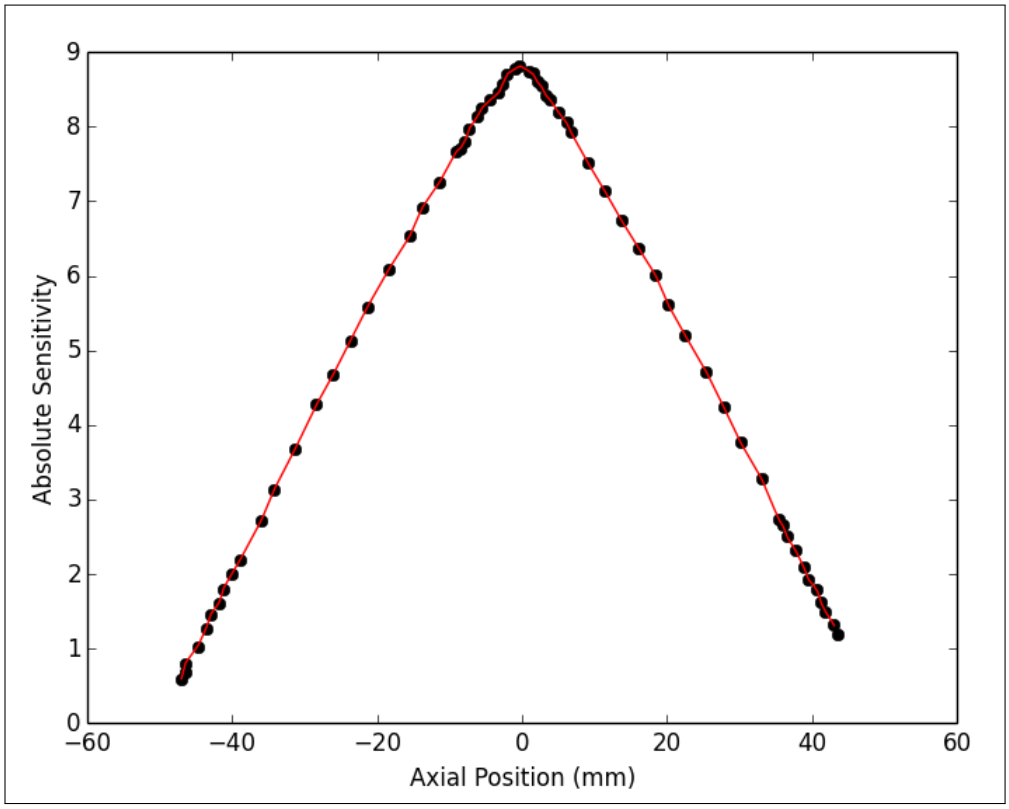

Figure 4.6: Axial absolute sensitivity profile. Axial FOV is 94 mm long, so the values go from -47 mm to +47 mm. The black dots are the data points, and the interpolation, linear point-to-point, is shown with a red line.

Axial Position (mm)	**SA (%)**	**Axial Position (mm)**	**SA (%)**	**Axial Position (mm)**	**SA (%)**	**Axial Position (mm)**	**SA (%)**
-47.1	0.6	-21.4	5.6	-0.3	8.8	22.5	5.2
-46.5	0.7	-18.4	6.1	0.9	8.8	25.4	4.7
-46.5	0.8	-15.5	6.5	1.5	8.7	27.8	4.3
-44.8	1.0	-13.7	6.9	2.0	8.6	30.1	3.8
-43.6	1.3	-11.4	7.3	2.6	8.6	33.1	3.3
-43.0	1.5	-9.1	7.7	3.2	8.4	35.4	2.7
-41.8	1.6	-8.5	7.7	3.8	8.4	36.0	2.7
-41.2	1.8	-7.9	7.8	5.0	8.2	36.6	2.5
-40.1	2.0	-7.3	8.0	6.1	8.1	37.7	2.3
-38.9	2.2	-6.1	8.1	6.7	7.9	38.9	2.1
-36.0	2.7	-5.6	8.3	9.1	7.5	39.5	1.9
-34.2	3.1	-4.4	8.4	11.4	7.1	40.7	1.8
-31.3	3.7	-3.2	8.5	13.7	6.7	41.2	1.6
-28.4	4.3	-2.6	8.6	16.1	6.4	41.8	1.5
-26.0	4.7	-2.0	8.7	18.4	6.0	43.0	1.3
-23.7	5.1	-0.9	8.8	20.2	5.6	43.6	1.2

Table 4.16: Absolute sensitivity, SA, and axial position of point source compared to center of axial FOV.

4.2.4 NEMA Image Quality Phantom Study

This test was done to extract image uniformity, values of resolution recovery coefficients, and accuracy of data corrections.

Uniformity

The results from the uniformity test are given in Table 4.17. The mean activity concentration is 167.1 kBq/ml, with a percentage standard deviation (%STD) of 4.7%. The activity in the phantom at scan start was 3.7 MBq, and the phantom can be filled by approximately 22 ml. The uniform region should therefore have a mean concentration at about 3.7 MBq/22 ml = 168.2 kBq/ml. This is in accordance with measured mean activity concentration.

Recovery Coefficients

The recovery coefficients from the five rods are given in Table 4.18, and shown in Figure 4.7. The recovery coefficients should be as close to 1 as possible, since the activity is uniformly distributed in the phantom. Rods with diameter 3 mm, 4 mm and 5 mm have recovery coefficient of approximately 1, and the rod with diameter 2 mm has recovery coefficient 0.84. The 1 mm diameter rod has recovery coefficient 0.16. The standard deviation increases as the rod diameter decreases.

The phantom was supposed to be aligned with the axis of the tomograph's FOV, but was in the experimental setting shifted a few pixels. This should not be a problem, except when finding the recovery coefficient of the smallest rod, see discussion in Section 5.2.

Accuracy of Corrections

The accuracy of scatter corrections are given as the spill-over ratio in cold regions. The spill-over ratio and %STD in the water- and air-filled cylinders are reported in Table 4.19. The spill-over ratio is 0.10 and 0.09 for both water-filled and air-filled cylinder, respectively.

	Mean (kBq/ml)	Maximum (kBq/ml)	Minimum (kBq/ml)	%STD
Uniformity	167.1	209.9	127.9	4.7

Table 4.17: Uniformity test; mean, maximum and minimum activity concentration, as well as percentage standard deviation (%STD).

Rod Diameter (mm)	RC	%STD
1	0.16	30.7
2	0.84	25.7
3	1.08	20.5
4	1.08	19.7
5	1.09	11.6

Table 4.18: Recovery Coefficients (RC) and percentage standard deviation (%STD) for rods with diameter 1, 2, 3, 4 and 5 mm.

	SOR	%STD
Water-filled cylinder	0.10	12.4
Air-filled cylinder	0.09	14.1

Table 4.19: Spill-over ratio (SOR) and percentage standard deviation (%STD) for water- and air-filled cylinder.

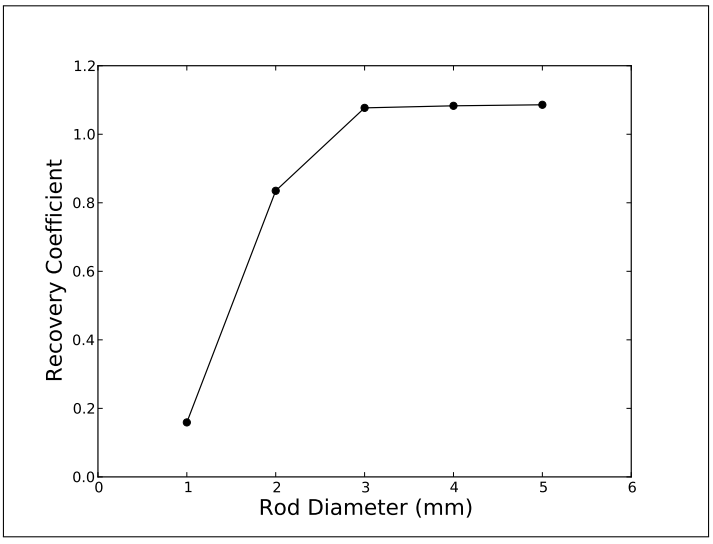

Figure 4.7: Recovery coefficients of rods as function of rod diameter.

Chapter 5

Discussion

In order to understand the findings in the results section, it is necessary to compare these findings with previous reports both with tests from the same system/vendor and with tests from other systems/vendors. Thus, this chapter discusses the findings of the current thesis, in light of existing literature, and presents the shortcomings of the methodology alongside future recommendations.

5.1 CT Subsystem

Hounsfield Quality Check

By definition, water should have CT-number 0 HU, and air should have CT-number -1000 HU. There was quite some deviation from this in the non-automatic test, especially in the air region. A noticeable source of error was the cut at -1000 HU in the images from the non-automatic test. It is not possible to achieve an average CT-number of -1000 HU in the air region if all measured CT-numbers are -1000 HU and higher. Still, this does not explain all deviation from defined CT-numbers, as there was a deviation in the water region as well.

The acquisition parameters of the automatic and non-automatic test were different, since detailed information about the automatic test was not obtained from the vendor before the non-automatic test was done. This might be one reason why the results are different, but it doesn't explain why the CT-numbers are cut at -1000 HU in the non-automatic test and not in the automatic test. It was not given whether the automatic test was scanned with semicircular half scan or full scan, but if it was scanned with full scan it might explain why the noise was lower in the automatic test.

It should be possible to reproduce the automatic test, since this test and the non-automatic test was performed the same day with the same phantom. However, this cannot be properly done before the reason for the cut at -1000 HU is found, and before the vendor provide complete acquisition parameters. It has been checked whether or not it is the analysis software InterView FUSION which is the problem, and it turned out not to be the case, as the values in the DICOM images were cut at -1000 HU also when opening them in a different software program (Python).

The image homogeneity measurement indicated that the images were homogeneous. As the CT-numbers are cut at -1000, the air chamber has a smaller range of CT-numbers than the water chamber, and therefore a lower standard deviation. This however does not mean less noise in the images.

Noise in Reconstruction Filters

The order of the filters, when sorted from highest to lowest according to standard deviation of noise in the reconstructed images, was in accordance with theory, Section 2.5.3. RamLak was the filter with most noise and BlackMan with least noise.

There was not found a significant difference in the reconstruction filters, the mean CT numbers were similar and there were no obvious visible differences in the images reconstructed with different filters. It could have been useful to scan the phantom with an even more diluted contrast agent, to see if a difference would be visible in the low-contrast image.

Different Scanning Methods

This test evaluated the scan time, dose, artefacts and signal-to-noise ratios (SNRs) for the four scanning methods. Based on the results, the following recommendations are suggested:

- **Semicircular, full scan**
  This scanning method came out similar to or worse than “helical, 1 pitch” in all comparisons, and thus a simple “helical, 1 pitch” would be recommended over this scanning option.
- **Semicircular, half scan**
  ”Semicircular, half scan“ had the shortest scan time, but the images with highest noise and most artefacts. If, for a special experiment, low scan time is more important than dose and CT image quality, then this would be the best scanning method.
- **Helical, 0.5 pitch**
  ”Helical, 0.5 pitch” gave the images with highest quality, but at the cost of more scan time and more dose to animal. Before using this scanning

method, it must be taken into consideration whether or not good image quality is worth exposing the animal for more dose and longer scan time.

- **Helical, 1 pitch**
  ”Helical 1 pitch” would be the scanning method of choice in most contexts, based on these few tests only. Lowest dose, quite good images, and just a few minutes longer scan time than “semicircular, half scan”, which had the lowest scan time.

The differences in dose between the different scanning methods were as expected. “Semicircular, half scan” and “semicircular, full scan” had the same dose, as the acquisitions were done with the same number of projections. “Helical, 0.5 pitch” had double dose compared to “helical, 1 pitch” which also was expected since “helical, 0.5 pitch” had twice as many rotations as “helical, 1 pitch”.

Scan time and dose were also checked for different tube voltages and currents. With time kept fixed, the dose changed with tube voltage and current. For all scanning methods, the dose was lowest for 35 kV_p and 1000 μA, and almost the same for 50 kV_p and 670 μA, and 70 kV_p and 310 μA. The dose is only proportional to the mAs when the tube voltage is kept constant. The reason why the dose for 35 kV_p was a factor 2 lower than the dose for 50 kV_p and 70 kV_p and 310 μA can be that with 35 kV_p, a larger part of the x-rays might have been stopped by the filter in front of the x-ray tube, which removes the x-rays with lowest energy.

5.2 PET Subsystem

The PET subsystem was evaluated according to the NEMA NU 4-2008 standard. All results were more or less as expected, compared to performance evaluations of the PET systems from the same vendor. This is a very reassuring finding as the vendor is not testing each produced scanner according to the NEMA NU 4-2008 standard. In this section, the current system is compared to the scanner evaluations described in Section 2.8 and in Appendix A.

Spatial Resolution

The scanner in this project has one of the best spatial resolutions (0.9 - 1.4 mm full width at half maximum (FWHM) at center of field of view (FOV) using FBP) compared to the other commercial preclinical scanners (1.3 - 4.1 mm FWHM at center of FOV using FBP [33–35]). As the comparisons are done using the same reconstruction method (FBP), this difference is due to hardware configuration, i.e. optimal contribution of scintillator crystals and readout.

At center of FOV the FWHM resolution values when reconstructed with Tera-Tomo reconstruction approach 0.4 mm, which is the resolution value needed for a mouse to be scanned with an equivalent spatial resolution value as humans scanned in clinical PET scanners [3]. So the spatial resolution values were much improved by changing reconstruction algorithm from filtered back-projection to Tera-Tomo reconstruction. This is also visible in the image of the point source reconstructed with FBP and Tera-Tomo, Figure 3.12, where noise-streaks are present around the point source reconstructed with FBP.

The response functions were made by summing the one-dimensional profiles that were parallel to the direction of measurement. If there was a lot of noise in either of the directions, this would contribute to the response functions; and the full width at tenth maximum (FWTM) values would increase substantially. The noise contribution could also be large enough so that none of the intensity values would be under 10% of the maximum value, and therefore make a FWTM value not achievable. This is what might have happened in the tangential direction, Figure 4.3, where there suddenly is a step from approximately 4 mm FWTM at 15 mm radial distance center to approximately 7 mm FWTM at 25 mm radial distance from center. At the center of axial FOV, 35 mm radial distance from center, the FWTM in tangential direction was not possible to compute.

Scatter Fraction, Count Losses, and Random Coincidence Measurements

The scatter fraction was 19.3%. This value was a bit higher than the scatter fractions found by Szanda et al. (2011) for the NanoPET/CT (15%) and Nagy et al. (2013) for the nanoScan PET/MRI (17.3%). The scatter fraction was also higher than the average scatter fraction of the systems evaluated by Goertzen et al. (2012) (average scatter fraction was approximately 12%). The scatter fraction was calculated at activities between 1 and 1.5 MBq, where the random event rate was expected to be negligible compared to the scatter event rate. If the random event rate was not really negligible compared to the scatter event rate, this will give a larger scatter fraction. Remember, the lower scatter fraction the better.

For low activities, the count rates increase proportionally with the activity. This is as expected, as higher activity means more disintegrations, and therefore more hits. But at one point the detectors will no longer be able to keep up with the increasing number of hits, due to detector dead time. This happened at 40 MBq with a peak count of 738.7 kcps for total event rate.

The noise equivalent count rate (NECR) increases toward 33 MBq, where it reaches its maximum; 427.9 kcps. This is quite similar to the peak of the NECR curve found by Szanda et al. (2011) for the NanoPET/CT system; 430 kcps at 36 MBq. The peak of the NECR curve found by Nagy et al. (2013) for

the nanoScan PET/MRI system was 406 kcps at 0.847 MBq/ml. This seems quite similar as well, but the volume of the phantom was not given so it is not certain what the activity was at the peak. Since preclinical systems from different vendors have a wide variation in design, it is not useful to compare the NECR curve with the curves found by Goertzen et al. (2012).

Sensitivity

The axial absolute sensitivity profile was as expected; highest at the center of axial FOV, and then decreasing towards the edges of the FOV. The absolute sensitivity measured at center of FOV was 8.8%, which is quite good as the highest reported absolute sensitivity at center of FOV is approximately 10%, according to Yao et al. (2012) [3]. The vendor reported 9% as the absolute sensitivity at center of FOV, and Nagy et al. (2013) reported 8.5% as absolute sensitivity at center of FOV for the nanoScan PET/MRI. So the absolute sensitivity at center of FOV found in this project is consistent with the values found in other evaluations of the same model.

In Goertzen et al. (2012) the scanners from before 2003 has absolute sensitivity at center of FOV from 1.19% - 3.03%, and after 2003 scanners has from 2.22% - 6.72%. So with time, there have been developed PET scanners with better and better sensitivity, most likely due to improvements in crystal material, homogeneity of crystal growth process and developments in electronics. The PET scanner evaluated in this thesis has one of the best reported sensitivities of commercial preclinical scanners.

NEMA Image Quality Phantom Study

The uniformity test had a percentage standard deviation (%STD) of 4.7%, and the max/mean ratio and min/mean ratio were 1.26 and 0.77, respectively. The %STD is higher than the value reported by the vendor in the contract, i.e. 2.74% with Tera-Tomo reconstruction, and the value reported by Nagy et al. (2013) for the nanoScan PET/MRI system, i.e. 3.52%. Still, compared to older systems, a %STD of 4.7% is a good uniformity. The scanners evaluated by Goertzen et al. (2012) had %STD in the uniformity region in the range 4.5%-15.4%. The max/mean and min/mean ratios were quite similar to the ratios of almost all of the systems reported by Goertzen et al. (2012).

The recovery coefficients (RC) are supposed to be 1 in a perfect system, as the activity concentration should stay the same throughout a homogeneously filled phantom. The RCs found in this test were approximately 1 for rods with diameter 3 mm, 4 mm and 5 mm, and 0.8 for the rod with diameter 2 mm. The rod with diameter 1 mm had RC of less than 0.2. These RCs were very similar to the RCs reported by the vendor and the RCs reported by Nagy et al. (2013) for the nanoScan PET/MRI system (the RCs reported by vendor and

Nagy et. al (2013) where all approximately 1 for rods with diameter 3 mm, 4 mm and 5 mm, 0.8 for rod with diameter 2 mm and less than 0.3 for rod with diameter 1 mm). The RCs found in this thesis, and by the vendor and by Nagy et al. (2013), were found in images reconstructed with Tera-Tomo. This test is highly dependent on the reconstruction algorithm, as shown by Goertzen et al. (2012), so it is not useful comparing it to the other scanners.

The spill-over ratios (SORs) are supposed to be 0 in a perfect system, since there is no activity in cold areas. The SORs found in this thesis were 0.10 and 0.09 for water- and air-filled cylinders, respectively. The SORs reported by the vendor (0.07 and 0.06 for water- and air-filled cylinders, respectively), and the SORs reported by Nagy et al. (2013) for the nanoScan PET/MRI system (0.06 for both water- and air-filled cylinders) were quite similar, although a bit lower.

The image quality phantom was not aligned perfectly with the axis of the tomograph's field of view, but shifted a few pixels. Error because of this might be present in the recovery coefficient of the rod with diameter 1 mm. The voxel size is 0.4 mm x 0.4 mm x 0.4 mm, so a shift of 2-3 pixels will mean a shift of around 1 mm. The recovery coefficients were found by taking the mean value of a straight line of pixels in the rod. If the rod is not aligned perfectly with the tomograph's field of view, this straight line of pixels would not contain only pixels from the rod. Some pixels would be in cold areas, and therefore make the recovery coefficient smaller than it should be, i.e. partial volume effect.

Limitations of NEMA NU 4-2008

NEMA NU 4-2008 is a widely accepted standardized method for evaluating the performance of small-animal PET scanners. For it to be possible for this standard to be applied to the majority of preclinical PET scanners, the standard has to be general enough for it to apply to all the scanners based on common methodology available on the scanner systems. This puts limitations on how thoroughly the performance evaluation reflects the true performance of a system.

One limitation is the use of filtered back-projection (FBP) in the evaluation of spatial resolution. Vendors of most preclinical PET systems offer iterative 3-dimensional reconstruction algorithms. For these systems, the FBP algorithm requirement in the NEMA NU 4-2008 standard leads to situations which are never realized in routine imaging situations. The iterative algorithms are better, as they will try to compensate for physical/technological limitations, e.g. scanner geometry and positron range. However, although iterative methods may have very good results for synthetic tests; this will not necessarily be reflected in images of animal. This is a reason for using FBP in NEMA, in addition to it being available on most scanners. The limitation in

the spatial resolution test caused by choice of reconstruction algorithm does not presently have a practical solution [35].

Furthermore, the NEMA NU 4-2008 standard is not very easy to follow, and as such there may be different interpretations on how to perform the evaluation. It would have been easier to understand the standard if there had been more figures which could explain the text. To ensure that everyone who uses the NEMA NU 4-2008 standard do everything correctly, the standard could have been provided with Python or MATLAB scripts. In the current work all analysis tools had to be implemented in parallel with performing the tests.

5.3 Practical Limitations of the PET/CT Evaluation

The nanoScan PET/CT system had just been installed at the PET center in Bergen when this work started. The PET/CT scanner has many scanning and reconstruction options, so it took some time to get to know the scanner. The user manual was not very helpful, it seemed quite incomplete. Communication with vendor was not so good either; it took quite a long time to get answers. This was particularly the case in the part of the NEMA standard which required sinograms, since it was hard to find the sinograms on the scanner, and no information was available on the format of the sinograms.

In the beginning, it was also a problem filling the fillable phantoms. Phantoms for preclinical scanners are small, and it is difficult to fill the phantoms uniformly without any air bubbles. It took some time to find a solution to this problem, but in the end it was solved by using a laboratory centrifuge. The centrifuge forced all the bubbles to the top of the phantom, and when at the top, more liquid were added to the phantom to get the bubbles out.

A last problem with the materials was that the PET reconstructions often were really slow and crashed during processing, so the reconstructions had to be restarted multiple times. The vendor is still attempting to solve this problem. Luckily this does not influence the quality of the measurements, but it is very time consuming.

In summary, the scanner gives at the moment good images. The tests done in this thesis should be repeated regularly to be able to detect changes in system performance, i.e. detector degradation. The problem with the CT-numbers should also be fixed.

5.4 Implications for In Vivo Imaging

The spatial resolution when reconstructing with Tera-Tomo is approaching the resolution value needed for a mouse to be scanned with an equivalent

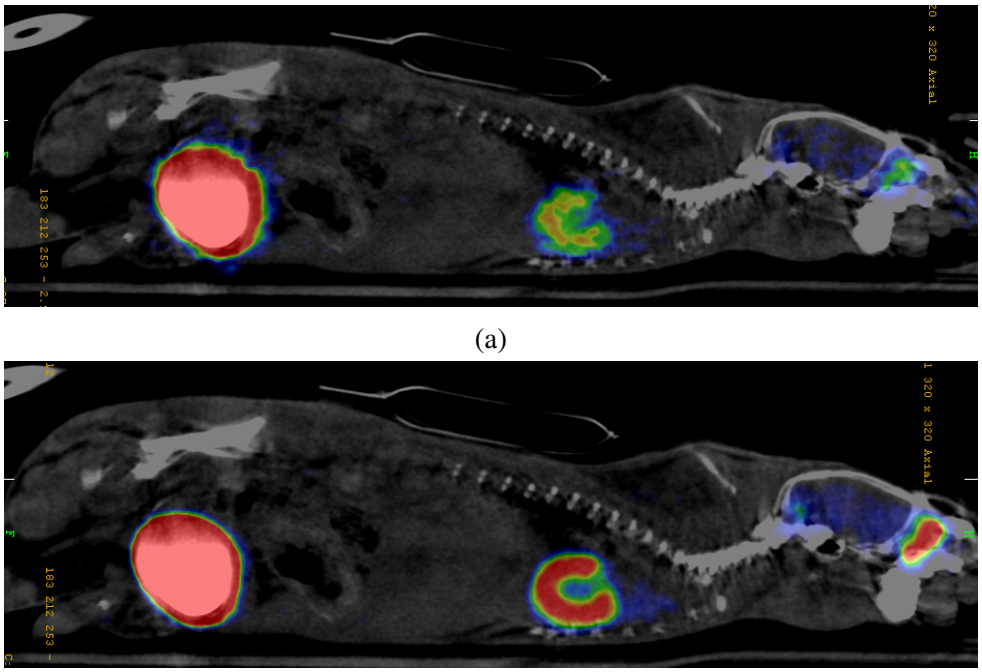

(a)

(b)

Figure 5.1: A PET/CT scan of a mouse. PET part is reconstructed with (a) filtered back-projection and (b) Tera-Tomo.

spatial resolution value as humans scanned in clinical PET scanners. At the same time, the spatial resolution is approaching its physically limited spatial resolution; the limitation set by the positron range of ^{18}F (mean range is 0.6 mm). So Tera-Tomo reconstruction is approaching the best possible achievable spatial resolution when scanning with ^{18}F. For other radioisotopes, other spatial resolutions will be expected, as the mean positron range depends on the radioisotope. The spatial resolution measured in this thesis was measured with the standard NEMA point source, but, as already mentioned, ^{22}Na and ^{18}F have very similar positron ranges.

Figure 5.1 illustrates the difference between the two reconstruction methods filtered back-projection and Tera-Tomo. The reconstruction parameters of these images are given in Table 5.1. The PET resolution in these two images are quite different, but both images show three areas with increased uptake of FDG; the brain, the heart and the bladder. The 3D Tera-Tomo reconstruction clearly outperforms the 2D FBP method.

The sensitivity profile of the scanner system is substantial, as seen in Figure 4.6. If not corrected for, the standardized uptake values would have been reduced by 50% in the periphery (i.e. brain) compared to the central regions (i.e. heart). For in vivo imaging however, the loss of sensitivity towards the edges of the FOV is automatically corrected for.

	FBP	**Tera-Tomo**
Reconstruction Mode:	2D	3D
Energy window:	250-750 keV	400-600 keV
Coincidence mode:	1-5	1-5
Reconstruction:	FBP	Tera-Tomo
Rebinning Method:	SSRB SINO	-
Random Corrections:	Delayed Window	Delayed Window
Normalization:	ON	ON
Dead time Correction:	ON	ON
Attenuation Correction:	ON	ON

Table 5.1: PET reconstruction parameters, mouse image.

As mentioned in Section 2.7.5, the signal-to-noise ratio in the final reconstructed images is proportional to the NECR. Therefore, it is not necessary to inject more than 33 MBq (where the NECR curve peaked) in a mouse, because higher activity will not increase image quality, it will only give more dose to the animal. However, going past the NECR peak is not an issue in daily use of the scanner, as the animals normally are injected with a radiotracer with activity of 5-10 MBq.

Chapter 6

Conclusion and Future Work

In this work, the performance of the nanoScan PET/CT system was evaluated for the first time. An abbreviated performance evaluation of the CT subsystem was done, together with a complete NEMA NU 4-2008 performance evaluation of the PET subsystem.

The CT subsystem has proved adequate for its intended use, although the cut of CT-numbers at -1000 HU should be fixed by the vendor. The CT images were homogeneous, but with some noise. The "helical, 0.5 pitch" scanning method had best image quality. For the sake of the animals, "helical, 1 pitch" was the best scanning method, with lowest dose, quite good images, and just a few minutes longer scan time than "semicircular, half scan", when scanning one field of view. The reconstruction filters were in accordance to theory.

The main performance parameters of the PET subsystem are all similar to or exceed those of comparable systems, making this one of the best preclinical commercial PET scanners available at the moment. The spatial resolution according to the NEMA NU 4-2008 standard is approximately 1 mm at the center of field of view (FOV), which is the highest among currently available commercial systems. The sensitivity at center of FOV was 8.8%, just a bit lower than the highest reported absolute sensitivity at center of FOV, i.e. 10%. The counting rate capabilities have proved adequate for all applications undertaken to date, and the NEMA image quality phantom study demonstrated good values of uniformity and recovery coefficients.

The work in this thesis is of importance to all imaging studies on the system, particularly those that include quantitative assessments. The implementations and increased level of understanding gained by this project will substantially ease redoing the evaluations in the future. Such evaluations should be done regularly to assure stability and robust measurement.

In future work, it would be particularly interesting to see how the current performance of the scanner influences physical modelling of a metabolic pro-

cess, i.e. tracer kinetic modelling in dynamic PET acquisitions. Furthermore, to similarly perform a performance evaluation of the novel human PET/MRI system that will be installed in a few years (possible in 2016).

Bibliography

[1] Willi A. Kalender. *Computed Tomography: Fundamentals, System Technology, Image Quality, Applications*. Publicis, 3rd edition, 2011.

[2] Siman R. Cherry, James A. Sorenson, and Michael E. Phelps. *Physics in Nuclear Medicine*. Saunders, 4th edition, 2012.

[3] Rutao Yao, Roger Lecomte, and Elpida S. Crawford. Small-Animal PET: What Is It, and Why Do We Need It? *Journal of nuclear medicine technology*, 40(3):157–165, 2012.

[4] National Electrical Manufacturers Association. *Performance Measurements for Small Animal Positron Emission Tomographs*. NEMA Standard Publication NU 4-2008.

[5] Tor F. Thorsteinsen. Kompendium i strålingsfysikk. Fysisk institutt - Universitetet i Bergen, 1995.

[6] Penelope Allisy-Roberts and Jerry Williams. *Farr's Physics for Medical Imaging*. Saunders Ltd., 2nd edition, 2007.

[7] Scintillator Materials Group at Stanford University. What are scintillator materials? http://www.stanford.edu/group/scintillators/scintillators.html. Accessed: 01.06.2014.

[8] Tom K. Lewellen. Recent developments in PET detector technology. *Physics in medicine and biology*, 53(17):R287, 2008.

[9] Hamamatsu Photonics. *Photomultiplier Tubes, Basics and Applications*. Hamamatsu, 3nd edition, 2007.

[10] E.B. Podgorsak. *Radiation Oncology Physics: A Handbook for Teachers and Students*. IAEA, 2005.

[11] Statens strålevern. Stråledoser og grenseverdier. http://www.nrpa.no, August 2011. Accessed: 13.11.2013.

[12] Jack Valentin. *The 2007 Recommendations of the International Commission on Radiological Protection*. Elsevier Oxford, 2007.

[13] Gabor T. Herman. *Fundamentals of Computerized Tomography, Image Reconstruction from Projections*. Springer, 2nd edition, 2009.

[14] Greg Michael. X-ray computed tomography. 36(6):442–451, 2001.

[15] William C Scarfe, Allan G Farman, and Predag Sukovic. Clinical applications of cone-beam computed tomography in dental practice. *Journal of the Canadian Dental Association*, 72(1), 2006.

[16] William C. Scarfe and Allan G. Farman. What is Cone-Beam CT and How Does it Work? *Dental Clinics of North America*, 52(4):707–730, 2008.

[17] Mediso. NanoScan PET-CT, Operator's Manual.

[18] Gábor Jakab, Attila Rácz, and Kálmán Nagy. High quality cone-beam CT reconstruction on the GPU. *Hungarian Association for Image Processing and Pattern Recognition. Budapest, Hungary*, 2011.

[19] Keith J. Strauss. Radiation safety summit - method to estimate radiation dose to pediatric patients from CT scans. *Pediatric Radiology*, 41:210–211, 2011.

[20] Paul A. Tipler and Ralph A. Llewellyn. *Modern Physics*. W. H. Freeman, 5th edition, 2008.

[21] Mohammad Dawood, Xiaoyi Jiang, and Klaus Schäfers. *Correction Techniquies in Emission Tomography*. CRC Press, 1st edition, 2012.

[22] Eveline Miele et al. Positron Emission Tomography (PET) radiotracers in oncology - utility of 18F-Fluoro-deoxy-glucose (FDG)-PET in the management of patients with non-small-cell lung cancer (NSCLC). *Journal of Experimental & Clinical Cancer Research*, 27, 2008.

[23] P. E. Valk, D. L. Bailey, D. W. Townsend, and M. N. Maisey. *Positron Emission Tomography*. Springer, 2003.

[24] S. Vallabhajosula, L. Solnes, and B. Vallabhajosula. A Broad Overview of Positron Emission Tomography Radiopharmaceuticals and Clinical Applications: What Is New? *Seminars in Nuclear Medicine*, 41, 2011.

[25] Peter Koncz. NanoScan PET-CT, PET Basics. Mediso, 2013.

[26] Gopal B. Saha. *Basics of PET Imaging*. Springer, 2nd edition, 2010.

[27] Federic H. Fahey. Data Acquisition in Pet Imaging. *Journal of nuclear medicine technology*, 30(2):39–49, 2002.

[28] Habib Zaidi and Bruce Hasegawa. Determination of the attenuation map in emission tomography. *Journal of Nuclear Medicine*, 44(2):291–315, 2003.

[29] M. Magdics et al. TeraTomo project: a fully 3D GPU based reconstruction code for exploiting the imaging capability of the NanoPET/CT system. World Molecular Imaging Congress, 2010.

[30] J. Valentin. Radiation Dose to Patients from Radiopharmaceuticals: (Addendum 3 to ICRP Publication 53) icrp publication 160. *Annals of the ICRP*, 2008.

[31] Jan Sijbers and Andrei Postnov. Reduction of ring artifacts in high resolution micro-CT reconstructions. *Physics in Medicine and Biology*, 49(14):N247, 2004.

[32] National Electrical Manufacturers Association. About the national electrical manufacturers association. http://www.nema.org. Accessed: 16.04.2014.

[33] Kálmán Nagy et al. Performance Evaluation of the Small-Animal nanoScan PET/MRI System. *Journal of Nuclear Medicine*, 54(10):1825–1832, 2013.

[34] Istvan Szanda et al. National Electrical Manufacturers Association NU-4 Performance Evaluation of the PET Component of the NanoPET/CT Preclinical PET/CT Scanner. *Journal of Nuclear Medicine*, 52(11):1741–1747, 2011.

[35] Andrew L. Goertzen et al. NEMA NU 4-2008 Comparison of Preclinical PET Imaging Systems. *Journal of Nuclear Medicine*, 53(8):1300–1309, 2012.

[36] National Electrical Manufacturers Association. About dicom. http://dicom.nema.org.

[37] Adam M. Alessio et al. Measured Spatially Variant System Response for PET Image Reconstruction. *Nuclear Science Symposium Conference Record, 2005 IEEE*, 4, 2005.

[38] Quality Assurance in Radiology and Medicine. NEMA NU4 Micro-PET Image Quality Mouse Phantom. http://www.qrm.de. Accessed: 01.07.2014.

Appendices

Appendix A

NEMA NU 4-2008 Performance Data for a Collection of Commercial Animal PET Systems

Included in this appendix is NEMA NU 4-2008 performance data for a collection of commercial animal PET systems manufactured since 2000, Table A.1.

Manufacturer	Model	Performance Evaluation
Mediso	nanoScan PET/CT	Performed by vendor
Mediso	NanoPET/CT	Szanda et al. (2011)
Mediso	nanoScan PET/MRI	Nagy et al. (2013)
Concorde Microsystems/Siemens	microPET P4	Goertzen et al. (2012)
Concorde Microsystems/Siemens	microPET R4	Goertzen et al. (2012)
Concorde Microsystems/Siemens	microPET Focus 120	Goertzen et al. (2012)
Concorde Microsystems/Siemens	microPET Focus 220	Goertzen et al. (2012)
Siemens	Inveon	Goertzen et al. (2012)
Philips	Mosaic HP	Goertzen et al. (2012)
Raytest GmbH	ClearPET	Goertzen et al. (2012)
Sedecal	Argus (formerly eXplore Vista)	Goertzen et al. (2012)
Sedecal	VrPET	Goertzen et al. (2012)
Gamma Medica	LabPET 8	Goertzen et al. (2012)
Gamma Medica	LabPET 12	Goertzen et al. (2012)

Table A.1: Overview of various PET systems manufactured since 2000.

Performance data on the nanoScan PET/CT system is from the system's purchase contract, i.e. Standard Contract for Purchase of Goods.

A.1 Spatial Resolution

The spatial resolution values of the PET systems in Table A.1, at center of axial FOV and at 1/4 of axial FOV from the center, are given in Figure A.1 and in Table A.2.

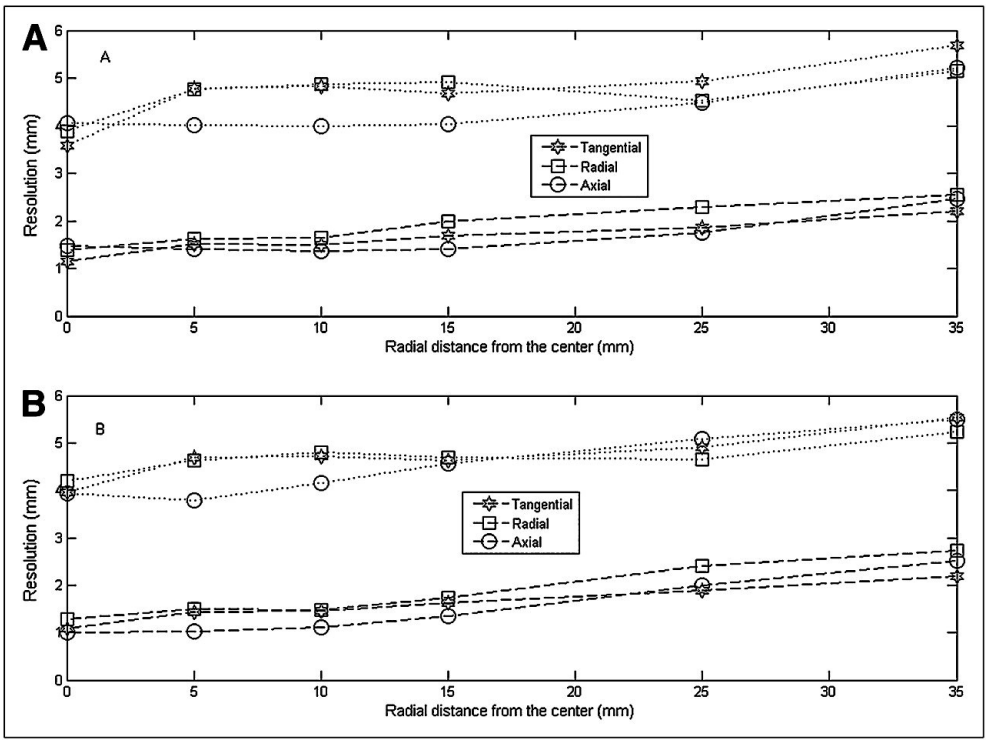

Figure A.1: NanoPET/CT: spatial resolution in center of axial FOV (A) and at 1/4 FOV from center (B). Dashed line and dotted line correspond to FWHM and FWTM, respectively. Reconstruction: SSRB to SINO, FBP [34].

System, energy window, reconstruction	Radial offset) (mm)	FWHM/FWTM (mm) at center			FWHM/FWTM (mm) at 1/4 offset		
		Radial	Tangential	Axial	Radial	Tangential	Axial
NanoScan PET/CT, 400-600 keV, SSRB to 2DLOR, OSEM	1	0.99	0.98	1.29	1.03	0.96	1.38
	10	1.09	0.92	1.28	1.11	0.92	1.37
	25	1.88	1.14	1.81	1.90	1.10	1.80
NanoPET/CT, 250-750 SSRB to SINO, FBP		See Figure A.1.					
NanoScan PET/MRI, 400-600 keV, SSRB to SINO, FBP	5	1.50/3.29	1.32/3.14	0.91/2.85	1.41/3.27	1.33/3.17	1.23/2.92
	10	1.49/3.32	1.39/3.38	1.16/2.93	1.49/3.24	1.43/3.29	0.97/3.10
	15	1.97/4.07	1.54/3.61	1.67/3.33	1.81/3.84	1.48/3.52	1.49/3.38
	25	2.01/4.05	1.65/3.85	1.57/3.42	2.03/4.11	1.70/3.87	1.89/4.10
microPET P4, 350-660 keV, Fourier rebinning + 2D FBP	5	2.29/4.03	2.18/3.81	2.20/4.52	2.34/4.22	2.14/3.77	1.75/4.22
	10	2.41/4.23	2.23/3.92	2.38/4.66	2.37/4.14	2.22/3.84	1.97/4.49
	15	2.42/4.19	2.28/3.83	2.42/4.68	2.39/4.16	2.27/3.87	2.04/4.53
	25	2.61/4.67	2.25/3.76	2.42/4.67	2.53/4.41	2.30/3.91	2.07/4.50
	50	3.27/6.40	2.40/4.10	2.58/5.09	3.20/6.08	2.45/4.29	2.30/4.74
	75	3.92/8.07	2.64/4.53	2.88/5.99	3.78/7.12	2.81/5.15	2.72/5.58
microPET R4, 350-650 keV, Fourier rebinning + 2D FBP	5	2.13/4.90	2.21/4.22	2.72/5.59	2.06/5.24	2.18/4.14	2.37/4.88
	10	2.30/4.60	2.31/4.36	3.02/6.54	2.30/4.61	2.29/4.39	2.66/5.31
	15	2.86/5.38	2.39/4.57	3.25/7.48	2.63/5.35	2.35/4.40	2.84/5.71
	25	3.30/6.32	2.51/4.66	3.27/7.57	3.31/6.23	2.53/4.80	3.09/6.31
microPET Focus 120, 350-650 keV, Fourier rebinning + 2D FBP	5	1.92/3.66	1.66/3.06	1.90/3.81	1.92/3.63	1.65/3.09	1.62/3.28
	10	1.88/3.95	1.74/3.22	1.94/3.91	1.83/3.69	1.76/3.28	1.66/3.34
	15	1.99/4.02	1.72/3.11	1.98/4.05	1.94/3.75	1.77/3.22	1.69/3.41
	25	2.53/4.84	1.73/3.01	2.05/4.34	2.45/4.49	1.80/3.20	1.81/3.67
microPET Focus 220, 250-750 keV, Fourier rebinning + 2D FBP	5	1.75	1.80	1.70	1.70	1.70	1.73
	10	1.68	1.78	1.73	1.66	1.79	1.75
	15	1.82	1.71	1.80	1.88	1.72	1.78
	25	2.07	1.69	1.84	2.09	1.74	1.87
	50	2.88	1.77	1.98	2.82	1.82	1.92
	75	4.08	1.90	2.16	3.92	1.90	2.11
Inveon, 350-625 keV, Fourier rebinning + 2D FBP	5	1.63/3.36	1.62/3.15	2.45/5.62	1.66/3.32	1.63/3.14	1.97/4.20
	10	1.80/3.84	1.58/2.91	2.40/5.51	1.72/3.40	1.64/3.18	2.12/4.44
	15	2.03/4.32	1.56/2.78	2.29/5.32	1.87/3.69	1.63/3.05	2.17/4.72
	25	2.49/5.17	1.61/2.86	2.09/4.67	2.38/4.76	1.65/2.97	2.06/4.54
ClearPET, 250-650 keV, 3D FBP	5	1.94/3.76	2.00/4.17	3.24/6.05	2.18/4.05	1.97/3.92	3.18/5.91
	10	1.85/3.47	2.27/5.97	3.19/5.97	1.87/3.68	2.14/4.86	3.20/5.88
	15	2.01/3.62	2.43/5.53	3.20/5.96	2.05/3.84	2.33/5.25	3.19/5.83
	25	2.55/4.28	2.42/5.69	3.21/5.97	2.50/4.18	2.43/6.59	3.19/5.85
Mosaic HP, 385-665 keV, 3D Fourier reprojection	5	2.32/5.30	2.32/4.97	2.64/6.07	2.33/5.32	2.40/4.88	2.48/5.32
	10	2.45/5.48	2.51/4.96	2.82/6.14	2.37/5.54	2.49/4.97	2.80/5.89
	15	2.43/5.44	2.65/5.24	2.79/6.28	2.48/5.62	2.63/5.25	2.80/5.92
	25	2.59/5.93	2.83/5.25	2.96/6.28	2.63/5.81	2.87/5.31	3.10/6.30
Argus, 250-700 keV, 3D Fourier reprojection	5	1.63	1.65		1.65	1.70	
	10	1.71	1.70		1.74	1.75	
	15	1.85	1.70		1.85	1.75	
	25	2.25	1.73		2.15	1.85	
VrPET, 100-700 keV. SSRB + 2D FBP	5	1.52/2.76	1.62/2.99	2.66/4.81	1.62/2.95	1.68/2.86	2.57/5.21
	10	1.58/2.85	1.68/3.02	3.03/5.45	1.54/2.89	1.68/3.07	3.11/5.45
	15	1.78/3.25	1.51/2.79	3.11/5.50	1.69/3.09	1.73/3.14	3.22/5.72
	25	2.03/3.69	2.12/3.72	3.32/5.92	1.79/3.29	1.98/3.60	3.60/6.87
LabPET 8, 250-650 keV, SSRB + 2D FBP	5	1.65/3.40	1.70/3.30	*	1.57/3.30	1.65/3.50	*
	10	1.91/3.60	1.82/3.67	*	1.92/3.40	1.75/3.45	*
	15	2.01/4.10	1.83/3.70	*	1.92/3.77	1.86/3.90	*
	25	2.56/4.65	1.90/4.28	*	2.55/4.70	1.93/4.30	*

Table A.2: Spatial resolution values (FWHM and FWTM) at axal center of FOV and at 1/4 axial offset [33–35]. (*Axial intrinsic resolution (FWHM/FWTM) = 1.4/4.3 mm).

A.2 Scatter Fraction, Count Losses and Random Coincidence Measurements

A summery of the counting-rate test results of the PET systems in Table A.1 are given inTable A.3.

System	Energy window (keV)	Peak NECR (kcps)	Activity* (MBq)	NECR at 3.7 MBq (kcps)	Scatter fraction (%)
NanoPET/CT	250-750	430	36	Not given	15
nanoScan PET/MRI	250-750	406	0.847 MBq/ml‡	Not given	17.3
microPET P4	350–650	>601†	>174†	22.1	5.2
microPET R4	350–650	618	156	37.2	9.3
microPET Focus 120	350–650	897	103	66.5	5.6
microPET Focus 220	250–700	>763†	>89†	47.3	7.2
Inveon	350–625	1670	131	129	7.8
ClearPET	250–650	73	18	29.3	31
Mosaic HP	385–665	555	92	59.6	5.4
Argus	250–700	117	50	18.7	21
VrPET	100–700	74	22		11.5
LabPET 8	250–650	279	82	23.5	15.6
LabPET 12	250–650	362	81	38.9	16

Table A.3: Summery of counting rate test results for mouse phantom [33–35]. (* Activity at which peak NECR occurs, † Peak value not reached because of insufficient activity at start of scan, ‡ The activity concentration was given instead of activity).

A.3 Sensitivity

A summery of the sensitivity test results of the PET systems in Table A.1 are given in Table A.4 and in Figure A.2.

System	Energy window (keV)	Axial length (cm)	Mouse (absolute) sensitivity (%)	SA_{tot} (%)	Peak detection efficiency (%)
nanoScan PET/CT	250-750	9.4	5*	-	9
NanoPET/CT	250-750	9.5	5.14	-	7.7
nanoScan PET/MRI	250-750	9.4	5.83	-	See Figure A.2
microPET P4	350–650	7.8	0.67	0.61	1.19
microPET R4	350–650	7.8	1.19	1.10	2.06
microPET Focus 220	350–650	7.6	1.26	1.18	2.28
microPET Focus 120	350–650	7.6	1.98	1.82	3.42
Inveon	350–625	12.7	4.0	2.8	6.72
ClearPET	250–650	11.0	2.32	1.87	3.03
Mosaic HP	385–665	11.9	2.43	1.77	2.83
Argus	250–700	4.8			4.32
VrPET	100–700	4.56	1.09	1.09	2.22
LabPET 8	250–650	7.5	1.45	1.42	2.36
LabPET 12	250–650	11.25	3.6	2.74	5.4

Table A.4: Absolute sensitivity over central 7 cm of axial FOV (mouse sensitivity), complete axial FOV (total absolute sensitivity), and peak detection efficiency for various scanners [33–35]. (*At -25 mm from CFOV).

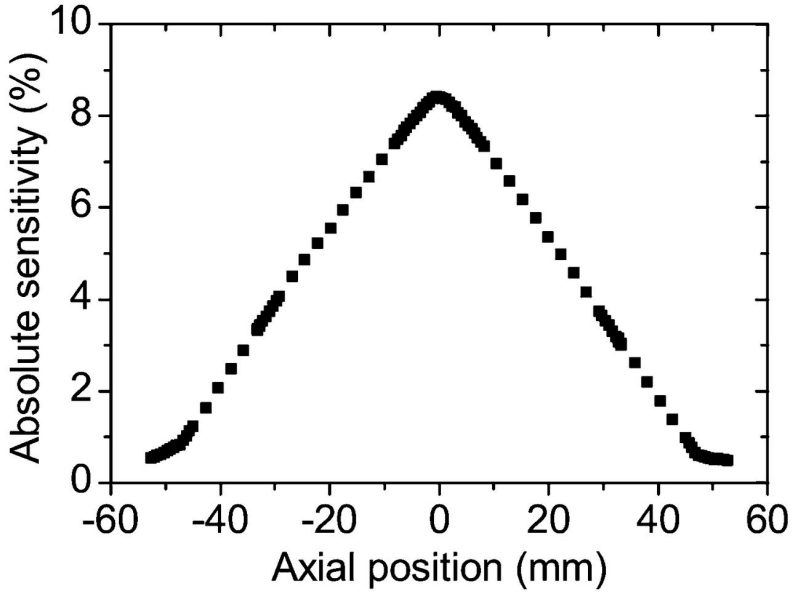

Figure A.2: Axial absolute sensitivity profile, nanoScan PET/MRI [33] .

A.4 NEMA Image Quality Phantom Study

A summery of the results of the NEMA image quality phantom study of the PET systems in Table A.1 are given in Table A.5.

System	Energy window (keV)	Reconstruction algorithm	Uniform region			Recovery coefficients					Spillover ratios*	
			%STD	Ratio maximum/mean	Ratio minimum/mean	1 mm	2 mm	3 mm	4 mm	5 mm	Water	Air
nanoScan PET/CT	400-600	3D OSEM	9.5	1.72	-	-	-	-	-	-	0.07	0.06
		Tera-Tomo	2.7	1.10	0.88	0.27	0.83	0.94	1.01	1.04	0.06	0.05
NanoPET/CT	250-750	SSRB, MLEM	8	-	-	0.19	0.58	0.81	0.89	0.99	0.08	0.20
nanoScan PET/MRI	not given	Tera-Tomo	3.52	1.01	0.86	0.26	0.84	0.9	0.98	1.03	0.06	0.06
microPET P4	350–650	FORE + 2D FBP	5.2	1.2	0.81	0.11	0.37	0.6	0.77	0.86	4.9%	4.0%
microPET Focus 220	250–700	FORE + 2D FBP	6.8	1.27	0.71	0.15	0.41	0.63	0.74	0.86	1.2%	4.1%
microPET R4	350–650	FORE + 2D FBP	4.5	1.14	0.8	0.14	0.35	0.6	0.79	0.87	6.2%	4.6%
microPET Focus 120	350–650	FORE + 2D FBP	6	1.25	0.74	0.15	0.48	0.75	0.86	0.93	1.8%	−0.3%
Inveon	350–625	FORE + 2D FBP	5.3	1.18	0.8	0.17	0.48	0.72	0.84	0.93	1.7%	−0.6%
ClearPET	250–650	3D OSEM	10.9	1.43	0.58	0.11	0.21	0.42	0.73	0.9	36.9%	26.7%
Mosaic HP	385–665	3D RAMLA	5.1	1.19	0.8	0.16	0.36	0.56	0.7	0.84	6.3%	2.7%
Argus	250–700	3D OSEM	6	1.23	0.81	0.27	0.65	0.93	0.95	0.97	15.0%	13.0%
VrPET	100–700	3D OSEM	15.4	1.75	0.47	0.22	0.62	0.72	0.75	0.75	9.3%	8.5%
LabPET 8	250–650	2D MLEM	6	1.24	0.76	0.19	0.78	0.97	1	1.02	24.4%	13.7%
LabPET 12	250–650	2D MLEM	7.9	1.29	0.73	0.24	0.77	0.92	0.93	0.97	25.6%	16.0%

Table A.5: Summary of results from image quality phantom test [33–35]. (%STD = percentage standard deviation; FORE = Fourier rebinning; 2D = 2-dimensional; OSEM = ordered subsets expectation maximization; RAMLA = row-action maximum-likelihood algorithm; MLEM = maximum-likelihood expectation maximization). (*Values from Goertzen et al. (2012) are not provided as ratios, but as percent).

Appendix B

Python Scripts

Included in this appendix are abbreviated versions of the Python scripts developed as a part of this thesis. The Python scripts are as follows:

- **Convert DICOM file into Python array**
  This script converts DICOM files into a 3D-array, where the length of z-direction corresponds to number of slices, and the x- and y-directions corresponds to the width and the height of the slice.
- **Convert Sinogram file into Python array**
  This script converts a sinogram file into a 3D-array, where the z-direction corresponds to number of sinograms. The xy-plane is the sinogram, and as earlier mentioned the x-axis of a sinogram corresponds to displacement and the y-axis to the angle.
- **Spatial Resolution**
  Insert DICOM file as a pixel array (by using "Convert DICOM file into Python array") into this script, and FWHM and FWTM in all three orthogonal directions are generated. The location of the point source in the scanner corresponding to that DICOM file must be known. A for loop can be used to go through all the DICOM files, and plot all the FWHM- and FWTM-values as a function of radial distance from center.
- **Scatter Fraction, Count Losses, and Random Coincidence Measurements**
  Insert sinogram files as a pixel array (by using "Convert Sinogram file into Python array"), and following parameters will be generated:
  - Scatter fraction, SF
  - Total Event Rat, Rtot_j
  - True Event Rate, Rtrue_j
  - Random Event Rate, Random_j

  - Scattered Event Rate, Rscattered_j
  - Noise Equivalent Count Rate, Rnec_j

  A for loop can be used to go through all the acquisitions, and plot Rtot, Rtrue, Rrandom, Rscattered and Rnec as a function of average activity.
- **Sensitivity**
  Insert sinogram files as pixel array (by using "Convert Sinogram file into Python array"), and the the sensitivity, absolute sensitivity and position of point source in scanner relative to center of FOV is generated. A for loop can be used to go through all the acquisitions, and plot absolute sensitivity as a function of axial position of point source.
- **NEMA Image Quality Phantom Study**
  Insert DICOM file as a pixel array (by using "Convert DICOM file into Python array"), and the following values are generated:
  - Mean, minimum and maximum activity concentration and percentage standard deviation (%STD) for uniformity region,
  - Recovery coefficients and %STD for 5-rod region, and
  - Spill-over ratio and %STD for 2-chamber region.

```
##############################################
#  Convert DICOM file into Python array
##############################################
from matplotlib.pyplot import *
from numpy import *
import dicom
import os
import re

def TryInt(s):
    if s.isdigit():
        return int(s)
    return s

def dcm_zpos(dcm):
    return dcm.ImagePositionPatient[2]

def numkey(s):
    return map(TryInt, re.findall('\d+|\D+',s))

#Find and return dicom files under path
def GetFiles(path,ext):
    files = []
    for item in os.listdir(path):
        if os.path.isfile(os.path.join(path,item)) \
        and os.path.splitext(item)[1] == ext:
            files.append(item)
    return sorted(files, key=numkey)

#DICOM path
path = 'path'              #Insert DICOM path here
filelist = GetFiles(path,'')

imglist = []               #Create list for dicom images
for filename in filelist: #Loop through images in filelist
    #Open dicom image:
    imageDCM = dicom.read_file(os.path.join(path,filename))
    imglist.append(imageDCM)

#Sorts list after slice number
imglist = sorted(imglist, key=dcm_zpos)

#Find size
width,height = imglist[0].pixel_array.shape
depth = len(imglist)

#voxeldata = pixel array of DICOM files
voxeldata = empty((depth,width,height),dtype='int')
for i in range(depth):
    voxeldata[i] = imglist[i].pixel_array
```

```
##############################################
#  Convert Sinogram file into Python array
##############################################

import scipy.io as sio
import numpy as np
import re

def TryInt(s):
    if s.isdigit():
        return int(s)
    return s

def numkey(s):
    return map(TryInt, re.findall('\d+|\D+',s))

def makesinogramarray(filename):
    file = sio.netcdf_file(path+'/'+filename,mode='r')
    data = file.variables['image'].data.astype(np.double)
    image_min = file.variables['image-min'].data
    image_max = file.variables['image-max'].data
    rescale_slope = (image_max-image_min)/65535.
    rescale_intercept = image_min
    sino = (data+32768)*rescale_slope+rescale_intercept
    return sino

#Sinogram path
filename = 'filename'   #Insert Sinogram filename here

#sino = pixel array of sinogram file
sino = makesinogramarray(filname)
```

```
##############################################
#  Spatial Resolution
##############################################
from matplotlib.pyplot import *
import matplotlib.pyplot as plt
from numpy import *
import numpy as np
import dicom
import os
import re

def lin(x1,x2,y1,y2,t):
    a = (float(y2)-float(y1)) / (float(x2)-float(x1))
    b = float(y1)
    x = (t-b)/a
    return x1+x

def fw_calc(intensity, max_index, max_value, fraction):
    t = max_value*fraction
    X_l = argmax(intensity[:max_index+1]>t)
    X_r = max_index+argmax(intensity[max_index:]<t)
    X_l = lin(X_l-1,X_l, intensity[X_l-1], intensity[X_l],t)
    X_r = lin(X_r-1,X_r, intensity[X_r-1], intensity[X_r],t)
    return X_r - X_l
####################
# Insert "Convert DICOM file to python pixel array" here,
# output: voxeldata
####################

#Find slice with maximum pixel values when summed
index_z = argmax(sum(sum(voxeldata,axis=1),axis=1))
index_x = argmax(sum(sum(voxeldata,axis=0),axis=1))
index_y = argmax(sum(sum(voxeldata,axis=0),axis=0))

ImageZ = voxeldata[index_z,:,:]
ImageX = voxeldata[:,index_x,:]
ImageY = voxeldata[:,:,index_y]

#px, py, pz is middle point in intensity plot
#Change x and y so that x corresponds to radial
#direction and y to tangential direction
px=int(index_y+.5)
py=int(index_x+.5)
pz=int(index_z)

#Box size, length of sides, l
l=50;

#Values inside box in maximum xy-plane and zy-plane
intensityValue = ImageZ[py-l/2:py+l/2,px-l/2:px+l/2];
intensityValueZ = ImageY[:,py-l/2:py+l/2];
```

```
##############################################
#  Spatial Resolution, continuation
##############################################
#Get intensity profile in x-, y- and z-direction
intensityX = sum(intensityValue,axis=0)
intensityY = sum(intensityValue,axis=1)
intensityZ = sum(intensityValueZ,axis=1)

#Parabolic fit using the peak point and its two nearest
#neighboring points, to find the maximum value.
Xtopp = argmax(intensityX)
Ytopp = argmax(intensityY)
Ztopp = argmax(intensityZ)
Xrange = arange(Xtopp-1,Xtopp+2)
Yrange = arange(Ytopp-1,Ytopp+2)
Zrange = arange(Ztopp-1,Ztopp+2)
Xpeak = intensityX[Xrange]
Ypeak = intensityY[Yrange]
Zpeak = intensityZ[Zrange]
Xp = polyfit(Xrange,Xpeak,2)
Yp = polyfit(Yrange,Ypeak,2)
Zp = polyfit(Zrange,Zpeak,2)

#Take derivative of parabolic fit to find peak
X_der = polyder(Xp);
X_root_idx = roots(X_der);
X_max =  polyval(Xp,X_root_idx);
Y_der = polyder(Yp);
Y_root_idx = roots(Y_der);
Y_max =  polyval(Yp,Y_root_idx);
Z_der = polyder(Zp);
Z_root_idx = roots(Z_der);
Z_max =  polyval(Zp,Z_root_idx);

#Scales convert from pixels to mm
scale_x = float(imglist[0].PixelSpacing[0])
scale_y = float(imglist[0].PixelSpacing[1])
scale_z = float(imglist[0].SliceThickness)

#FWHM and FWTM (in mm) in the three directions are
#then found:
fwhm_x = fw_calc(intensityX,Xtopp,X_max,0.5)*scale_x
fwhm_y = fw_calc(intensityY,Ytopp,Y_max,0.5)*scale_y
fwhm_z = fw_calc(intensityZ,Ztopp,Z_max,0.5)*scale_z
fwtm_x = fw_calc(intensityX,Xtopp,X_max,0.1)*scale_x
fwtm_y = fw_calc(intensityY,Ytopp,Y_max,0.1)*scale_y
fwtm_z = fw_calc(intensityZ,Ztopp,Z_max,0.1)*scale_z
```

```
##############################################
# Scatter Fraction, Count Losses,
# and Random Coincidence Measurements
##############################################
import numpy as np
def lin(x1,x):
    x2 = x1 + 1
    y1 = sum_projection[x1]
    y2 = sum_projection[x2]
    a = (float(y2)-float(y1)) / (float(x2)-float(x1))
    b = float(y1)-a*float(x1)
    y = a*x+b
    return y
def average_activity(activity,t_acq):
    t_half = 109.771*60    #half time F-18 in seconds
    mu = np.log(2)/t_half
    A_ave = ((activity)/(mu*t_acq))*(1-np.exp(-mu*t_acq))
    return A_ave
#########################
# Insert "Convert Sinogram file to python pixel array" here,
# output: sino and sino_background
#########################
#b = no. of sinograms, n = height, m = width
b,m,n = sino.shape
a = 1    # no. of scans

#Intrinsic True Count Rate (R_int)
tot_counts = np.sum(np.sum(sino_background,axis=1),axis=1)
T_acq_bac = 20 * 60 #in seconds
Rint_i = []
for i in range(161):
    Rint_i.append(tot_counts[i]/T_acq_bac)

#Make mask, set pixels farther than 8 mm from phantom to zero
new_sinogram = np.zeros((b,n,m))
for i in range(b):          #Goes through each sinogram
    sinogram = sino[i,:,:].transpose()
    for row in range(n):     #Goes through each row
        center_index = m/2
        for col in range(m): #Goes through each pixel in row
            if col < center_index - 69 :
                new_sinogram[i,row,col] = 0
            elif col > center_index + 69:
                new_sinogram[i,row,col] = 0
            else:
                new_sinogram[i,row,col] = sinogram[row,col]
```

```
##########################################
# Scatter Fraction, Count Losses, and
# Random Coincidence Measurements, continuation
##########################################
#The max pixel in each row shall be aligned with center of sinogram
shiftet_sinogram = np.zeros((b,n,m))
for i in range(b):          #Goes through each sinogram
    sinogram = new_sinogram[i,:,:]
    for row in range(n):     #Goes through each row
        center_index = m/2
        max_index = np.argmax(sinogram[row,:])
        #Shift so that max pixel is centered
        shift = center_index-max_index
        shiftet_sinogram[i,row,:] = np.roll(sinogram[row,:],shift)
#sum_projection: pixels in shifted_sinogram with same radial
#offset summed
sum_projection_i = np.sum(shiftet_sinogram,axis = 1)

Counts_rs = np.zeros((a,b))
Counts_tot = np.zeros((a,b))
for slice in range(b):  #Goes through each sinogram
    sum_projection = sum_projection_i[slice,:]

    #The counts CL and CR shall be obtained from the sum projection.
    #Linear interpolation sall be employed to find the pixel
    #intensities at +/- 7 mm from the central pixel of the projection.
    max_index = np.argmax(sum_projection)
    CL_index = max_index-7/0.3
    CR_index = max_index+7/0.3
    CL = lin(int(CL_index),CL_index)
    CR = lin(int(CR_index),CR_index)

    #Counts_rs are found by taking average of CL and CR, which are
    #then multiplied by pixels between CR and CL, and then summed
    #with counts outside 14 mm wide strip
    CLR_average = (CL + CR)*0.5
    CLR = CLR_average*(CR_index-CL_index)
    C_outside = np.sum(sum_projection[:CL_index]) + \
np.sum(sum_projection[CR_index:])
    Crs = C_outside + CLR
#random + scattered event's counts
    Ctot = np.sum(sum_projection)
#Total event count
    scan_nr = 0         #0 as long as scan_nr = 1
    Counts_rs[scan_nr,slice] = Crs
    Counts_tot[scan_nr,slice] = Ctot

#a = no. of scans, b = no. of sinograms
#Tacq = acquisition time, A_ave = average activity
Tacq = 120 #Acquisition time
A0 = 64.95 #MBq
A_ave = average_activity(A0,Tacq)
```

```
##############################################
# Scatter Fraction, Count Losses, and
# Random Coincidence Measurements, continuation
##############################################

#Scatter fraction, SF, calculated at activities between
#1 and 1.5 MBq only.
SFi = np.zeros((b))
for col in range(a):
    SFi[col]=(np.sum(Counts_rs[col]))/(np.sum(Counts_tot[col]))
SF = (np.sum(np.sum(Counts_rs,axis=0),axis=0))/
\
(np.sum(np.sum(Counts_tot,axis=0),axis=0))

#Total Event Rate, Rtot_j
Rtot_ji = np.zeros((a,b))
for row in range(a):
    for col in range(b):
        Rtot_ji[row,col]= (Counts_tot[row,col])/Tacq
Rtot_j = np.sum(Rtot_ji,axis = 1)

#True Event Rate, Rtrue_j
Rtrue_ji = np.zeros((a,b))
for row in range(a):
    for col in range(b):
        Rtrue_ji[row,col]= (Counts_tot[row,col]-Counts_rs[row,col])/Tacq
Rtrue_j = np.sum(Rtrue_ji,axis = 1)

#Random Event Rate, Rrandom_j
Rrandom_ji = np.zeros((a,b))
for row in range(a):
    for col in range(b):
        Rrandom_ji[row,col]= Rtot_ji[row,col]- \
        (Rtrue_ji[row,col]/(1-SFi[col]))
Rrandom_j = np.sum(Rrandom_ji,axis = 1)

#Scattered Event Rate, Rscattered_j
Rscattered_ji = np.zeros((a,b))
for row in range(a):
    for col in range(b):
        Rscattered_ji[row,col]= Rtot_ji[row,col]-Rtrue_ji[row,col]- \
        Rrandom_ji[row,col]-Rint_i[col]
Rscattered_j = np.sum(Rscattered_ji,axis = 1)

#Noise Equivalent Count Rate, Rnec_j
Rnec_ji = np.zeros((a,b))
for row in range(a):
    for col in range(b):
        Rnec_ji[row,col]= (Rtrue_ji[row,col]*Rtrue_ji[row,col])/ \
        Rtot_ji[row,col]
Rnec_j = np.sum(Rnec_ji,axis = 1)

##Plot: A_ave on x-axis and Rtot_j, Rtrue_j, Rrandom_j,
##Rscattered_j and Rnec_j on y-axis
```

```
##########################################
# Sensitivity
##########################################
import scipy.io as sio
import numpy as np
import matplotlib.pyplot as plt
import matplotlib.cm as cm
########################
# Insert "Convert Sinogram file to python pixel array" here,
# output: sino and sino_background
########################
#o = no. of sinograms, a = no. of rows, b = no. of columns (of
#transpose sinogram), CFOV = center of FOV
o, b, a = sino.shape
CFOV =  o/2.*0.585

#Sinogram with maximum pixels intensities, sino_maks
index_z = np.argmax(np.sum(np.sum(sino,axis=1),axis=1))
sino_maks = sino[index_z,:,:].transpose()
sino_background_maks = sino_background[index_z,:,:].transpose()

#Each row in sino, all pixels 1 cm from max pixel is set to zero
#to make new_sinogram. Same mask is applied to sino_background
new_sinogram = np.zeros((o,a,b))
new_background_sinogram = np.zeros((o,a,b))
for i in range(o):      #Goes through each sinogram
    sinogram = sino[i,:,:].transpose()
    sinogram_background = sino_background[i,:,:].transpose()
    for row in range(a): #Goes through each row
        maks_index = np.argmax(sino_maks[row,:])
        for col in range(b): #Goes through each pixel in row
            if col < maks_index - 34 :
                new_sinogram[i,row,col] = 0
                new_background_sinogram[i,row,col]=0
            elif col > maks_index + 34:
                new_sinogram[i,row,col] = 0
                new_background_sinogram[i,row,col]=0
            else:
                new_sinogram[i,row,col] = sinogram[row,col]
                new_background_sinogram[i,row,col]= \
                sinogram_background[row,col]

T_acq = 1.*60. #Acquisition time in seconds
T_acq_background = 20.*60 #Background acquisition time in seconds
A_cal = 278.25   #Activity in kBq

#Counting rates R_i and R_Bi
R_i = np.sum(new_sinogram)/T_acq
R_Bi = np.sum(new_background_sinogram)/T_acq_background

#Sensitivity S_i and absolute sensitivity S_ai
S_i = (R_i - R_Bi)/A_cal
S_ai = (S_i/1000.) / 0.9060 *100.

#Position of point source in scanner relative to CFOV
Position = index_z*0.585 - CFOV
```

```
##############################################
# NEMA Image Quality Phantom Study
##############################################

from matplotlib.pyplot import *
import numpy as np
import dicom
import os
import re
from scipy.stats import linregress

def MakeImage(clicks, length):
    #Click on top and bottom of region
    clicks = ginput(clicks)
    #Use clicks to find central point in region,
    #and get image, which is the slices within
    #+/- length/2 mm from this point.
    len = length * 0.5
    uni_za,uni_zb = clicks
    uni_z = (uni_za[1]+uni_zb[1])/2
    uni_za = int(uni_z-len/scale_z)
    uni_zb = int(uni_z+len/scale_z)
    image = voxeldata[uni_za:uni_zb]
    return clicks, image

def MakeMask(clicks,image,diameter):
    #Show average of image, and click in center roi
    image_mean = np.mean(image,axis=0)
    imshow(image_mean)
    radius = diameter * 0.5
    clicks = ginput(1)
    x = clicks[0][0]
    y = clicks[0][1]
    mask = (xx-x)**2+(yy-y)**2 <= (radius/scale_z)**2
    return clicks, mask, image_mean

########
# Insert "Convert DICOM file to python pixel array" here,
# output: voxeldata
#######
#Scales convert from pixels to mm
scale_x = float(imglist[0].PixelSpacing[0])
scale_y = float(imglist[0].PixelSpacing[1])
scale_z = float(imglist[0].SliceThickness)
# generate coordinates
x = np.arange(0,height)
y = np.arange(0,width)
xx,yy = np.meshgrid(x,y)
```

```
##############################################
# NEMA Image Quality Phantom Study, continuation
##############################################

###UNIFORMITY###
#Plot average dicom image
top_image=np.mean(voxeldata, axis=2)
subplot(321)
imshow(top_image)
clicks, uni_image = MakeImage(2,10)
subplot(322)
clicks2,uni_mask, uni_image_mean = MakeMask(1,uni_image,22.5)

#mean, min, max activity concentration and %std is output
uni_voi = uni_image[:,uni_mask]
uni_mean = np.mean(uni_voi)
uni_std = np.std(uni_voi)
uni_std_percent = uni_std/uni_mean*100.
uni_max = np.max(uni_voi)
uni_min = np.min(uni_voi)

###5-ROD REGION (recovery coefficients)###
#Plot average dicom image
side_image=np.mean(voxeldata, axis=1)
subplot(323)
imshow(side_image)
clicks3, cyl_image = MakeImage(2, 10)

#Cyl_diam is diameter of 5-rods in mm,
cyl_diam = np.array([1.,2.,3.,4.,5.])
```

```
##############################################
# NEMA Image Quality Phantom Study, continuation
##############################################

#Analyse each rod seperately
for i in range(len(cyl_diam)):
    subplot(324)
    clicks4, cyl_mask, cyl_image_mean = \
    MakeMask(1,cyl_image,2*cyl_diam[i])
    cyl_max = cyl_image_mean == np.max(cyl_image_mean[cyl_mask])
    cyl_pos = np.logical_and(cyl_max,cyl_mask)
    cyl_xy = np.unravel_index(np.argmax(cyl_pos),cyl_pos.shape)

    #The transverse image pixel coordinates of the locations of the
    #maximum ROI values are used to create line profile, cyl_voi
    trans_x = 0.05
    trans_y = 0.01
    length = 10 / scale_z
    cyl_zz = np.arange(-length/2,length/2)
    cyl_x = (cyl_xy[0]-trans_y*(cyl_zz)+.5).astype('int')
    cyl_y = (cyl_xy[1]-trans_x*(cyl_zz)+.5).astype('int')
    cyl_voi = (cyl_image[:,cyl_xy[0],cyl_xy[1]]).astype('float')

    #The mean, cyl_mean, and %std, RC_STD,
    #of the RC of the rod are found
    cyl_voi /= uni_mean
    cyl_mean = np.mean(cyl_voi)
    cyl_std = np.std(cyl_voi)
    RC_STD=100.*np.sqrt((cyl_std/cyl_mean)**2+(uni_std/uni_mean)**2)

###WATER- AND AIR-FILLED CHAMBERS###
#Plot average dicom image
side_image_2=np.mean(voxeldata, axis=1)
subplot(325)
imshow(side_image_2)
clicks5, w_a_image = MakeImage(2, 7.5)

#Analyse one chamber at the time
for i in range(2):
    subplot(326)
    clicks6,w_a_mask,w_a_image_mean= MakeMask(1,w_a_image,4)

    #The spill-over ratio and %std are now found
    w_a_voi = w_a_image[:,w_a_mask]
    w_a_mean = np.mean(w_a_voi)
    w_a_std = np.std(w_a_voi)
    w_a_STD=100.*np.sqrt((w_a_std/w_a_mean)**2+(uni_std/uni_mean)**2)
    SOR = w_a_mean/uni_mean
```

Appendix C

Data Sheets of Radioactive Sources

Included below are data sheets of the radioactive sources used during this work.

RADIONUCLIDE SAFETY DATA SHEET

NUCLIDE: F-18 **FORMS: ALL SOLUBLE**

PHYSICAL CHARACTERISTICS:

HALF-LIFE: 109.74 min. TYPE DECAY: EC e^+
gamma: 0.511 MeV (193 %)
beta: 0.633 MeV maximum

Hazard category: C- level (low hazard) : 1 mCi to 100 mCi
B - level (Moderate hazard) : > 100 mCi to 10 Ci
A - level (High hazard) : > 10 Ci

EXTERNAL RADIATION HAZARDS AND SHIELDING:

The gamma exposure rate at 1 cm from 5 mCi is 28.2 R/hr. The exposure rate varies directly with activity and inversely as the square of the distance. The 1/10 value layer in lead is 1.6 cm. The beta absorbed dose rate at 1 cm from 5 mCi is 1500 R/hr. The range of the 0.633 MeV beta is 0.1921 cm in lucite and 0.0907 cm in glass.

HAZARDS IF INTERNALLY DEPOSITED:

The annual limit on oral intake (ALI) of F-18 corresponding to a whole-body guideline gamma exposure rate of 500 mrem/year is 5.4 mCi.

DOSIMETRY AND BIOASSAY REQUIREMENTS:

Film badges and dosimeter rings are required for all usage of F-18.

SPECIAL PROBLEMS AND PRECAUTIONS:

1. Because the specific gamma-ray constant for F-18 is high (5.65 R-cm/mCi-hr), syringe shields will be relatively ineffective at attenuating the 0.511 MeV annihilation quanta, so exposure reduction can best be achieved through avoiding unnecessary holding of the filled syringe prior to injection. Store stock material and filled syringes in lead pigs. Unnecessary exposure to personnel and other patients should be minimized by increasing distance from the patient while he is waiting to be scanned. The gamma exposure rate at 1 meter from a patient containing 5 mCi of F-18 will be approximately 2.5 mR/hr.

2. Segregate wastes with those with half-lives less than 4 days (e.g. Tc-99m).

3. Dilute aqueous wastes may be disposed to the sewer system in amounts of up to 1000 uCi daily per lab.

RADIONUCLIDE SAFETY DATA SHEET

NUCLIDE: Na-22 **FORMS: ALL SOLUBLE**

PHYSICAL CHARACTERISTICS:

HALF-LIFE: 2.6 years
TYPE DECAY: positron emission --- maximum energy 0.545 MeV
gamma ray associated with annihilation 0.511 MeV
accompanying gamma photons 1.275 MeV

Hazard category: C- level (low hazard) : 0.001 to 0.1 mCi
B - level (Moderate hazard) : > 0.1 mCi to 10 mCi
A - level (High hazard) : greater than 10 mCi

EXTERNAL RADIATION HAZARDS AND SHIELDING:

The gamma exposure rate at 1 cm from 1 mCi of Na22 shielded for positrons is 12000 mR/hr. The half and tenth values of lead for this gamma are 0.9 and 3.6 cm respectively. The maximum exposure rate at 1 foot from such storage areas must be shielded to less than 2 mR/hr.

The dose rate from the positrons is 310,000 mrads/hr at 1 cm per mCi. The maximum range of the positrons is about 44 inches in air, and about 0.06 inches in lucite. The use of the lead shield for storage will provide and adequate shield for the positron particles.

HAZARDS IF INTERNALLY DEPOSITED:

It is important to avoid ingestion and /or skin contamination.

The Annual Limit of Intake based on a whole body dose of 500 mrem per year is 54 microcuries. The maximum permissible body burden is 10 microcuries; the critical organ being the body fluids.

DOSIMETRY AND BIOASSAY REQUIREMENTS:

Film badges and dosimeter rings are required if 0.5 millicuries or more are being handled at any one time or 0.1 millicurie levels are handled on a frequent (daily) basis.

SPECIAL PROBLEMS AND PRECAUTIONS:

1. Work behind shielding, preferably transparent materials. Use remote handling whenever possible.

2. Survey frequently. Change gloves often.

3. Segregate wastes to those with half-lives greater than 90 days (but not with H3 and/or C14).

4. Limit of soluble waste to sewer: 1 microcurie per day per lab.